Astronomy Letters, Vol. 27, No. 10, 2001, pp. 615–624. Translated from Pis'ma v Astronomicheskiĭ Zhurnal, Vol. 27, No. 10, 2001, pp. 723–734.

Effects of Possible Deviations of Fundamental Physical Constants on Primordial Nucleosynthesis

A. V. Ivanchik, A. V. Orlov, and D. A. Varshalovich*

Ioffe Physicotechnical Institute, ul. Politekhnicheskaya 26, St. Petersburg, 194021 Russia

Received July 11, 2000; in final form, May 10, 2001

Abstract—We study the effects of possible deviations of fundamental physical constants on the yields of light nuclides, ^{2}D, ^{3}He, ^{4}He, ^{7}Li, and others during primordial nucleosynthesis. The deviations of fundamental constants from their current values are considered in the low-energy approximation of string theories; the latter predict the existence of a scalar field, which, apart from the tensor gravitational field, determines the space geometry. A two-parameter (η, δ) model is constructed for primordial nucleosynthesis: $\eta = n_B/n_\gamma$ is the baryon-to-photon density ratio, and δ is the relative deviation of fundamental physical constants at the epoch of primordial nucleosynthesis from their current values. A dependence of η on the deviation of coupling constants δ has been derived on condition that the primordial helium abundance is $Y_p = f(\eta, \delta) = \text{const}$, where const corresponds to experimental values. We thus showed that the relative baryonic density (and hence Ω_B) could vary over a much wider range than allowed by the standard nucleosynthesis model. Considering this result, we discuss the recently found mismatch between Ω_B obtained from an analysis of CMBR anisotropy and from the standard primordial nucleosynthesis model. *© 2001 MAIK "Nauka/Interperiodica".*

Key words: *theoretical and observational cosmology*

INTRODUCTION

The recent announcement about the possible detection of a cosmological change in the fine-structure constant $\alpha = e^2/\hbar c$ made after the spectra of distant quasars had been analyzed (Webb *et al.* 1999; Murphy *et al.* 2000) has rekindled interest in theories with changing constants. If the fundamental constants actually differed at the formation epoch of quasar spectra, then we have good reason to expect their difference at earlier epochs of the evolution of the Universe, in particular, at the stage of primordial nucleosynthesis. The latter can serve as a sensitive indicator of the conditions that existed in the first minutes of the life of our Universe. Here, our goal is to study the effects of changes in fundamental physical constants on the yields of light nuclides during primordial nucleosynthesis.

The recently found mismatch between the baryonic density inferred from CMBR anisotropy observations (Jaffe *et al.* 2000) and its value obtained from the standard primordial nucleosynthesis theory can serve as an additional argument for modifying the primordial nucleosynthesis theory.

THE ROLE OF SCALAR FIELDS IN COSMOLOGY

Currently, the relationship between cosmology and particle physics has been found to be increasingly intimate. The scalar fields that correspond to zero-spin particles such as Higgs particles, dilatons, axions, and others necessarily arise in current unification theories of fundamental interactions (SUSY GUT, Superstrings/M-theory, and others). They can significantly affect the expansion dynamics of the Universe during certain periods of its evolution. This can occur at the dilaton-dominated epoch ($\lesssim 10^{-43}$ s), at the inflationary epoch (~10^{-38} s), and at the current evolutionary stage of the Universe, which may correspond to the quasi-de-Sitter expansion with acceleration. The physical manifestations of scalar fields apart from those mentioned above can take various forms. For example, they can manifest themselves in space–time variations of the fundamental physical constants that characterize the strengths of various interactions.

Temporal variations of the coupling constants can be revealed by analyzing the dependence of the primordial ^{4}He mass fraction on gravitational constant G, on fine-structure constant α, and on other constants (Kolb *et al.* 1986; Barrow 1987). Based on astronomical observational data for the primordial helium abundance Y_p, Kolb *et al.* (1986) imposed constraints (~2–3%) on the possible deviations of fundamental physical constants at the epoch of primordial nucleosynthesis from their current values. However, they varied different constants separately (with the remaining constants being fixed) and assumed the parameter $\eta = n_B/n_\gamma$, the baryon-to-photon density ratio, to also be fixed.

* E-mail address for contacts: varsh@astro.ioffe.rssi.ru

Subsequently, modifying the standard nucleosynthesis theory, several authors imposed constraints on the relative change in fundamental physical constants by taking into account the possible simultaneous change in various constants (see, e.g., Campbell and Olive 1995; Santiago *et al.* 1997; Bergström *et al.* 1999). However, the calculations were performed for a specific fixed η [as in the pioneering study by Kolb *et al.* (1986)].

In this paper, we consider a two-parameter (η, δ) model for primordial nucleosynthesis, in which η is a free parameter and can depend (for a constant yield of light elements) on the deviation of constant δ. The parameter δ characterizes the relative deviation of fundamental physical constants at the epoch of primordial nucleosynthesis from their current values. We propose specific dependencies of the coupling constants on scalar-field parameters.

The most comprehensive similar study has recently been carried out by Damour and Pichon (1999). However, they represent the change in fundamental constants by the change in the gravitational constant G alone, which is not enough from the viewpoint of more general current theories. Their justification of the change in constant G is ambiguous (see, e.g., Magnano and Sokolowski 1994; Damour and Polyakov 1994; see below for more details).

Here, we consider a wider class of models and estimate the effects of changes in various constants on the nuclide yield during primordial nucleosynthesis.

BASIC POINTS OF THE STANDARD PRIMORDIAL NUCLEOSYNTHESIS THEORY

The classic studies of primordial nucleosynthesis (Wagoner 1969, 1970) were carried out in terms of two standard models: the standard cosmological model and the standard model of particle physics.

The standard cosmological model (Big Bang) was universally accepted after the discovery of cosmic microwave background radiation (CMBR). The following facts form its observational basis:

(i) Expansion of the Universe [with the current Hubble constant $H_0 = 100h$ km s^{-1} Mpc^{-1} ($h \approx 0.7$)];

(ii) CMBR (T = 2.73 K is the current blackbody temperature of the photon spectrum);

(iii) The relative abundances of light nuclides (^{2}D, ^{3}He, ^{4}He, ^{7}Li, and others).

Being in good agreement with observational data, the standard cosmological model, nevertheless, has a number of conceptual difficulties (unnatural initial conditions, the horizon and flatness problem, baryonic asymmetry, the problem of the cosmological constant, and others). In any case, a modification of the standard model that eliminates the above difficulties and that is consistent with particle physics must contain as a zero approximation the standard cosmological model, which has stood the test of time, just as the Newtonian gravitational theory is contained in the general theory of relativity.

Modern particle physics is based on the Standard Model of fundamental interactions. The local gauge symmetry described by the group $SU_c(3) \otimes SU_L(2) \otimes U(1)$, where $SU_c(3)$ is the symmetry of the strong color interaction between quarks and gluons and $SU_L(2) \otimes U(1)$ describes the electroweak interaction, underlies this model (Okun' 1984). In the Standard Model, three of the four fundamental interactions (strong, electromagnetic, and weak) are described in a unified way. Presently, there are no experimental data that would be in clear conflict with this model in the energy range accessible for current experiments. However, all three interactions are not actually unified in the Standard Model, and there are still three different coupling constants (g_1, g_2, g_3), which are free model parameters. The true unification could be achieved based on a simple (nonreducible) group (with a single coupling constant $g_{\rm GUT}$) that would include a direct product of the gauge groups of the three interactions:

$$\mathcal{G} \supset SU_c(3) \otimes SU_L(2) \otimes U(1). \qquad (1)$$

At the same time, the gravitational interaction remains outside this unification as before and is described by its own coupling constant $G \sim M_{\rm Pl}^{-2}$, where $M_{\rm Pl} \equiv \sqrt{\hbar c/G} \equiv 2.2 \times 10^{-5}$ g is the Planck mass.

EXTENSION OF THE STANDARD MODEL

The supersymmetry methods that unify bosons and fermions, allow gravitation to be unified with other gauge theories (quantum chromodynamics, Weinberg–Salam–Glashow electroweak theory), and are outside the scope of the local quantum field theory have been developed with a generalization of the concept of geometry and the dimensionality of an elementary object. These methods have led to the development of the superstring theory. The superstring theory and its various generalizations and modifications (M-theory and others) are presently the true claimants to the role of a Grand Unification Theory for all interactions (see Green *et al.* 1987; Polyakov 1987; Ketov 1990; Morozov 1992; and references therein). However, the current superstring theory is still a subject of pure mathematics rather than of experimental physics, because most of its predictions lie in the energy range inaccessible in current experiments ($E \lesssim E_{\rm Pl} = M_{\rm Pl}c^2 \simeq 1.2 \times 10^{19}$ GeV). Nevertheless, there are elements in the low-energy behavior of the theory whose presence or absence in an experiment allows its various versions to be discussed. Thus, for example, small but nonzero changes in the coupling constants during cosmological evolution are an important observational effect predicted by current theories. In this paper, we discuss variations in the low-energy limits of fundamental constants rather than their

changes with interaction energy (running coupling constants; see, e.g., Okun' 1998).

A SCALAR-TENSOR MANIFESTATION OF GRAVITATION

In addition to the tensor field in general relativity whose quanta are gravitons, all versions of the superstring theory predict the existence of a fundamental scalar field whose quanta are dilatons (Green *et al.* 1987). In these theories, gravitation is equally described by the Riemann tensor $R^{\lambda}_{\mu\tau\nu}$ (convolution of the Riemann tensor, the Ricci tensor $R_{\mu\nu} \equiv R^{\lambda}_{\mu\lambda\nu}$, appears in Einstein's equations) and by the dilaton field Φ.

To determine the behavior of matter, let us write the action of the superstring theory. In general, this action is written for the motion of a string in D-dimensional space ($D > 4$), where $D - 1$ is the number of spacelike dimensions. Since we analyze the energies that are much lower than $E_{\rm Pl}$, the low-energy limit of the reduced four-dimensional action is of interest (Lovelace 1984; Fradkin and Tseytlin 1985; Callan *et al.* 1985, 1986)

$$S = \frac{1}{2k^2}\int d^4x\sqrt{-g}e^{-\Phi}(R + \partial_\mu\Phi\partial^\mu\Phi + 2k^2\mathcal{L}_m[\psi_m, g_{\mu\nu}]), \quad (2)$$

where $k^2 = 8\pi G$, $g_{\mu\nu}$ is the space metric with signature $(-+++)$, $g \equiv \det g_{\mu\nu}$, $R \equiv g^{\mu\nu}R_{\mu\nu}$ is the scalar curvature, and $\mathcal{L}_m$ is the Lagrangian density related to the nongravitational fields of the matter ψ_m (the fermion and gauge fields are the interaction carriers). This form of the action is called Jordan's frame (Jordan 1949).

However, the problem of the theory based on action (2) is that the gravitational part of Eq. (2) is equivalent to the theory of Brans and Dicke (1961) with the parameter $\omega = -1$, which, in turn, is inconsistent with observational constraints on ω ($|\omega| \gg 1$; Will 1993). Initially, the solution of this problem in terms of the string theory was reduced to the artificial introduction of dilaton mass m_Φ [or to the introduction of a potential $V(\Phi)$] (Taylor and Veneziano 1988), which allowed the dilaton field to be stabilized near a constant value Φ_0. The theory with action (2), in which $\Phi = \text{const} = \Phi_0$, is equivalent to the general theory of relativity. However, this solution of the problem suggests the existence of as yet unknown dynamical mechanisms for the assumption of mass by the dilaton and cause several other difficulties. In particular, it is unclear at which evolutionary stage of the Universe the dilaton is stabilized.

Damour and Polyakov (1994) proposed a different elegant method of solving this problem, which allows a theory with changing constants and particle masses consistent with currently available observational data to be constructed for a massless (!) dilaton. The string coupling parameter of gravitational fields with matter $e^{-\Phi}$ in action (2) was obtained only in the tree string interaction approximation. Including all expansion terms results in a modification of the string coupling parameter $e^{-\Phi} \longrightarrow W^2(\Phi)$. The action with this coupling parameter is equivalent to the generalized scalar-tensor theory (Wagoner 1970; Will 1993). The latter necessarily approaches the general theory of relativity as the Universe expands (the attractor mechanism; Damour and Nordtvedt 1993), which corresponds to a zero coupling constant of the dilaton field with matter.

The laws of motion for gravitational fields $\{R_{\mu\nu}, \phi\}$ have the most simple and convenient form if action (2) is written in Einstein frame, where the metric kinetic term is represented in canonical form (i.e., simply R). For this purpose, a conformal transformation of the metric is made, $g_{\mu\nu} \longrightarrow W^2(\Phi)g_{\mu\nu}$. Subsequently, the scalar field is redefined, $\Phi \longrightarrow \phi(\Phi)$, so that the kinetic term of the new field ϕ has a standard form, and action (2) can then be represented as

$$S = \frac{1}{2k^2}\int d^4x\sqrt{-g}(R - 2\partial_\mu\phi\partial^\mu\phi + 2k^2W^{-2}(\phi)\mathcal{L}_m[\psi_m, g_{\mu\nu}(\phi)]). \quad (3)$$

The action written in this way leads to usual Friedmann equations for the dynamics of the scaling factor of the Universe $a(t)$ in the gravitational sector. However, if the scalar field ϕ depends on spatial-temporal coordinates, then the coupling constants that appear in the Lagrangian of matter $\mathcal{L}_m$ and that describe the interaction between various types of fields will necessarily depend on cosmological time and, in general, on spatial-temporal coordinates.

Thus, the low-energy limit of string theories yields:

(i) GTR + scalar field in gravitation;

(ii) standard $SU_c(3) \otimes SU_L(2) \otimes U(1)$ physics with the coupling constants and particle masses dependent on the cosmological evolution of the dilaton field, $g_i = g_i[f_1(\phi)]$ and $m_j = m_j[f_2(\phi)]$, respectively, in particle physics.

It should be noted that the physical equivalency of action (2) [Jordan Frame (JF)] and action (3) [Einstein Frame (EF)] is treated differently by different authors. According to the authors of the first group, JF is physical, while EF is considered as a convenient computational procedure; the authors of the second group consider EF as physical; and the authors of the third group consider the two frames to be physically equivalent [this issue is discussed in detail in the review by Magnano and Sokolowski (1994)]. Thus, we consider two possible cases: (1) JF is physical and (2) EF is physical.

METHODS FOR STUDYING THE EARLY UNIVERSE

At present, we can observe few physical processes that allow the conditions that existed in the early Uni-

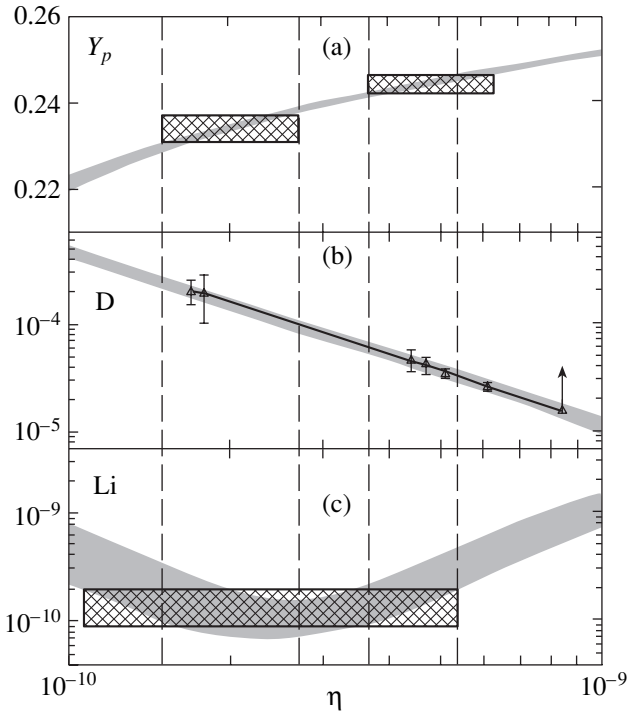

Fig. 1. Light-nuclide yields versus relative baryonic density $\eta = n_B/n_\gamma$: (a) $Y_p = m(^4\mathrm{He})/(m(\mathrm{H}) + m(^4\mathrm{He}))$, (b) D = [D]/[H], and (c) Li = [^{7}Li]/[H]. The band widths characterize the uncertainties of theoretical calculations; the triangles and hatched rectangles indicate the uncertainties of astronomical observations.

verse to be studied. Thus, for example, by analyzing quasar spectra, we can see the Universe up to $z \simeq 7$, where z is the redshift, $1 + z \equiv a(t_0)/a(t)$, $a(t)$ is the scaling factor, and t_0 is the current age of the Universe. The CMBR makes it possible to look into the past of the Universe up to $z \approx 10^3$. Much earlier evolutionary stages of the Universe ($z \approx 10^9$) can be studied by observing the relative abundances of the light elements produced during primordial nucleosynthesis.

Standard nucleosynthesis in the Big Bang model predicts the relative abundances of light nuclei that are in satisfactory agreement with helium, deuterium, and lithium observations.

Table 1. The abundances of light elements

	Range	Source
Y_p	0.244 ± 0.002	Izotov and Thuan (1998)
	0.234 ± 0.003	Olive *et al.* (1997)
D/H	$(2.0 \pm 0.5) \times 10^{-4}$	Webb *et al.* (1997)
	$(1.9 \pm 0.5) \times 10^{-4}$	Rugers and Hogan (1996)
	$(4.0 \pm 0.7) \times 10^{-5}$	Burles and Tytler (1998)
	$(3.4 \pm 0.3) \times 10^{-5}$	Kirkman *et al.* (1999)
	$(4.4 \pm 0.9) \times 10^{-5}$	Levshakov (1998)
	$\gtrsim 1.5 \times 10^{-5}$	Molaro *et al.* (1999)
	$(2.5 \pm 0.2) \times 10^{-5}$	O'Meara *et al.* (2000)
^{7}Li/H	$(1.7 \pm 0.5) \times 10^{-10}$	Bonifacio and Molaro (1997)
	$(1.4 \pm 0.5) \times 10^{-10}$	Ryan *et al.* (2000)

The yield of light elements in the standard nucleosynthesis model depends on the only parameter $\eta = n_B/n_\gamma$, which has been constant from the annihilation of electrons and positrons up until now (Fig. 1). This quantity can be expressed in terms of the contribution of baryons to the matter density in the Universe at the current epoch, $\Omega_B \equiv \rho_B/\rho_{cr}$:

$$\eta_{10} \simeq 274\Omega_B h^2, \tag{4}$$

where $\rho_{cr} = 3H_0^2/8\pi G$ is the critical density and $\eta_{10} = 10^{10}\eta$.

Currently available observational data on the light-element abundances in the standard primordial nucleosynthesis model provide the most stringent constraints on the baryonic density of the Universe Ω_B. Table 1 gives estimates for the relative abundances of primordial helium, deuterium, and lithium. Note that the accuracy of determining the primordial helium abundance is presently an order of magnitude higher than the accuracy of determining the deuterium and lithium abundances. Besides, the assertions about the primordial origin of these elements are model-dependent. Gnedin and Ostriker (1992) showed that the gamma-ray fluxes detected from several quasars could be enough to produce the observed amounts of D and ^{3}He through ^{4}He photodisintegration.

Some processes in the interstellar medium can also produce light elements, for example, spallation reactions during the interaction of cosmic rays (nonthermal particles) with interstellar matter (Bykov 1995). The latter processes are most effective during starbursts, which apparently took place at $z > 7$.

CONSTANTS IN THE FORMULAS FOR PRIMORDIAL NUCLEOSYNTHESIS

The primordial synthesis of nuclei was described in detail, for example by Wagoner (1969), Weinberg (1972), and Kolb and Turner (1990).

In the standard nucleosynthesis model at energies $E > 1$ MeV ($T > 10^{10}$ K), the particles that constituted the primordial plasma (protons, neutrons, electrons, positrons, neutrinos, and antineutrinos) at this time were in thermodynamic equilibrium. The equilibrium between protons and neutrons was maintained by the weak reactions

$$p + e^- \rightleftharpoons n + \nu_e, \quad n + e^+ \rightleftharpoons p + \bar{\nu}_e,$$
$$n \rightleftharpoons p + e^- + \bar{\nu}_e. \tag{5}$$

The ratio of neutron number n to proton number p in thermodynamic equilibrium was determined by the Boltzmann factor:

$$\frac{n}{p} \simeq \exp\left(-\frac{Q}{T}\right), \quad (6)$$

where $Q \equiv (m_n - m_p)c^2 \simeq 1.3$ MeV. The equilibrium was conserved as long as the characteristic weak reaction rates Γ_W exceeded the expansion rate of the Universe H. At temperatures $T = T_f \lesssim 1$ MeV (f stands for freeze-out), the rates of processes (5) became insufficient to maintain the equilibrium, and the n/p ratio proved to be frozen; i.e., it essentially ceased to depend on time. To be more precise, the fraction of neutrons subsequently slowly decreased, mainly through their β decay on a time scale $\tau_n = 886.7$ s (neutron lifetime) (see Fig. 2).

In the energy range 1 MeV to 0.01 MeV, the chain of nuclear reactions leads to the burning of virtually all neutrons to produce ^{4}He and a small fraction ($\sim 10^{-4}$) of ^{2}D and ^{3}He. Thus, the mass fraction of primordial ^{4}He in the total mass of the Universe is $Y_p \simeq 2(n/p)_f/(1 + (n/p)_f)$. Given the time Δt elapsed from the time when the n/p ratio was frozen until the peak of the main nuclear reactions, the above value will be slightly smaller because of the neutron free decay. The final formula for Y_p, which implicitly contains all the basic constants (α, m_e, Q, τ_n, G_F) that determine the process under consideration, is

$$Y_p \simeq \frac{2(n/p)_f}{1 + (n/p)_f} \exp(-\Delta t/\tau_n), \quad (7)$$

where $(n/p)_f = (-Q/T_f)$. Therefore, a change in α, m_e, Q, τ_n, or G_F causes a change in Y_p and, naturally, in the relative abundances of other nuclei.

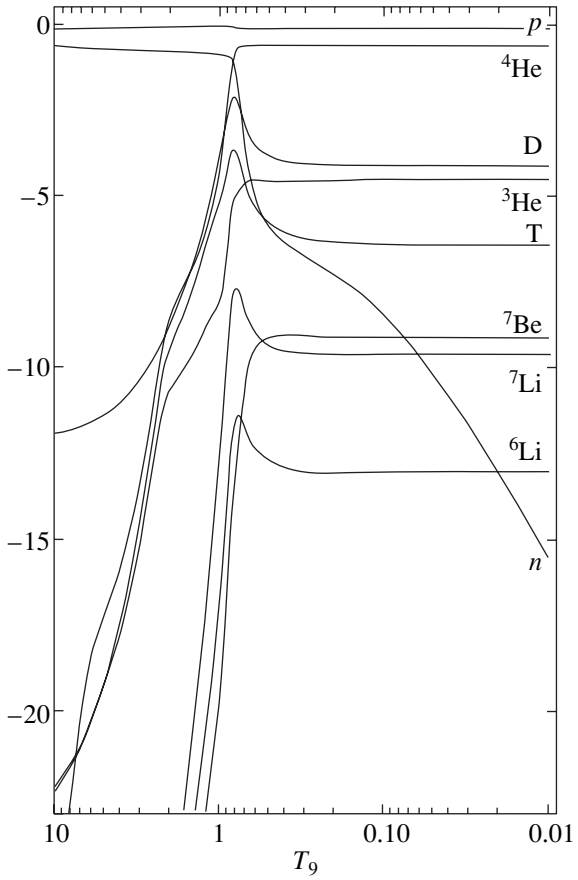

Fig. 2. Evolution of the relative light-nuclide abundances during primordial nucleosynthesis as a function of temperature ($T_9 = T \times 10^{-9}$).

THE TWO-PARAMETER (η, δ) MODEL FOR PRIMORDIAL NUCLEOSYNTHESIS

To solve the formulated problem, we developed a numerical code for computing the relative abundances of the light elements produced during primordial nucleosynthesis (see, Orlov and Varshalovich 1998). The basic elements of this code are the same as those in the classic code of Wagoner (1969) [updated by Kawano (1992) and Smith *et al.* (1993)]. However, we completely reconsidered the integration procedures, added new nuclear reactions, used currently available cross-section data, and, most importantly, updated the code in accordance with the problem under discussion by treating the fundamental constants as variable parameters of the numerical code.

The basic cosmological equations (here, we consider a flat Universe; i.e., $k = 0$) in the presence of a scalar field are derived in the standard way, i.e., by minimizing action (3). They are as follows:[1]

$$-3\frac{\ddot{a}}{a} = 4\pi G(\rho + 3p) + 2\dot{\phi}^2, \quad (8)$$

$$\left(\frac{\dot{a}}{a}\right)^2 \equiv H^2 = \frac{8\pi G}{3}\rho + \frac{1}{3}\dot{\phi}^2, \quad (9)$$

$$\ddot{\phi} + 3H\dot{\phi} = -\frac{4\pi G}{3}\rho(1/3 - \gamma)\sigma(\phi). \quad (10)$$

The latter equation describes the evolution of scalar field ϕ and, hence, the evolution of all coupling constants. Its solution depends on the form of function $\sigma(\phi)$, which characterizes the coupling of matter with the dilaton field, and on the equation of state for the matter that fills the Universe, $p_{tot} = \gamma\rho_{tot}$. The function $\sigma(\phi)$ is given by the relation $\sigma(\phi) = \partial \ln W(\phi)/\partial\phi$.

In Fig. 3, γ is plotted against ζ, which is given by the relation $d\zeta = H(t)dt$. When the initial condition $\zeta(z = 0) = 0$ is chosen, ζ will be related to the redshift by $\zeta = \ln(a/a_0) = -\ln(1 + z)$. At the radiation-dominated epoch, when $\gamma = 1/3$, the scalar field is decoupled with matter, and Eq. (10) is particularly simple: $\ddot{\phi} + 3H\dot{\phi} = 0$ or, if written in terms of ζ, $\phi'' + \phi' = 0$ (here, the prime denotes dif-

[1] Note that, for a constant scalar field, ϕ = const, the string action (2) coincides with the Einstein action. Therefore, we obtain the standard general-relativity equations as the gravitation equations, and Eqs. (8) and (9) coincide with Friedmann's equations.

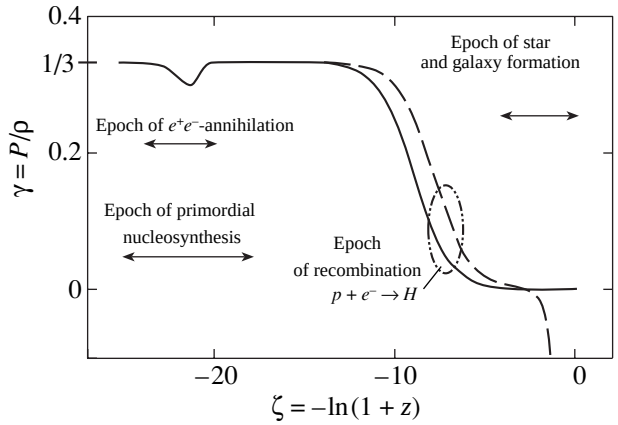

Fig. 3. Parameter $\gamma = p/\rho$ versus $\zeta = \ln(a/a_0) = -\ln(1 + z)$.

ferentiation with respect to parameter ζ). Accordingly, the solution of these equations is

$$\phi(t) = \phi_R + \frac{b_1}{\sqrt{t}}, \quad \phi(\zeta) = \phi_R + b_2 \exp(-\zeta). \qquad (11)$$

Therefore, if the derivative $\dot{\phi}$ (and ϕ') was nonzero at some initial time (long before primordial nucleosynthesis), then $\dot{\phi}$ (and ϕ') will approach zero and the field ϕ itself will tend to a constant value, which we denoted by ϕ_R. This circumstance significantly facilitates the solution of Eqs. (8)–(10) in the radiation-dominated period. It also allows the numerical simulation of primordial nucleosynthesis to be greatly simplified by assuming that ϕ changes only slightly over the entire period of the nuclear reactions.

We see from Fig. 3 that the radiation-dominated period ($\gamma = 1/3$) gives way to a phase dominated by nonrelativistic matter with $\gamma = 0$. The solid and dashed lines correspond, respectively, to the cosmological model with $\rho_M = \rho_{cr}$, $\rho_V = 0$ and to the model with a vacuum-dominated phase, $\rho_M = 0.3\rho_{cr}$, $\rho_V = 0.7\rho_{cr}$. In both cases, from the time when γ becomes much less than 1/3, the field ϕ, according to Eq. (10), must change; this change depends on the specific model for the coupling of the scalar field with matter, more specifically, on the function $\sigma(\phi)$. Consequently, the current amplitude of the scalar field ϕ_0 can differ from ϕ_R.

Thus, the coupling constants at the epoch of primordial nucleosynthesis can differ from their current values. However, they may be considered invariable during nucleosynthesis, which significantly simplifies the calculations of light-nuclide yields.

Note that a small (~10%) deviation of γ from 1/3 during the annihilation of electrons and positrons does not qualitatively change our assumptions and the subsequent calculations.

Let us introduce a coefficient $\delta \sim (\phi_R - \phi_0)$, which quantitatively characterizes the difference between the conformal factors, as follows:

$$W^2(\phi_0) = W^2(\phi_R)(1 + \delta). \qquad (12)$$

For the effect of δ on the yields of light elements to be elucidated, we must determine the δ dependence of the fundamental constants that play the key role in primordial nucleosynthesis. This dependence is different in the Jordan (JF) and Einstein (EF) frames. Since there is no consensus on which of these frames correspond to physical measurements, we analyze both alternatives.

In JF, according to Damour and Pichon (1999), the presence of a scalar field causes a change in the expansion rate of the Universe, which may be treated as a change in gravitational constant G, whereas the remaining coupling constants are invariable.

In EF, all coupling constants (3) change (see, e.g., Damour and Polyakov 1994; Campbell and Olive 1995). All four main interactions manifest themselves in full measure at different stages of primordial nucleosynthesis. Accordingly, we will consider the transformation laws for the coupling constants in EF.

Electromagnetic Interaction

The Lagrangian of the electromagnetic interaction that appears in action (2) is

$$\bar{\Psi}(\gamma^\mu D_\mu - m_\Psi)\Psi + \frac{1}{4}F_{\mu\nu}F^{\mu\nu}. \qquad (13)$$

This Lagrangian describes a fermion of mass m_Ψ interacting with an electromagnetic field described by tensor $F^{\mu\nu}$. After conformal transformation, the Lagrangian (13) in action (3) takes the form

$$\bar{\Psi}(\gamma^\mu D_\mu - W^{-1}(\phi)m_\Psi)\Psi + \frac{W^2(\phi)}{4}F_{\mu\nu}F^{\mu\nu}. \qquad (14)$$

In view of Eq. (12), this Lagrangian describes a fermion of mass $m_\Psi = m_\Psi^0 (1 + \delta)^{1/2}$ and charge $e = e^0(1 + \delta)^{1/2}$, i.e., for the fine-structure constant $\alpha = \alpha^0(1 + \delta)$.

Weak Interaction

Weak interaction is the most universal interaction after gravitation: whereas gravitation covers all particles, weak interaction extends at least to all fermions. In the low-energy limit, the weak reaction rates are proportional to the Fermi constant $G_F = 1.436 \times 10^{-49}$ erg cm^3. Actually, the Fermi constant is not a true coupling constant, and its physical meaning is defined in the electroweak theory [$SU_L(2) \otimes U(1)$]:

$$G_F = \frac{\sqrt{2}g^2}{8M_W^2} = \frac{1}{\sqrt{2}v^2}. \qquad (15)$$

Here, g is one of the two true coupling constants of electroweak interaction; M_W is the mass of the W-boson, the carrier of electroweak interaction, which, in turn, is also proportional to g: $M_W = gv/2$; and v is the vacuum mean of the Higgs fundamental scalar field, which is central to the electroweak theory (and is responsible for the generation of fermion masses).

Since the structure of the electroweak Lagrangian with respect to conformal transformation is similar to the electromagnetic Lagrangian, the dependencies of the coupling constants on the conformal factors are the same; i.e., $g = g_0(1 + \delta)^{1/2}$. The dependence of the vacuum mean v on the dilaton field is determined by the peculiarities of the vacuum symmetry breakdown mechanisms (possibly the compactification mechanisms). The latter have not been studied adequately at present and depend on the specific superstring model. We analyze the direct interaction of the dilaton field with the fields of matter determined solely by the factor $W(\phi)$ in action (3). The value of the function multiplied by a factor then changes, while the position of the extremum (which the value of v is for the Higgs scalar field) remains as before. In this approximation, G_F does not depend on the dilaton field.

Note, however, that the independence of the weak interaction constant on field ϕ does not mean that the weak reaction rates will not change. The key reactions (5), which determine the n/p ratio, depend not only on G_F but also on electron mass m_e and on difference Q between the neutron and proton masses (see, e.g., Lifshitz and Pitaevskii 1971). In turn, Q depends both on the change in neutron and proton masses and on the change in the intensity of electromagnetic interaction, i.e., on α. Thus, by changing α, we recalculated Q using the expression of Dixit and Sher (1988) and the neutron lifetime τ_n, on which the yields of light nuclides depend significantly.

Strong Interaction

The relative helium abundance is determined mainly by the neutron abundance at the time when the nuclear reaction rates increase. Since most of the neutrons in nuclear reaction transform to helium by combining with protons, the helium abundance depends weakly on changes in the strong interaction constant. This is clearly seen from Figs. 1 and 2. Obviously, even if all the deuterium is converted to helium at $\eta \gtrsim 2 \times 10^{-10}$, then the addition of Y_p will be $\lesssim 10^{-4}$. The relative abundances of deuterium, lithium, beryllium, and boron are more sensitive to the nuclear reaction rates, but here we may also disregard the effect of a change in the strong interaction constant compared to the effect of the electromagnetic interaction constant. This is possible, because the reactions for the radiative capture of neutrons by protons and deuterons are radiative processes and because the cross sections for the nuclear reactions involving charged particles are determined mainly by the Coulomb barrier. The temperature range at the nucleosynthesis peak is such that the Gamow factor $\exp(-\sqrt{E_G/E})$, which characterizes the subbarrier tunneling probability, is much smaller than unity (i.e., $E \sim kT < E_G$). Therefore, the nuclear reaction rates are exponentially sensitive to a change in the fine-structure constant α [$E_G = (2\pi\alpha Z_i Z_j)^2 \mu c^2/2$, where Z_i, Z_j, and μ are the charges and reduced mass of the nuclei involved in the reaction].

Gravitational Interaction

Gravitational interaction determines the expansion rate of the Universe and, consequently, the times when the balance is upset between the direct and reverse reactions. If the action is written in Einstein form (3), then G appearing in it is constant. However, this constant is not a true coupling constant. The analog of the fine-structure constant for gravitation is the relation

$$\alpha_G(m) \equiv \frac{Gm^2}{\hbar c} \simeq 6.707 \times 10^{-39}\left(\frac{m}{\mathrm{GeV}}\right)^2, \qquad (16)$$

where the mass acts as the gravitational charge. Since G always appears in combination Gm, the change in mass can be effectively described by a change in G.

Table 2 gives the resulting dependencies of fundamental constants on δ. The superscript 0 denotes the current values of the corresponding quantities. The δ dependence of Q was taken by using the results of Dixit and Sher (1988):

$$Q = Q^0(1 + \delta)^{1/2} - q_C\delta. \qquad (17)$$

The constant q_C determines the contribution of electromagnetic interaction to the difference Q between the neutron and proton masses, $q_C \approx 0.9$ MeV. The neutron lifetime was calculated from the standard formula (see, e.g., Lifshitz and Pitaevskii 1971) by taking into account the changes in Q and electron mass m_e.

RESULTS OF THE CALCULATIONS

Under our assumptions, we calculated the yields of primordial elements as a function of two parameters (η, δ) by using the dependencies from Table 2. The results of our calculations are shown in Figs. 4–6.

Table 2. The δ dependencies of constants

JF	EF
$G = G^0(1 + \delta)$	$G = G^0(1 + \delta)$
$\alpha = \alpha^0$	$\alpha = \alpha^0(1 + \delta)$
$m_\psi = m_\psi^0$	$m_\psi = m_\psi^0(1 + \delta)^{1/2}$
$G_F = G_F^0$	$G_F = G_F^0$

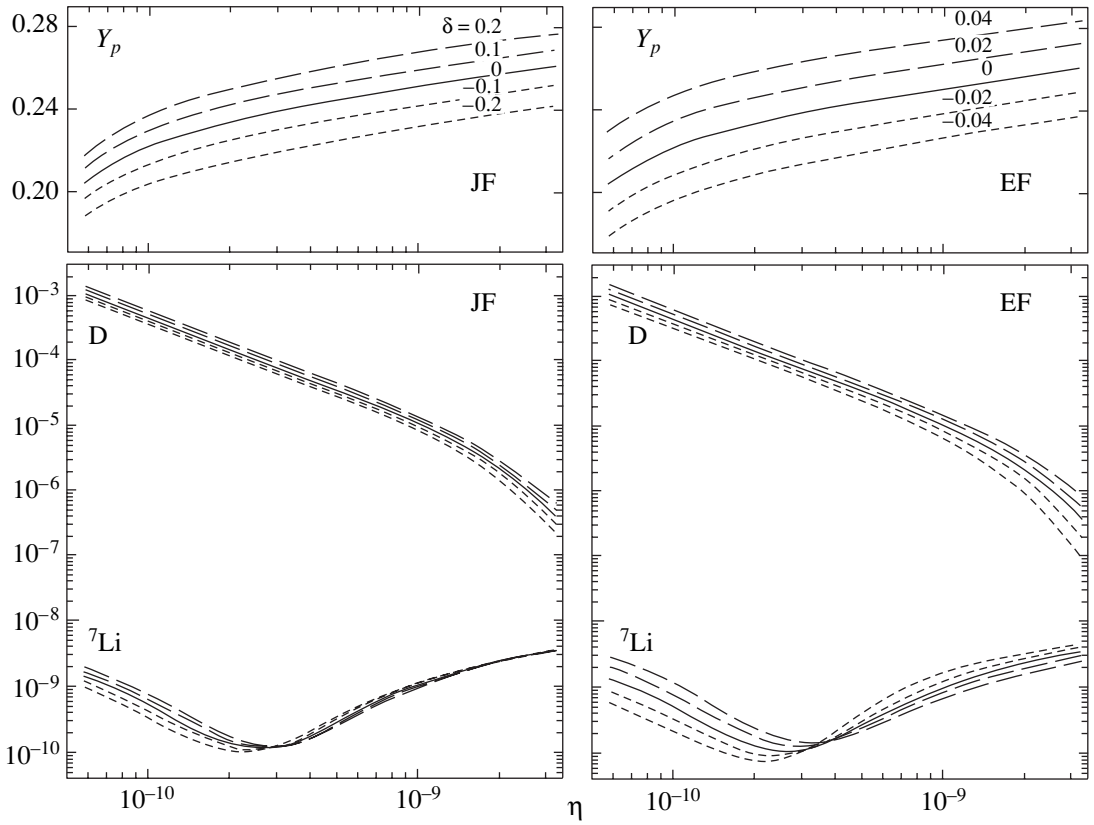

Fig. 4. Light-nuclide yields versus η for various δ indicated above the curves in JF and EF: $Y_p = m(^4\mathrm{He})/(m(\mathrm{H}) + m(^4\mathrm{He}))$, D = [D]/[H], and ^{7}Li = [^{7}Li]/[H].

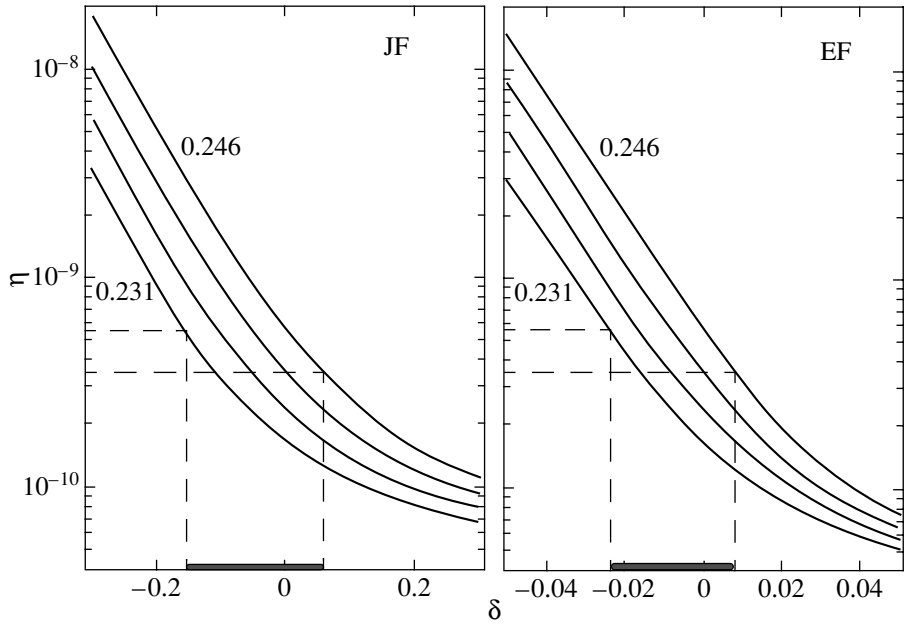

Fig. 5. Parameter η versus δ for various Y_p indicated near the curves for JF and EF.

We see from Fig. 4 that an increase (decrease) in δ at fixed Y_p causes a decrease (increase) in η, i.e., a change in the baryonic abundance Ω_B of the Universe [see formula (4)].

The equation $Y_p(\eta, \delta) = \mathrm{const}$ implicitly defines the relation between η and δ for which the change in the baryonic abundance of the Universe and the deviation of fundamental constants at the epoch of primordial

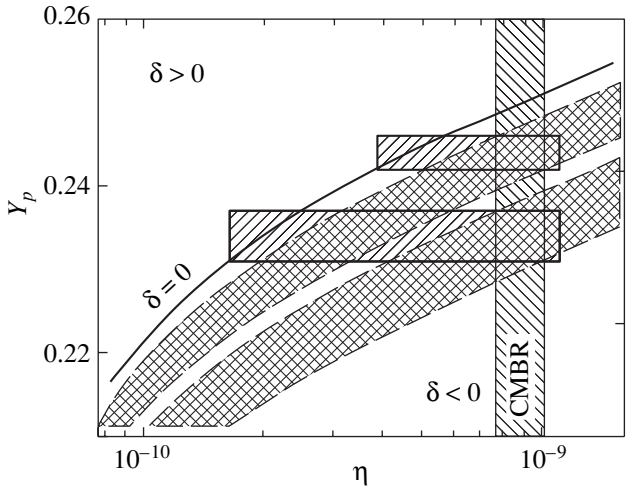

Fig. 6. The values of δ that simultaneously satisfy the CMBR anisotropy data and the ^{4}He(Y_p) data. The two hatched bands define the ranges of δ corresponding to its numerical values from Table 3.

nucleosynthesis from their current values agree are in agreement with observational data on the abundances of light elements.

In Fig. 5, η is plotted against δ for various Y_p = const in the range 0.231 to 0.246. This range covers the observational primordial-helium data from Olive *et al.* (1997) and Izotov and Thuan (1998) (Table 1). Variations in δ within 20% (JF) or 5% (EF) could, in principle, cause the baryonic abundance of the Universe to change by two or three orders of magnitude without coming into conflict with the helium data. However, the experimental data on primordial deuterium and lithium (Table 1) limit the range of η (i.e., Ω_B) and, accordingly, the range of δ. Therefore, the possible values of δ lie in the range from –0.15 to +0.06 (JF) or from –0.025 to 0.008 (EF).

In Fig. 6, Y_p is plotted against η for various δ. Also shown in this figure are the two experimental ranges $Y_p = 0.244 \pm 0.002$ and $Y_p = 0.234 \pm 0.003$. The vertical band correspond to η obtained by analyzing CMBR anisotropy data (acoustic peaks; Jaffe *et al.* 2000). The upper curve represents the standard primordial nucleosynthesis model (δ = 0); we see that this curve does not allow the CMBR data to be reconciled with the helium data. The hatched bands define the ranges of δ for which the CMBR data can be reconciled with the data of Izotov and Thuan (1998) or with those of Olive *et al.* (1997); the corresponding values of δ are given in Table 3.

Table 3. Admissible values of δ

	JF	EF
$Y_p = 0.244 \pm 0.002$	$-0.10 < \delta < -0.03$	$-0.015 < \delta < -0.005$
$Y_p = 0.234 \pm 0.003$	$-0.20 < \delta < -0.13$	$-0.032 < \delta < -0.019$

Note that the CMBR data give η for which the primordial deuterium abundance $\lesssim 10^{-5}$. In this case, deuterium must be additionally produced after the completion of primordial nucleosynthesis but before the formation of the quasar spectra in which deuterium is observed, i.e., in the range from $z \sim 10^9$ to $z \sim 3$.

CONCLUSION

(1) We have constructed a two-parameter model for primordial nucleosynthesis in which the first parameter η is the current baryon-to-photon density ratio and the second parameter δ characterizes the deviation of fundamental physical constants at the epoch of primordial nucleosynthesis from their current values. To solve the formulated problem, we developed a modified numerical code for computing the production of light nuclides, ^{2}D, ^{3}He, ^{4}He, ^{7}Li, and others during primordial nucleosynthesis.

(2) Using the equation $Y_p = f(\eta, \delta) = \text{const}$, which implicitly relates η and δ, we constructed an explicit function $\eta = f(\delta; Y_p)$. This function allows the relative baryonic density to be varied over a wide range ($\eta \in 10^{-10}$–10^{-8}), which corresponds to the baryonic abundance of the Universe from $\Omega_B \sim 0.01$ to $\Omega_B \sim 1$. Thus, when the constants vary, different values of Ω_B can correspond to the same helium abundance, which allows the primordial-helium data to be reconciled with the CMBR data (see, e.g., Jaffe *et al.* 2000).

(3) If the primordial deuterium and lithium data are also taken into account, then the admissible range of η and δ significantly narrows [here, we used the most typical ranges for deuterium $(3.8 \pm 1.5) \times 10^{-5}$ and for lithium $(1.5 \pm 0.5) \times 10^{-10}$], which corresponds to the relative baryonic density $\eta = (4.4 \pm 1.0) \times 10^{-10}$:

$$\begin{aligned} &\text{JF-frame:}\ -0.15 < \delta < 0.06, \\ &\text{EF-frame:}\ -0.25 < \delta < 0.008. \end{aligned} \qquad (18)$$

(4) The range of δ derived in our model (the constants change during the post-radiation expansion period of the Universe; i.e., $0 < z < 10^4$) agree with a recent result on the possible change in fine-structure constant, $\Delta\alpha/\alpha = (0.72 \pm 0.18) \times 10^{-5}$ for $0.5 < z < 3.5$ (Murphy *et al.* 2000).

In conclusion, note that primordial nucleosynthesis provides the most stringent constraints, $\Omega_B h^2 = 0.016 \pm 0.004$, and there have been no clear conflicts with the available observational data until recently. However, $\Omega_B h^2 = 0.032 \pm 0.005$ obtained by analyzing the CMBR fluctuation spectrum can serve as an indication that the standard primordial nucleosynthesis model must be modified. New experiments (MAP, PLANCK, and others) on more detailed CMBR anisotropy measurements are planned in the immediate future. A large number of cosmological parameters, including Ω_B, with an accuracy higher than several percent, are scheduled to be measured during these experiments. The baryonic abundance of the Universe obtained in this way (inde-

pendently of primordial nucleosynthesis estimates) will become a powerful means for testing primordial nucleosynthesis models for their consistency and self-consistency.

ACKNOWLEDGMENTS

We are grateful to A.A. Starobinsky and to the participants of an astrophysical workshop of the Dept. of Theoretical Astrophysics at the Ioffe Physicotechnical Institute. This study was supported by the Russian Foundation for Basic Research (project no. 99-02-18232), the State Science and Technology Program "Astronomy" (cosmomicrophysics), and the State Science and Technology Program "Fundamental Metrology."

REFERENCES

1. J. D. Barrow, Phys. Rev. D **35**, 1805 (1987).
2. L. Bergström, S. Iguri, and H. Rubinstein, Phys. Rev. D **60**, 045005 (1999).
3. P. Bonifacio and P. Molaro, Mon. Not. R. Astron. Soc. **285**, 847 (1997).
4. C. Brans and R. H. Dicke, Phys. Rev. **124**, 925 (1961).
5. S. Burles and D. Tytler, astro-ph/9803071 (1998).
6. A. M. Bykov, Space Sci. Rev. **74**, 397 (1995).
7. C. G. Callan, D. Friedan, E. J. Martinec, and M. J. Perry, Nucl. Phys. B **262**, 593 (1985).
8. C. G. Callan, I. R. Klebanov, and M. J. Perry, Nucl. Phys. B **278**, 78 (1986).
9. B. A. Campbell and K. A. Olive, Phys. Lett. B **345**, 429 (1995).
10. T. Damour and K. Nordtvedt, Phys. Rev. D **48**, 3436 (1993).
11. T. Damour and B. Pichon, Phys. Rev. D **59**, 123 502 (1999).
12. T. Damour and A. M. Polyakov, Nucl. Phys. B **423**, 532 (1994).
13. V. V. Dixit and M. Sher, Phys. Rev. D **37**, 1097 (1988).
14. E. S. Fradkin and A. A. Tseytlin, Phys. Lett. B **158**, 316 (1985).
15. N. Yu. Gnedin and J. P. Ostriker, Astrophys. J. **400**, 1 (1992).
16. M. Green, J. Schwarz, and E. Witten, *Superstring Theory* (Cambridge Univ. Press, Cambridge, 1987).
17. Yu. I. Izotov and T. X. Thuan, Astrophys. J. **500**, 188 (1998).
18. A. H. Jaffe, P. A. R. Ade, A. Balbi, *et al.*, astro-ph/0007333 (2000).
19. P. Jordan, Nature **164**, 637 (1949).
20. L. H. Kawano, Preprint FERMILAB-PUB-92/04-A (1992).
21. S. V. Ketov, *An Introduction to the Quantum Theory of Strings and Superstrings* (Nauka, Novosibirsk, 1990).
22. D. Kirkman, D. Tytler, S. Brules, *et al.*, astro-ph/9907128 (1999).
23. E. W. Kolb and M. S. Turner, *The Early Universe* (Addison-Wesley, Redwood City, 1990).
24. E. W. Kolb, M. J. Perry, and T. P. Walker, Phys. Rev. D **33**, 869 (1986).
25. S. A. Levshakov, astro-ph/9808295 (1998).
26. E. M. Lifshitz and L. P. Pitaevskii, *Relativistic Quantum Theory* (Nauka, Moscow, 1971; Pergamon, Oxford, 1971), Part 2.
27. C. Lovelace, Phys. Lett. B **135**, 75 (1984).
28. G. Magnano and L. M. Sokolowski, Phys. Rev. D **50**, 5039 (1994).
29. P. Molaro, P. Bonifacio, M. Centurion, and G. Vladilo, astro-ph/9908060 (1999).
30. A. Yu. Morozov, Usp. Fiz. Nauk **162** (8), 83 (1992) [Sov. Phys. Usp. **35**, 671 (1992)].
31. M. T. Murphy, J. K. Webb, V. V. Flambaum, *et al.*, astro-ph/0012419 (2000).
32. L. B. Okun', *Particle Physics* (Nauka, Moscow, 1984; Harwood, Chur, 1985).
33. L. B. Okun', Usp. Fiz. Nauk **168** (6), 625 (1998) [Phys. Usp. **41**, 553 (1998)].
34. K. A. Olive, G. Steigman, and E. D. Skillman, Astrophys. J. **483**, 788 (1997).
35. J. M. O'Meara, D. Tytler, D. Kirkman, *et al.*, astro-ph/0011179 (2000).
36. A. V. Orlov and D. A. Varshalovich, Preprint No. 1719, FTI im. A. F. Ioffe RAN (Ioffe Physicotechnical Institute, Russian Academy of Sciences, 1998).
37. A. M. Polyakov, *Gauge Fields and Strings* (Harwood Academic, Chur, 1987).
38. M. Rugers and C. J. Hogan, Astrophys. J. Lett. **459**, L1 (1996).
39. S. G. Ryan, T. C. Beers, K. A. Olive, *et al.*, Astrophys. J. Lett. **530**, L57 (2000).
40. D. I. Santiago, D. Kalligas, and R. V. Wagoner, Phys. Rev. D **56**, 7627 (1997).
41. M. S. Smith, L. H. Kawano, and R. A. Malaney, Astrophys. J., Suppl. Ser. **85**, 219 (1993).
42. T. R. Taylor and G. Veneziano, Phys. Lett. B **213**, 459 (1988).
43. R. V. Wagoner, Astrophys. J., Suppl. Ser. **18**, 247 (1969).
44. R. V. Wagoner, Phys. Rev. D **1**, 3209 (1970).
45. J. K. Webb, R. F. Carswell, K. M. Lanzetta, *et al.*, Nature **388**, 250 (1997).
46. J. K. Webb, V. V. Flambaum, C. W. Churchill, *et al.*, Phys. Rev. Lett. **82**, 884 (1999).
47. S. Weinberg, *Gravitation and Cosmology* (Wiley, New York, 1972).
48. C. M. Will, *Theory and Experiment in Gravitational Physics* (Cambridge Univ. Press, Cambridge, 1993).

Translated by V. Astakhov

Astronomy Letters, Vol. 27, No. 10, 2001, pp. 625–633. Translated from Pis'ma v Astronomicheskiĭ Zhurnal, Vol. 27, No. 10, 2001, pp. 735–745.

A Model of Particle Acceleration to High Energies by Multiple Supernova Explosions in OB Associations

A. M. Bykov[1] and I. N. Toptygin[2]*

[1] *Ioffe Physicotechnical Institute, Russian Academy of Sciences, ul. Politekhnicheskaya 26, St. Petersburg, 194021 Russia*
[2] *St. Petersburg State University, Universitetskaya nab. 7/9, St. Petersburg, 199164 Russia*

Received May 15, 2001

Abstract—The possibility of cosmic-ray (CR) acceleration to energies above 10^9 GeV per nucleus in extended Galactic OB associations is analyzed. A two-stage acceleration mechanism is justified: at the first stage, the acceleration by separate shock fronts from spatially and temporally correlated supernovae explosions takes place, and, at the second stage, the Fermi acceleration by supersonic turbulence in an extended, strongly perturbed region near the OB association takes place. We calculate the CR energy spectrum, the change in CR chemical composition with energy, and the energy dependence of the mean logarithm of atomic mass, $\langle \ln A \rangle$, for the accelerated particles. The calculated values are compared with those observed near the break in the energy spectrum. We estimate the turbulence parameters, which allow the observed features of the energy spectrum and the CR enrichment with heavy elements to be explained. *© 2001 MAIK "Nauka/Interperiodica".*

Key words: *cosmic rays, nonthermal radiation; supernovae and supernova remnants*

OBSERVATIONAL DATA AND STATEMENT OF THE PROBLEM

In recent years, observational data on the spectra and composition of high-energy cosmic rays (CRs) have shown that the current particle acceleration theory is not completely adequate and have necessitated the development of new acceleration models. Below, we briefly list the main observational data that were obtained in numerous experimental studies and that require an explanation (Khristiansen *et al.* 1995; Swordy 1994; Shibata 1996; Teshima 1994; Petrera 1996; Fomin *et al.* 1997; Glasmacher *et al.* 1999; Fortson *et al.* 1999). The spectra of CRs up to energies of 10^5 TeV were taken in balloon measurements (Russian–Japanese RUNJOB collaboration) by Apanasenko *et al.* (2001); these are power-law spectra without any features in this energy range. The index γ of the differential proton energy spectrum at energies $E = 10^2$–10^5 GeV per nucleon is approximately constant and close to $\gamma \approx 2.75$. The spectrum of heavy nuclei in the same energy range is flatter, and its index appears to be closer to $\gamma \approx 2.65$ (although the scatter of experimental data points is significant). These results were obtained both from observations of extended air showers and by direct measurements. At energies $E = 10^5$–10^7 GeV per nucleus, there is a feature (apparently a kink or a knee) in the CR energy spectrum summed over all nuclei. The shape of the feature has not been studied adequately; there may be a plateau or a nonmonotonic behavior. After the knee, the spectrum is again close to a power law with $\gamma \approx 3.1$–3.2 at energies $E \approx 10^7$–$10^{9.5}$ GeV per nucleus (Fortson *et al.* 1999; Teshima 1994; Bird *et al.* 1993; Bakatanov *et al.* 1992). The spectrum breaks at energy $E \approx 10^{9.5}$ GeV per nucleus, and $\gamma \approx 2.71 \pm 0.10$ at $E \approx 10^{9.5}$–$10^{10.6}$ GeV per nucleus (Bird *et al.* 1993).

The changes in spectral shape are apparently accompanied by a change in the Galactic CR composition and by an increase in the fraction of heavy nuclei with energy. This is suggested by the data in Table 1 and by recent measurements of the logarithm of atomic mass, $\langle \ln A \rangle$, averaged over the contributions from different groups of nuclei. According to the CASA–MIA team (Glasmacher *et al.* 1999) that measured the muon density of a shower as a function of its size from electrons, $\langle \ln A \rangle$ monotonically increases from about 1.2 at $E = 10^5$ GeV to 3.4 at $E = 10^7$ GeV. The KASKADE measurements, which took into account both muon and hadron shower characteristics, have shown that a break takes place only for light CR nuclei and that there is no evidence of a break in the heavy component up to 10^{17} eV (Kampert *et al.* 2001; see also Fig. 1, taken from this paper). According to the CASA–BLANCA team (Fortson *et al.* 1999), which used Cerenkov detectors, $\langle \ln A \rangle$ exhibits a nonmonotonic behavior: a decrease in the energy range 5×10^5 to 5×10^6 GeV and an increase at higher energies. The accuracy of determining the percentage abundances of various elements at high energies should not be overestimated. As yet no agreement has been reached on many issues between the various teams of researchers.

* E-mail address for contacts: INT@cosmos.hop.stu.neva.ru

Table 1. The nuclear composition of primary CRs at energies $E \le 10^5$ GeV

Nuclei	p	He	CNO	Ne–S	Fe group	Source
Z	1	2	6–8	10–16	≥26	
Energy, GeV per nucleus	10^5	10^5	10^5	10^5	10^5	
Energy, GeV per nucleon	10^5	2.5×10^4	7.1×10^3	4.2×10^3	1.2×10^3	
Percentage abundance, %	20	36	19	12	13	Swordy (1994)
Energy, GeV per nucleon	>2.5	>2.5	>2.5	>2.5	>2.5	
Percentage abundance, %	92	7	0.5	0.2	0.04	Syrovatskiĭ (1976)

Thus, for example, the Cerenkov detectors of the AIROBICC and HEGRA facilities, after applying corrections for systematic errors, give a CR composition consistent with the absence of any change in atomic mass with energy in the range $(0.3–10) \times 10^{15}$ eV (Argueros *et al.* 2000). The disagreement over the composition of primary CRs at extremely high energies is particularly serious. According to Bird *et al.* (1993), the composition dramatically changes at energies $E \approx 10^8$–10^{10} GeV per nucleus, from almost 100% of Fe to 100% of protons. However, this result is not confirmed by other investigators (Doi *et al.* 1995).

The above brief list of basic observational data on the spectral shape and composition of CRs shows that the situation at energies above 10^5 GeV is most difficult to explain. The available information about changes in the spectrum and chemical composition of high-energy particles suggests that either new sources switch on at high energies, which supply most of the particles of the corresponding energies, or the operating conditions of the same sources that generate lower energy particles change. The particle propagation conditions may also change with energy, causing the energy spectrum observed far from the sources to change (Berezinskiĭ *et al.* 1990).

Presently, most investigators consider the shock acceleration in a turbulent medium as the most likely generation mechanism for the majority of Galactic CRs. However, according to the most optimistic estimates, the acceleration by single shock waves from supernova explosions cannot account for the origin of the particles above the knee in the energy spectrum. Thus, for example, the analysis performed in Lagage and Cesarsky (1983), Fedorenko (1990), and many other papers (including models in which the turbulence level was calculated by using a self-consistent scheme

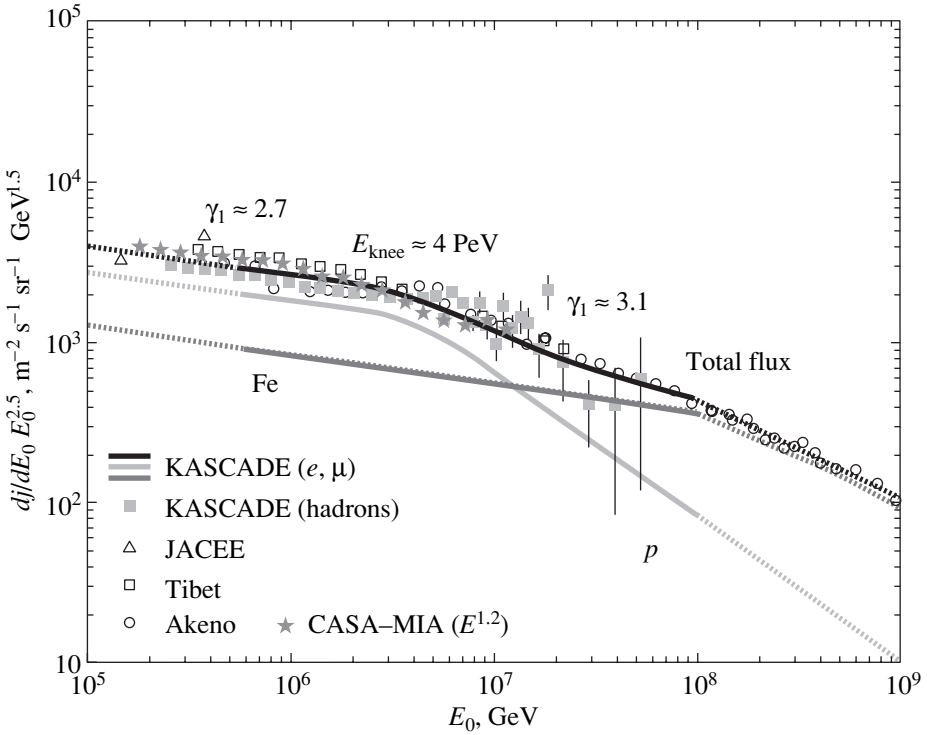

Fig. 1. The spectrum for all nuclei, as measured with various facilities, and the expected behavior of the proton and iron spectra (Kampert *et al.* 2001). Here, dj/dE_0 is the differential CR intensity related to the distribution function $F(E_0)$ used below by $dj/dE_0 = cF(E_0)$, where c is the speed of light.

for the generation of MHD waves by the accelerated particles) leads one to conclude that the maximum energy of the accelerated protons does not exceed 10^5–10^6 GeV. Volk and Biermann (1988) appear to give the highest maximum energy of $\sim(10^6$–$10^7)Z$ GeV. However, they had to make the following very optimistic assumptions: (1) at the presupernova stage, a strong stellar wind with a spiral magnetic field enhanced by many orders of magnitude compared to the mean interstellar field flowed out of the star; and (2) the explosion occurred in the stellar-wind region and the particle transport mean free path had the smallest possible (Bohm) value close to the gyroradius (see also Berezhko *et al.* 1996).

Calculations and observations (Lozinskaya 1986) show that the presupernova's stellar wind has a shell structure, which gives rise to several shock waves, forward and backward, in a young supernova remnant. Given that strong turbulence is quite possible in the presupernova's stellar-wind plasma, the model of particle acceleration by multiple shock fronts developed previously (Bykov and Toptygin 1990, 1993) may prove to be more adequate even for a single supernova explosion. The effect of shock-front multiplicity becomes particularly strong when we take into account the nonuniform distribution of supernovae in the disk and the temporal correlations of their explosions related to the synchronous evolution of stars in stellar associations (Bykov and Toptygin 1988).

Here, our goal is to further develop the model of CR acceleration in extended OB associations, whose preliminary analysis was performed previously (Bykov and Toptygin 1997). In our view, it would be most natural to interpret the experimental data presented above by assuming that the CRs are Galactic in origin up to energies of 3×10^9 GeV per nucleus, with the heavy nuclei prevailing at such energies. At the same time, the protons of extremely high energies $E > 3 \times 10^9$ GeV observed near the Earth are generated outside the Galaxy.

We estimated the energy parameters of OB associations that were important for the problem of CR acceleration. Of greatest importance are the magnetic-field strength, the intensity of turbulent pulsations, and their distribution in spatial scales. We restore the shape of the turbulence spectrum, which can account for the observed features in the accelerated-particle energy spectrum, and calculate the change in CR chemical composition when passing through the knee. This change is attributable to the change in the acceleration mechanism. The second change in the spectral shape and composition of CRs in our model takes place at higher energies and is caused by a reduction in the time of particle confinement in the acceleration region with increasing energy. We also calculated the shape of the particle spectrum near its cutoff, where the spectrum of Galactic sources appears to be joined with the spectrum of the particles accelerated outside the Galaxy. The changes in energy spectrum in our model are determined by the particle rigidity, which is in agreement with the data of Glasmacher *et al.* (1999).

A MODEL OF SUPERSONIC TURBULENCE IN OB ASSOCIATIONS

According to observational data (Lozinskaya 1986), a typical OB association produces a perturbed region 10^2–10^3 pc in size, whose lifetime is $\sim 10^7$ years. The perturbed state of the plasma inside the association and in its vicinity is produced by the winds from early-type stars at the presupernova stages and, in particular, by supernova explosions of massive stars. The frequency of explosions in a typical association is estimated to be 10^{-5}–10^{-6} per year. Since each supernova explosion takes place in the medium perturbed by the presupernova's stellar wind, we provide the basic parameters of the plasma in these regions.

According to Weaver *et al.* (1977), a multishell cavity with a radius R_c of ~30 pc filled with the stellar-wind and interstellar matter emerges within $\sim 10^6$ years after the onset of the outflow of a moderately intense ($\sim 10^{36}$ erg s^{-1}) stellar wind in the circumstellar medium (with a density of ~1 H atom cm^{-3}). At the same time, the pure stellar wind extends only to 6 pc; further out, there is the medium produced by its interaction and mixing with the surrounding matter. The mean particle number density in the cavity is $\sim 10^{-2}$ cm^{-3}. At the cavity boundary, the density rises to a value slightly higher than 1 cm^{-3}. Under these conditions, the mass of the matter inside the cavity is $\sim 15 M_\odot$. The cavity expands as a whole at a velocity of ~10 km s^{-1}.

For a supernova explosion with energy $\sim 10^{51}$ erg and ejected mass $\Delta M > M_\odot$, the medium may be considered cold, although its temperature is $\sim 10^6$ K (Weaver *et al.* 1977). Because of the nonuniform mass distribution in the cavity, the primary shock front generates a series of secondary perturbations. As the primary shock approaches the cavity boundary, the evolution of the remnant reaches the Sedov stage, because the mass of the matter swept up by the primary front will be close to or exceed the mass of the ejected envelope. Of considerable interest is the behavior of the shock wave from a supernova explosion at the cavity boundary, where the ambient density abruptly changes by a factor of ~100. Two shock waves, one passed into the interstellar medium and the other reflected deep into the cavity, diverge from this boundary. The contact discontinuity that emerges at the cavity boundary moves away from the star (Fig. 2). The parameters of the two shock fronts and the distribution of energy fluxes between them can be determined by using the conservation laws (Table 2).

We performed our calculations for a polytropic gas with a polytropic index $\gamma = 5/3$ by disregarding the magnetic field and the accelerated relativistic particles. The external shock wave (front I in Fig. 2) appears to be strong in most cases (Mach number $M_1 \gg 1$), because

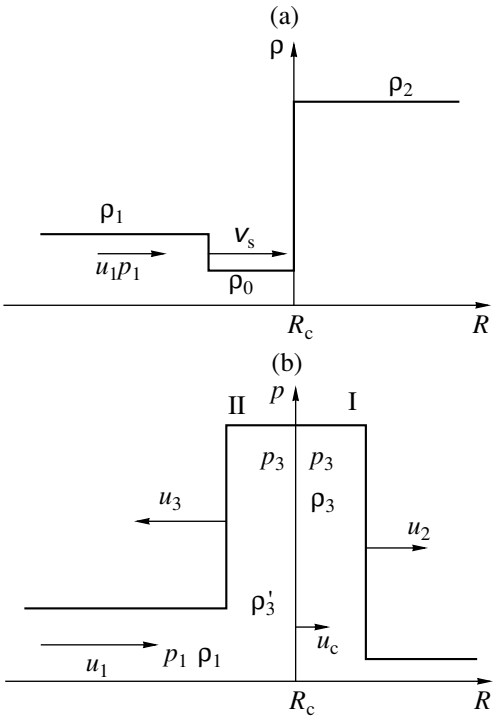

Fig. 2. The arrangement of discontinuities when the shock interacts with the density discontinuity: (a) before and (b) after the interaction. The velocities were determined in the frame of references associated with the star.

the temperature of the interstellar medium does not exceed 10^6 K. The internal shock wave (front II) exists in the gas already heated by the primary shock, and its Mach number M_2 cannot exceed $\sqrt{5}$ (see Table 2). The last column of the table gives the ratio of the energy flux through the external shock front outside the cavity boundary to the energy flux through the primary shock front inside the cavity:

$$\eta = \frac{\rho_2 u_2^3}{\rho_0 v_s^3},$$

Table 2. Interaction of the shock wave from a supernova explosion with the density discontinuity produced by stellar wind

ρ_2/ρ_0	p_3/p_1	M_2	ρ'_3/ρ_0	u_c/u_0	u_2/u_1	u_3/u_1	η
1	1.00	1.00	4.00	1.00	1.33		4.00
2	1.41	1.15	4.91	0.84	1.12	–0.14	1.19
5	2.08	1.37	6.14	0.65	0.86	0.02	1.34
10	2.65	1.52	6.98	0.52	0.69	0.14	1.37
20	3.23	1.67	7.70	0.40	0.54	0.24	1.30
50	3.95	1.83	8.45	0.28	0.37	0.37	1.11
100	4.41	1.93	8.87	0.21	0.28	0.44	0.93
1000	5.41	2.13	9.62	0.07	0.10	0.59	0.40
100 000	5.94	2.23	9.96	0.08	0.01	0.66	0.05

where $v_s = 4u_1/3$ is the front velocity of the strong primary shock in the cavity. It follows from Table 2 that, for overdensities at the cavity boundary $\rho_2/\rho_0 \le 100$, much of the wave energy passes into the ambient medium.

When the linear dimensions of the OB association are ~100 pc and when it contains 30 or 40 exploding stars, the mean separation between them is ~30–50 pc. This means that the cavities produced by stellar winds can be in contact and partially overlap and that supernova explosions will occur mostly in the tenuous medium of circumstellar cavities. Under these conditions, the shock fronts will interact and intersect to produce a strongly perturbed plasma region inside and near the stellar association. Assuming the mean density in a region with a radius of 100–150 pc to be ~10^{-2} m_H cm^{-3}, we find the total mass of the diffuse matter to be $10^3 M_\odot$. Such densities and total masses can apparently be taken as the basic parameters for the active stage of the association (~10^7 years). According to Lozinskaya (1986), the total mass transferred by the wind from a typical association over its lifetime is of the same order of magnitude. The matter swept up from the association is replenished by stellar winds and envelope ejections.

Random motions of plasma with shock fronts and with a wide range of spatial scales generate turbulent magnetic fields of the same scales; no special conditions like turbulence gyrotropy (Vaĭnshtein *et al.* 1980) are required for these fields to be generated. Let us estimate the magnetic energy as a fraction of the energy of turbulent motions:

$$\frac{B^2}{8\pi} = \xi \frac{10^{-2} m_p u^2}{2},$$

where ξ $(0 < \xi < 1)$ is the unknown conversion coefficient. Taking $u \approx (2\text{–}3) \times 10^8$ cm s^{-1} and $\xi \approx 0.05$ for the conversion coefficient, we obtain an estimate

$$B = (4\pi\xi \times 10^{-2} m_p u^2)^{1/2} \approx 3 \times 10^{-5} \text{ G}.$$

Given the complex multishell structure of the cavities produced by stellar winds, their sizes, and additional perturbations introduced by the ejected stellar matter, the most likely estimate for the scale sizes of typical inhomogeneities in the distribution of plasma velocities and magnetic fields is several parsecs, say, $L \approx 3\text{–}10$ pc.

PARTICLE ACCELERATION BY SUPERSONIC TURBULENCE IN OB ASSOCIATIONS

It follows from the above estimates and reasoning that a cavity with an OB association is a strongly perturbed region on time scales of several Myr that contains a random ensemble of shock fronts with various strengths, turbulent motions, and magnetic fields with a wide range of scales. We have developed the theory of particle acceleration in such systems previously (Bykov and Toptygin 1990, 1993).

If $v\Lambda/u \ll L$, where Λ is the local particle transport mean free path, v is the particle velocity, u is the characteristic front velocity, and L is the mean separation between the fronts, then the particles are accelerated, mainly independently, by separate shock fronts. The evolution of the accelerated-particle distribution function $F(r, p, t)$ averaged over the shock fronts and turbulent motions is described by the equation

$$\frac{\partial F}{\partial t} - \nabla_\alpha \kappa_{\alpha\beta} \nabla_\beta F = \left(\frac{1}{\tau_{sh}} + B\right)\hat{L}F + \frac{1}{p^2}\frac{\partial}{\partial p}p^2 D\frac{\partial F}{\partial p} + A\hat{L}^2 F + \frac{2}{3}B\hat{L}p\frac{\partial F}{\partial p}. \quad (1)$$

Here, $\kappa_{\alpha\beta}$ is the spatial diffusion tensor; the constant $\tau_{sh}^{-1} = \overline{\Delta u_n}/L$ is determined by the jump in hydrodynamic velocity at the shock fronts and by the mean separation between them; and A, B, and D are the kinetic coefficients, which are expressed in terms of the correlation functions of turbulent velocities. The operator

$$\hat{L}F = \frac{1}{p^2}\frac{\partial}{\partial p}\int_0^\infty G(p, p')F(p')dp' \quad (2)$$

describes the particle acceleration by a separate front, and Green's function $G(p, p')$ describes the spectrum transformation of the particles that fall on the shock front and are accelerated by it. In the test-particle approximation, Green's function is

$$G(p, p') = \begin{cases} ((\gamma + 2)/p')(p'/p)^{\gamma+2}\Theta(p - p'), & p \le p_m \\ 0, & p > p_m, \end{cases} \quad (3)$$

where γ is the spectral index for a separate front, and p_m is the maximum momentum to which the particles are accelerated by a single front. Expression (3) describes the formation of a spectrum with a single γ in the momentum range from p_0 (injection momentum) to p_m. The spectral index is determined by the compression ratio at the shock front:

$$\gamma = \frac{\sigma + 2}{\sigma - 1}, \quad \sigma = \rho_2/\rho_1. \quad (4)$$

The effect of the relativistic accelerated particles on the shock front causes the general plasma compression at the shock transition to increase, but it is now distributed between the sharp thermal discontinuity and the prefront, the region where the plasma flow incident on the front smoothly decelerates. The prefront width is $v\Lambda/u$, and the change in velocity at the prefront depends on the shock strength and on the accelerated-particle density. In this case, simple analytic expressions cannot be derived for Green's function (see, e.g., Toptygin 1997), but the nonlinear deformation of the front profile in the system under consideration is apparently negligible. This is because of the presumed multiplicity of the shock fronts, which are produced by the fragmentation of a small number of primary strong shock fronts and, therefore, have moderate Mach numbers.

Our estimates given below show that the particle acceleration time for the conditions under consideration is two or three orders of magnitude shorter than the lifetime of the stellar association itself at its active evolutionary phase. Therefore, in the particle acceleration problem, we may assume steady-state supersonic turbulence in the association and in its vicinity and use Eq. (1) in the steady-state form. An analysis of its solutions (Bykov and Toptygin 1990) indicates that under typical conditions and for relativistic particle energies, the particle acceleration by shock fronts play, a major role. The Fermi term with coefficient D can be very important only at nonrelativistic energies (Bykov and Fleĭshman 1992). It also becomes significant at high particle energies, when each particle simultaneously interacts with several fronts during the acceleration (see below).

Apart from isolated sharp shock fronts, there is small-scale turbulence in the system, which forms the local transport mean free path of the accelerated particles. This turbulence is produced by weak shock waves and by linear MHD modes of various types, which can be amplified at shock fronts (Bykov and Ushakov 1986). According to specific calculations and general views of the MHD turbulence properties (Vaĭnshtein *et al.* 1993), one might expect a power-law spectrum with index $\nu = 3/2$–$5/3$ on relatively small scales. The smaller and larger values from this range correspond, respectively, to weak MHD turbulence and to Kolmogorov homogeneous, isotropic turbulence in the approximation of an incompressible medium. The transport mean free path formed by such turbulence increases with energy and can be roughly estimated from the formula (Toptygin 1985)

$$\Lambda(E) \approx l_0\left(\frac{r_g}{l_0}\right)^{2-\nu}\frac{B_0^2}{\langle B_{st}^2\rangle}, \quad (5)$$

where l_0 is the main (maximum) scale of small-scale turbulence, B_0 is the large-scale field, B_{st}^2 is the turbulent field on scale l_0,

$$r_g = \frac{E}{Z_{eff}eB_0} \quad (6)$$

is the gyroradius of the accelerated ion, E is its energy, $v \approx c$, and Z_{eff} is the charge number of the accelerated ion.

When the equality

$$c\Lambda(E_*)/uL \approx 1, \quad (7)$$

which determines a characteristic energy E_*, is reached, the particle acceleration mechanism changes in our model. Isolated, moderately strong fronts play a major role at $E < E_*$. In the test-particle approximation,

they generate a power-law spectrum with index γ, the same for ions with any Z, in a medium with small-scale turbulence. However, allowance for nonlinearity may lead to slightly differing spectral indices for the nuclei with different Z at the same energy per nucleon.

The particles with energies $E > E_*$ simultaneously interact with several fronts and rarefaction regions between them during the acceleration; i.e., the ordinary Fermi acceleration by large-scale turbulence takes place. Thus, in our model, the acceleration mechanism changes near energy E_*, and it would be natural to associate the knee in the CR spectrum at $E \approx 10^6$ GeV with this peculiarity of the model. Note that the transport mean free path is determined by the particle rigidity

$$\rho = \frac{p}{eZ_{\rm eff}} \approx \frac{E}{ceZ_{\rm eff}}.$$

Therefore, the acceleration mechanism will change at the same rigidity but at different energies of the nuclei with different $Z_{\rm eff}$, and the change in energy spectrum will be accompanied by a change in the chemical composition of the energetic particles with energy.

At high energies, $E > E_*$, at which the purely Fermi acceleration remains, the particle distribution function satisfies the equation

$$\frac{\partial F}{\partial t} - \nabla_\alpha \kappa_{\alpha\beta} \nabla_\beta F = \frac{1}{p^2}\frac{\partial}{\partial p} p^2 D \frac{\partial F}{\partial p}, \quad (8)$$

where the diffusion coefficient in momentum space $D(p)$ must now include the total velocity field as well as the shock fronts. Assuming the spatial diffusion to be isotropic, we represent $D(p)$ as (Bykov and Toptygin 1990)

$$D(p) = \frac{\langle u^2 \rangle p^2}{9\kappa} = \frac{p^2}{\tau_a}, \quad (9)$$

where $\langle u^2 \rangle$ is the mean square velocity in the system and κ is the coefficient of spatial diffusion (which does not depend on momentum in the purely Fermi case). The Fermi acceleration time scale is $\tau_a = 9\kappa/\langle u^2 \rangle = \text{const}$.

The steady-state equation (8),

$$\frac{\tau_a \kappa}{r^2}\frac{\partial}{\partial r} r^2 \frac{\partial F}{\partial r} + \frac{1}{p^2}\frac{\partial}{\partial p} p^4 \frac{\partial F}{\partial p} = 0 \quad (10)$$

allows for the separation of variables under the assumption of spherical symmetry and isotropy of the system:

$$F(r, p) = f(p)\chi(r)/r. \quad (11)$$

The solutions are

$$\chi(r) = \sin kr, \quad f(p) = Cp^{-(\gamma+2)}, \quad (12)$$

where k and $\lambda = \kappa\tau_a k^2$ are constants and

$$\gamma = -\frac{1}{2} + \left(\frac{9}{4} + \lambda\right)^{1/2} \quad (13)$$

is the index of the particle energy spectrum at high energies ($p > p_*$). The constant C can be determined from the condition of joining this solution with the solution of Eq. (1) at $p < p_*$.

The possible values of k can be determined from the conditions at the $r = R$ boundary of the acceleration region. If the external region ($r > R$) is assumed to differ from the internal region ($r < R$) only by the absence of significant velocity fluctuations, $\langle u^2 \rangle = 0$, if the coefficients of spatial diffusion in the two regions are close in magnitude, and if we join the distribution functions and diffusive flows at $r = R$, then we obtain the condition

$$\cos kR = 0, \quad k_n = \frac{\pi}{2R}(2n+1), \quad n = 0, 1, \ldots. \quad (14)$$

The particle spectral index is determined by the smallest $k = \pi/2R$. Using equality (13) and specifying an experimental value $\gamma = 3.1$–3.2, we find the values of λ needed to explain the experiment:

$$\lambda = \kappa\tau_a k^2 = \frac{9\kappa^2 k^2}{\langle u^2 \rangle} = 10.71\text{–}11.44. \quad (15)$$

We use the observationally confirmed velocity of the shock fronts $u \approx 3 \times 10^8$ cm s^{-1} and the mean separation between them in an OB association and in its vicinity $L \approx 3$ pc $\approx 10^{19}$ cm. The particle transport mean free path for $r_g < L$ can then be roughly estimated as

$$\Lambda \approx L, \quad \kappa = \frac{c\Lambda}{3} \approx \frac{cL}{3}, \quad (16)$$

which follows from the fact that the strong scatterers (shock fronts) are separated, on average, by distance L. At $r_g > L$, the transport mean free path rapidly increases with energy, $\Lambda \propto p^2$, and the acceleration efficiency decreases. Thus, the condition $r_g \approx L$ in this model determines the energy above which a turnover of the energy spectrum occurs:

$$E_{\rm m} \approx Z_{\rm eff} e B_0 L. \quad (17)$$

We take a moderate estimate for the mean magnetic field in the perturbed region with multiple shock waves, $B_0 \approx 3 \times 10^{-5}$ G, when its energy is several times lower than the equipartition energy. This gives $E_{\rm m} \approx 10^8$ GeV for protons if $L \approx 3$ pc.

Using formula (16), we estimate the ratio of separation L between the fronts to system size R:

$$\frac{L}{R} \approx 2\frac{u}{c} \approx 0.02,$$

which gives $R \approx 150$ pc for the strongly turbulized region near the OB association. This estimate fits into the range of observable linear dimensions of hot cavities and superbubbles. The Fermi acceleration time scale is $\tau_a \approx 10^6$ years, which is of the order of or shorter than the time it takes for an ensemble of shock waves to

be formed in an association. The time of the preceding acceleration stage (at separate shock fronts) is shorter by two more orders of magnitude, because the local diffusion coefficient is small. We may therefore assume steady-state turbulence on acceleration time scales.

Let us now return to lower energies, at which the knee is observed in the spectrum. An abrupt increase in the particle transport mean free path from $\Lambda_* \approx l_0 B_0^2/\langle B_{st}^2\rangle$ at $r_g \approx l_0$ [$E = E_*$, see (6)] to $L \gg \Lambda_*$ at $E \gg E_*$ is required for the energy spectra with $\gamma = 2.7$ and 3.1–3.2 to be smoothly joined. Let us specify the beginning of the knee in the spectrum for protons, $E_{p*} = 3 \times 10^6$ GeV, in accordance with observational data. Then, $l_0 \approx r_{g*} = E_{p*}/eB_0 \approx 0.03$ pc. We find from (7) that

$$\Lambda_* \approx \frac{u}{c} L,$$

which allows the ratio of the magnetic energy of small-scale turbulence to the energy of the large-scale magnetic field to be determined: $\langle B_{st}^2\rangle/B_0^2 \approx 1$. However, in order for small-scale turbulence to weakly affect the high-energy particles, $E > E_*$, and not distort their energy spectrum with $\gamma \approx 3.1$–3.2, a cutoff or an appreciable dip in the turbulence spectrum on scales $l_0 \approx 10^{-2}$ pc is required. As a result, we obtain the shape of the turbulence spectrum in an association shown in Fig. 3. On scales $l > l_0$, either a field with broken-mirror structure with linear dimensions of individual regions L (single-scale spectrum) or a set of weak shock waves similar to that considered previously (Bykov and Toptygin 1987) can provide the required energy dependence of the particle transport mean free path. Such turbulence has a spectrum proportional to k^{-2}, which provides a constant particle transport mean free path $\Lambda \approx L$. There is small-scale ($l < l_0$) Kolmogorov ($\nu = 5/3$), MHD ($\nu = 3/2$), or mixed turbulence against this large-scale background.

In the transition region, the change in the acceleration mechanism causes the spectral index $\gamma(E)$ to change from $\gamma_1 \approx 2.7$ to $\gamma_2 \approx 3.1$–3.2, which can be approximated by a smeared step:

$$\gamma(E) = \frac{2\gamma}{1 + \gamma_1/\gamma_2 + (1 - \gamma_1/\gamma_2)\tanh[(E_* - E)/\Delta E]}. \quad (18)$$

Here, E_* is the energy at which the spectrum bends, and ΔE is the width of the transition region ($\sim E_*$).

In this case, the transport mean free path of the accelerated particles increases to $\Lambda \approx L$ (Fig. 4) and remains constant up to energies E_m; thereafter, it again increases for $E \gg E_m$ as $\Lambda(E) = L(E/E_m)^2$. At these energies, the particle momentum distribution function satisfies the equation

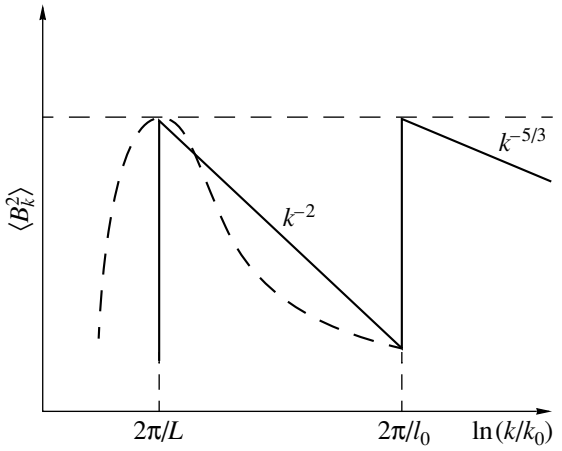

Fig. 3. The shape of the turbulent spectrum in an OB association that provides the observed shape of the energy spectrum and composition of high-energy CRs.

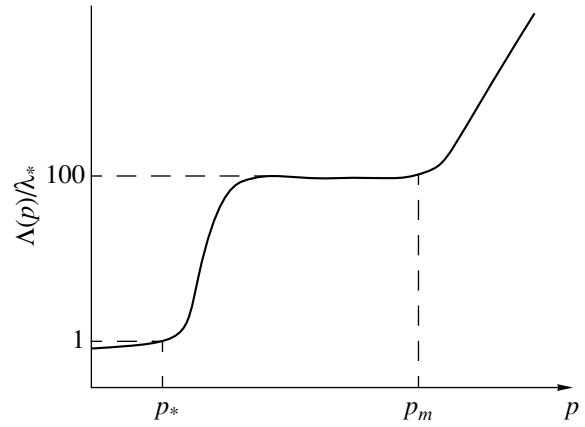

Fig. 4. Transport mean free path versus momentum (arbitrary units).

$$\left(\frac{p_m}{p}\right)^4 \frac{d}{dp} p^2 \frac{df}{dp} - \lambda f = 0, \quad (19)$$

where $p_m = E_m/c$. Its solution is

$$f(p) = A\left(\frac{p_0}{p}\right)^{1/2} K_{1/4}(\sqrt{\lambda} p^2/2), \quad (20)$$

where K_ν is the Macdonald function and A is the integration constant. Figure 5 (upper curve) shows the spectrum that is formed in our acceleration model for the nuclei with all Z. As the initial composition below the knee ($E \approx 10^5$ GeV), we took the composition from Swordy (1994) enriched with heavy elements (see Table 1). Because of the high photoionization probability in the vicinity of early-type hot stars, all nuclei, including iron, were assumed to be completely ionized; i.e., $Z_{eff} = Z$. The lower curve in Fig. 5 was constructed for a purely proton CR composition. The spectral shape

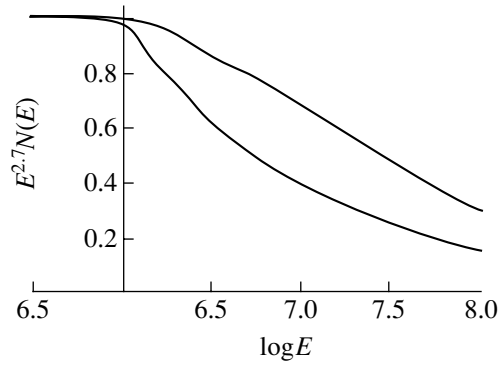

Fig. 5. The shape of differential energy spectrum $N(E)$ near the knee. $E^{2.7}N(E)$ related to $E^{2.7}N(E)|_{E = 10^6\ \mathrm{GeV}}$ and log$E$ (GeV) are along the vertical and horizontal axes, respectively. The upper and lower curves represent the nuclei with all Z and a purely proton spectrum, respectively. The spectral index changes from $\gamma = 2.7$ to 3.1 when passing through the knee.

for the nuclei with all Z at energies above 10^8 GeV is shown in Fig. 6.

CR ENRICHMENT WITH HEAVY ELEMENTS AT HIGH ENERGIES

In our model, the particle acceleration regime changes at some rigidities that depend on model parameters, $\rho_* = p_*/eZ$ and $\rho_m = p_m/eZ$. For the nuclei with different charge numbers, the energies of the transition from one regime to another are proportional to Z. Since the steepening of the spectrum increases during each change in regime, the relative contribution of heavy nuclei will increase twice: at $E_* = eZ\rho_*$ and at $E_m = eZ\rho_m$. Figure 7 illustrates the heavy-element enrichment of the spectrum as it bends. The first feature in the curve for protons is attributable to the change in the acceleration regime, and the second feature is attributable to the particle escape from the acceleration region. For iron, the two effects manifest themselves at high energies. The ratios of the spectra for the elements with charge numbers $Z_1 < Z_2$ before and after the bend can be expressed as

$$\left(\frac{F_{Z_1}(E)}{F_{Z_2}(E)}\right)_{E > E_{Z_2}^*} = \left(\frac{F_{Z_1}(E)}{F_{Z_2}(E)}\right)_{E > E_{Z_1}^*}\left(\frac{Z_2}{Z_1}\right)^{\gamma_2 - \gamma_1}. \qquad (21)$$

The largest energy E_m at which the transport mean free path Λ still retains a constant L belongs to iron. For the above parameters of the system,

$$E_{\mathrm{Fe}\,m} \approx 2.6 \times 10^9\ \mathrm{GeV},$$

which roughly corresponds to the highest energy Galactic particles (Bird *et al.* 1993). Since, according to (20), the distribution function at $E > E_m$ decreases exponentially, a 100% iron enrichment of CRs takes place in our model at $E > 3 \times 10^9$ GeV.

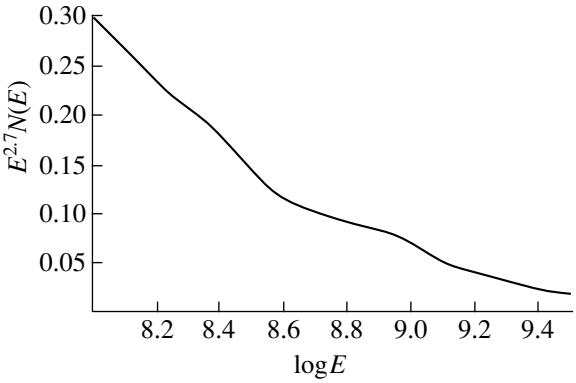

Fig. 6. The energy spectrum for all particles at energies $E > 10^8$ GeV.

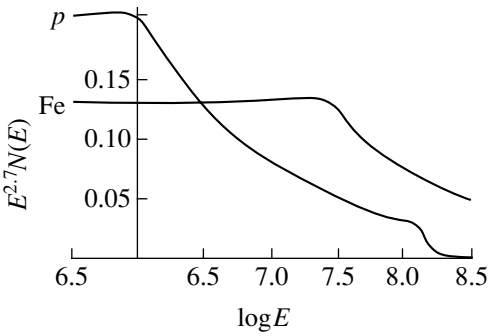

Fig. 7. The change in the percentages of protons and iron when passing through the knee in the spectrum. The same quantities as in Fig. 5 are along the axes.

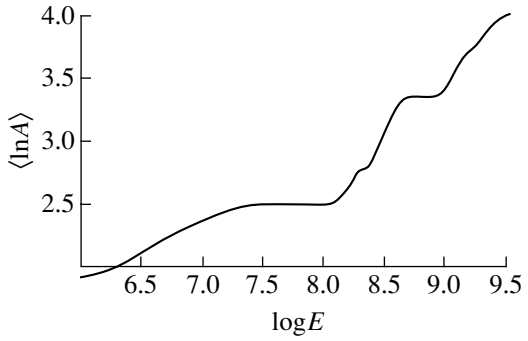

Fig. 8. The logarithm of atomic mass, $\langle \ln A \rangle$, averaged over the percentage abundance of the groups of nuclei versus energy.

The general change in the percentage abundances of various groups of nuclei in CRs with energy is given in Table 3. A plot of $\langle \ln A \rangle$ against energy is shown in Fig. 8. The smooth part of the curve from 10^6 to 10^8 GeV reflects the fact the composition becomes heavier after the change in acceleration regime; the step energy dependence at $E > 10^8$ GeV results from the sequential losses of light elements from the CR composition because of the predominant escape of light particles.

Table 3. Change in the percentages of the groups of nuclei in primary CRs with energy calculated for $E_* = 3 \times 10^6$ GeV, $\Delta E = 0.33E_*$, and $\gamma_2 = 3.2$, except the first row, where the data of Swordy (1994) are given

Energy, GeV per nucleus	p	He	CNO	Ne–S	Fe group
$10^{5.5}$	20	36	19	12	13
10^6	20	36	19	12	13
$10^{6.5}$	13	34	23	14	16
10^7	10	25	25	19	21
10^8	9	22	22	19	28
$10^{8.5}$	0	13	27	24	36
10^9	0	0	24	30	46
$10^{9.5}$	0	0	0	1	99

CONCLUSION

We have presented a model of CR acceleration in the Galaxy that can account for the generation of extremely-high-energy particles in extended (~150 pc in size) OB associations (Galactic superbubbles). The model relies on the available observational data and allows the spectral shape and chemical composition of particles at energies above the knee in the spectrum to be predicted from the measured values for energies 10^4–10^5 GeV per nucleus.

ACKNOWLEDGMENTS

This study was supported by the Russian Foundation for Basic Research (project nos. 98-02-17711 and 01-02-16654) and the Program of the Ministry of Education of Russia "Russian Universities—Basic Research" (project no. 015.02.01.01).

REFERENCES

1. A. V. Apanasenko, Z. Vatanabe, V. I. Galkin, *et al.*, Izv. Akad. Nauk, Ser. Fiz. **65**, 433 (2001).
2. F. Argueros, J. A. Barrio, and K. Bernlohr, Astron. Astrophys. **359**, 682 (2000).
3. V. N. Bakatanov, S. N. Bodnev, Yu. F. Novosel'tsev, *et al.*, Pis'ma Zh. Éksp. Teor. Fiz. **56**, 237 (1992) [JETP Lett. **56**, 231 (1992)].
4. E. G. Berezhko, V. K. Elshin, and L. E. Ksenofontov, Zh. Éksp. Teor. Fiz. **109**, 3 (1996) [JETP **82**, 1 (1996)].
5. V. S. Berezinskiĭ, S. V. Bulanov, V. L. Ginzburg, V. A. Dogel', and V. S. Ptuskin, *Cosmic-Ray Astrophysics* (Nauka, Moscow, 1990).
6. D. J. Bird, S. C. Corbato, H. Y. Dai, *et al.*, Phys. Rev. Lett. **71**, 3401 (1993).
7. A. M. Bykov and G. D. Fleĭshman, Pis'ma Astron. Zh. **18**, 234 (1992) [Sov. Astron. Lett. **18**, 95 (1992)].
8. A. M. Bykov and I. N. Toptygin, Astrophys. Space Sci. **138**, 341 (1987).
9. A. M. Bykov and I. N. Toptygin, Izv. Akad. Nauk SSSR, Ser. Fiz. **52**, 2290 (1988).
10. A. M. Bykov and I. N. Toptygin, Zh. Éksp. Teor. Fiz. **98**, 1255 (1990) [Sov. Phys. JETP **71**, 702 (1990)].
11. A. M. Bykov and I. N. Toptygin, Usp. Fiz. Nauk **163** (11), 19 (1993) [Phys. Usp. **36**, 1020 (1993)].
12. A. M. Bykov and I. N. Toptygin, in *Proceedings of the 25th International Cosmic Ray Conference, Durban, 1997*, Vol. 4, p. 365.
13. A. M. Bykov and A. Yu. Ushakov, Preprint No. 1059, FTI im. A. F. Ioffe (Ioffe Physicotechnical Institute, Leningrad, 1986).
14. T. Doi, N. Hayashida, K. Honda, *et al.*, in *Proceedings of the 24th International Cosmic Ray Conference, Roma, 1995*, Vol. 2, p. 685.
15. V. N. Fedorenko, Preprint No. 1442, FTI im. A. F. Ioffe (Ioffe Physicotechnical Institute, Leningrad, 1990).
16. Yu. A. Fomin, N. N. Kalmykov, G. B. Khristiansen, *et al.*, in *Proceedings of the 25th International Cosmic Ray Conference, Durban, 1997*, Vol. 4, p. 17.
17. L. F. Fortson, J. W. Fowler, C. H. Jui, *et al.*, in *Proceedings of the 26th International Cosmic Ray Conference, Salt Lake City, 1999*, Vol. 3, p. 125.
18. M. A. K. Glasmacher, M. A. Catanese, M. C. Chantell, *et al.*, in *Proceedings of the 26th International Cosmic Ray Conference, Salt Lake City, 1999*, Vol. 3, p. 129.
19. K.-H. Kampert, T. Antoni, W. D. Apel, *et al.*, astro-ph/0102266 (2001).
20. G. B. Khristiansen, Yu. A. Fomin, N. N. Kalmykov, *et al.*, in *Proceedings of the 24th International Cosmic Ray Conference, Roma, 1995*, Vol. 2, p. 772.
21. P. O. Lagage and C. J. Cesarsky, Astron. Astrophys. **125**, 249 (1983).
22. T. A. Lozinskaya, *Supernovae and Stellar Wind: Interaction with Galactic Gas* (Nauka, Moscow, 1986).
23. S. Petrera, Nuovo Cimento C **19**, 737 (1996).
24. T. Shibata, Nuovo Cimento C **19**, 713 (1996).
25. S. Swordy, in *Proceedings of the 23rd International Cosmic Ray Conference (Invited, Rapporteur, and Highligth Papers)* (World Scientific, Singapore, 1994), p. 243.
26. S. I. Syrovatskiĭ, Pis'ma Astron. Zh. **2**, 35 (1976) [Sov. Astron. Lett. **2**, 13 (1976)].
27. M. Teshima, in *Proceedings of the 23rd International Cosmic Ray Conference (Invited, Rapporteur, and Highlight Papers)* (World Scientific, Singapore, 1994), p. 257.
28. I. N. Toptygin, *Cosmic Rays in Interplanetary Magnetic Fields* (D. Reidel, Dordrecht, 1985).
29. I. N. Toptygin, Zh. Éksp. Teor. Fiz. **112**, 1584 (1997) [JETP **85**, 862 (1997)].
30. S. I. Vaĭnshteĭn, Ya. B. Zel'dovich, and A. A. Ruzmaĭkin, *Turbulent Dynamo in Astrophysics* (Nauka, Moscow, 1980).
31. S. I. Vaĭnshtein, A. M. Bykov, and I. N. Toptygin, *Turbulence, Current Sheets and Shocks in Cosmic Plasma* (Gordon and Breach, Langhorn, 1993).
32. H. J. Volk and P. L. Biermann, Astrophys. J. Lett. **333**, L65 (1988).
33. R. Weaver, R. McCray, J. Castor, *et al.*, Astrophys. J. **218**, 377 (1977).

Translated by V. Astakhov

Astronomy Letters, Vol. 27, No. 10, 2001, pp. 634–644. Translated from Pis'ma v Astronomicheskiĭ Zhurnal, Vol. 27, No. 10, 2001, pp. 746–757.

Atmospheric Iron Abundance in the Primary Component of υ Sgr

V. V. Leushin*

Special Astrophysical Observatory, Russian Academy of Sciences, Nizhniĭ Arkhyz, Stavropolskiĭ Krai, 357147 Russia

Received February 14, 2001

Abstract—Based on the observed energy distribution and line spectrum of the primary component of the binary υ Sgr, we computed blanketed model atmospheres. The atmospheric iron abundance in the primary component of υ Sgr was derived from photographic and CCD spectra. Our analysis confirmed the previously inferred $T_{\rm eff} = 13500 \pm 150$ K and $\log g = 2.0 \pm 0.5$. The microturbulent velocity was found from spectral lines in different spectral ranges to be $V_{\rm t} = 8$–12 km s^{-1}. We refined the mass fractions of light elements: 10^{-4} for H, 0.91 for He, 0.013 for C, 0.049 for N, and 0.008 for O. The iron abundance was determined with a high accuracy from Fe I, Fe II, and Fe III lines in the spectral range 4000–7000 Å: $\log(N({\rm Fe})/\Sigma N_i) = -3.80 \pm 0.20$.

Key words: *stars—variable and peculiar*

1. INTRODUCTION

Basic data on the chemical composition of stellar atmospheres and conclusions about its evolution in stars have been drawn from observed photographic spectra. A detailed history of the chemical evolution of the primary component in the eclipsing and spectroscopic binary υ Sgr (Leushin *et al.* 1997a) has also been determined by analyzing its photographic spectra. At the same time, some peculiarities of the processes included in calculations of the nuclear evolution of matter at the center of the binary's primary component are based on observational effects determined with insufficient accuracy, because it is objectively impossible to obtain accurate data from photographic observations. The binary υ Sgr is at the evolutionary stage associated with the formation and ejection of a helium envelope from its primary component. The binary is difficult to analyze because of its structure and current evolutionary status. It was established (Leushin *et al.* 1998) that υ Sgr appeared on the main sequence 52 Myr ago and consisted of $7M_\odot$ and $4M_\odot$ components. At that time, the components' chemical composition differed only slightly from the solar one, if at all. By now, the primary component with the initial mass of $7M_\odot$ has evolved from the main sequence to a helium giant. The $4M_\odot$ secondary component is still on the main sequence, because the evolution time of $4M_\odot$ main-sequence stars is 200–300 Myr. Five million years ago, the primary component had not yet lost its thick hydrogen envelope (the mass of the latter was $4.5M_\odot$) and had two nuclear burning zones: (1) helium-burning zone at the boundary of a carbon-oxygen-neon core and (2) hydrogen-burning zone at the upper boundary of the helium shell above the core. The nuclear burning in these layers proceeded with weak mixing over the entire helium shell. This nuclear process with the simultaneous loss of the hydrogen envelope lasted about 10 000 years. As a result, the system transformed into a binary composed of a main-sequence ($4M_\odot$) star and a helium giant with a mass of $2.5M_\odot$ and radius of 40–$50R_\odot$ at the second stage of Roche-lobe filling with the helium envelope. In addition, the system also contains part of the mass ejected by the primary component during the first Roche-lobe filling. Thus, at least four components form the spectrum of υ Sgr: the primary ($T_{\rm eff} = 13\,500 \pm 150$ K, $\log g = 2.0 \pm 0.5$), the secondary ($T_{\rm eff}$ =15000–20000 K), the interstellar medium produced by the first envelope ejection, and the matter that is leaving the primary as a result of the second Roche-lobe filling.

Nevertheless, if we restrict our analysis to a detailed interpretation of the visible and near-infrared spectral ranges, then the influence of the secondary component may be disregarded. The latter contributes about 0.01 of the flux in these spectral ranges, which shows up only in the far ultraviolet. The radiation from the interstellar medium in the binary system may also be ignored, because it increases the far-infrared luminosity of υ Sgr. The mass outflow through the Roche lobe gives rise to line emission: the feature in Hα is completely in emission, and the absorption feature in Hβ is significantly reduced by emission. For the same reason, several lines with P Cyg profiles are also observed in the red spectral range of υ Sgr. This distorts the spectral energy distri-

* E-mail address for contacts: leushin@sci.lebedev.ru

Table 1. Spectroscopic material for the analysis of υ Sgr

Date	Spectrogram number	Detector	Spectral range	Resolution	Signal/noise	Dispersion
May 17, 1978	1, 2	Kodak103aO	3900–5000	10 000	≅40	8 Å mm^{-1}
June 14, 1978	33–35	Kodak103aO	3900–5000	10 000	≅40	8 Å mm^{-1}
Aug. 13, 1986	21	Kodak103aO	3900–5000	10 000	≅40	1.8 Å mm^{-1}
June 15, 1996	c11 604s	CCD 1242 × 1192 Wight Instr. (GB)	3400–10 000	40 000	≅200	0.18 Å pic^{-1}
June 6, 1999	s23 712	CCD K585 530 × 580 Elektron	5050–6640	40 000	≅110	0.10 Å pic^{-1}

bution of the primary component only slightly, and it may be disregarded at the first stage.

A detailed study of υ Sgr based on high-dispersion spectra taken with the 6-m (BTA) telescope allows the binary's evolution to be reliably determined. At the same time, there are peculiarities in υ Sgr and in other such stars that primarily refer to anomalies of elements heavier than oxygen, whose analysis requires a higher accuracy than photographic observations can provide. CCD spectrographs can give such accuracies. These circumstances necessitate an analysis of υ Sgr using CCD spectra.

2. OBSERVATIONS

We have analyzed the atmosphere of the primary component of υ Sgr by using spectrograms taken during 1976–1986 with the main grating stellar spectrograph of the 6-m Special Astrophysical Observatory (SAO) telescope on Kodak 103aO and Kodak OaO photographic emulsions with a dispersion of 2–8 Å mm^{-1} in Hγ, as well as CCD spectra taken with an echelle spectrograph of the 1-m SAO telescope (Musaev 1993) and with the PFES echelle spectrometer of the 6-m telescope (Panchuk *et al.* 1998). The corresponding data on the spectroscopic material are given in Table 1.

The absorption lines that we identified and measured in the spectrum of the bright component of υ Sgr by using photographic spectra with measured equivalent widths in the wavelength range 3800–4680 Å are listed in Kravtsov and Leushin (1981). The results obtained from CCD spectra are presented in Table 2 for the measured Fe I, Fe II, and Fe III lines in the wavelength range 4000 to 8500 Å. We reduced the spectra with the Dech20 code (Galazutdinov 1992). Table 2 contains the atomic parameters, equivalent widths, and $\log(N(\mathrm{Fe})/\Sigma N_i)$ deduced from the corresponding lines. Since the spectrum for the primary component of υ Sgr is very rich in spectral lines, difficulties in drawing the continuum arise. Therefore, the accuracy of the equivalent widths cannot be higher than 10%, even at a signal-to-noise ratio of ≅200. We used $\log gf$ from the VALD compilation of $\log gf$ data (Ryabchikova *et al.* 1999) and from Leushin *et al.* 1997b) to analyze the spectral lines in υ Sgr.

3. MODEL ATMOSPHERES FOR THE PRIMARY COMPONENT OF υ Sgr

3.1. Model Parameters and Chemical Composition

Based on the parameters of the continuum (Burnashev 1981) and line (Kravtsov and Leushin 1981) spectra, we computed model atmospheres for the bright component of the unique binary υ Sgr (Leushin and Topil'skaya 1985). All spectral features of υ Sgr were described within the observational error limits by two models:

(1) $T_{\mathrm{eff}} = 13\,500 \pm 200$, $\log g = 1.5 \pm 0.5$, $N(\mathrm{He})/\Sigma N_i = 0.95$, $N(\mathrm{H})/\Sigma N_i = 10^{-6}$,

(2) $T_{\mathrm{eff}} = 14\,000 \pm 200$, $\log g = 2.0 \pm 0.5$, $N(\mathrm{He})/\Sigma N_i = 0.70$, $N(\mathrm{H})/\Sigma N_i = 10^{-6}$.

The microturbulent velocities for various species were determined by Kravtsov and Leushin (1981) from the curves of growth for the line equivalent widths derived from photographic spectra: V_t(V II) = 5.1 km s^{-1}, V_t(Cr II) = 6.6 km s^{-1}, V_t(Fe II) = 7.6 km s^{-1}, and V_t(S II) = 8.1 km s^{-1}. An analysis of these data leads us to conclude that the accuracy of photographic observations is not high enough for a proper model atmosphere to be uniquely chosen. In addition, the blanketing effect was ignored in the above papers, and, although important conclusions about the binary's evolution and its current state were drawn from an analysis of the chemical composition and physical parameters of its components (Leushin *et al.* 1998), recalculating a model atmosphere with allowance for new opacity data and for blanketing is of current interest. Using chemical-composition data (Leushin and Topil'skaya 1987), we computed a model with variations in abundances, effective temperature, and surface gravity. The model atmosphere was computed with the SAM1 code (Wright 1975), which we modified for the KONTUR code (Leushin and Topil'skaya 1986; Leushin 1995). We chose the following initial model parameters: T_{eff} = 13500, $\log g$ = 2.0; the abundances of some elements are given in Table 3 (the abundances of the remaining elements were taken to be solar).

Iterations began with the models of Kurucz (1989) for the corresponding effective temperature, surface gravity, and solar chemical composition. We passed to the chemical composition of υ Sgr by substituting the

Table 2. Parameters and equivalent widths of Fe I lines and iron abundances ([Fe] = log N(Fe)/ΣN$_i$)

λ, Å	ε_i, eV	loggf	W_λ, mÅ	[Fe]	λ, Å	ε_i, eV	loggf	W_λ, mÅ	[Fe]	λ, Å	ε_i, eV	loggf	W_λ, mÅ	[Fe]
4181.75	2.83	–.37	7.0	–3.69	4227.42	3.33	.26	26.0	–3.52	4299.23	2.41	–.43	9.0	–3.70
4184.89	2.83	–.56	2.0	–3.82	4233.60	2.48	–.35	11.0	–3.67	4307.90	1.56	–.07	50.0	–3.55
4187.79	2.42	–.30	8.0	–3.80	4250.12	2.47	–.37	11.0	–3.66	4325.76	1.61	.00	35.0	–3.75
4198.30	2.40	–.42	11.0	–3.64	4250.78	1.56	–.69	10.0	–3.74	4337.04	1.56	–1.40	1.0	–3.82
4199.09	3.05	.14	25.0	–3.54	4260.47	2.40	.03	32.0	–3.57	4383.54	1.49	.04	46.0	–3.70
4202.02	1.49	–.71	20.0	–3.47	4271.15	2.45	–.05	21.0	–3.67	4404.75	1.55	–.25	30.0	–3.67
4219.35	3.57	.12	10.0	–3.71	4271.76	1.49	–.16	22.0	–3.83	4415.12	1.61	–.62	11.0	–3.75

Parameters and equivalent widths of Fe II lines and iron abundances ([Fe] = log N(Fe)/ΣN$_i$)

λ, Å	ε_i, eV	loggf	W_λ, mÅ	[Fe]	λ, Å	ε_i, eV	loggf	W_λ, mÅ	[Fe]	λ, Å	ε_i, eV	loggf	W_λ, mÅ	[Fe]
4031.44	4.73	–3.27	81.0	–3.81	4122.67	2.58	–3.66	196.0	–3.54	4178.86	2.58	–2.50	320.0	–3.78
4061.78	5.95	–2.53	107.0	–3.81	4124.79	2.54	–4.00	96.0	–3.95	4180.98	4.74	–3.67	55.0	–3.72
4069.88	5.91	–3.08	100.0	–3.39	4128.74	2.58	–3.78	187.0	–3.49	4182.69	4.73	–3.70	30.0	–3.96
4070.03	2.54	–5.28	44.0	–3.26	4153.01	2.89	–5.39	10.0	–3.74	4202.52	6.81	–2.40	55.0	–4.10
4075.95	2.54	–4.94	50.0	–3.54	4171.37	7.71	–2.77	30.0	–3.71	4202.86	6.81	–2.73	55.0	–3.74
4085.73	7.49	–2.97	20.0	–3.78	4173.46	2.58	–2.59	330.0	–3.60	4211.80	2.64	–5.14	17.0	–3.80
4087.28	2.58	–4.93	41.0	–3.63	4175.10	7.94	–3.98	3.0	–3.51	4213.52	7.77	–2.55	25.0	–3.88
4088.76	2.84	–4.89	49.0	–3.48	4175.99	6.81	–3.84	9.0	–3.66	4221.40	6.14	–3.13	44.0	–3.77
4093.23	6.70	–3.03	46.0	–3.64	4176.45	4.74	–4.59	9.0	–3.76	4229.37	7.81	–2.87	46.0	–3.38
4097.50	7.65	–2.27	93.0	–3.48	4177.69	2.54	–3.85	201.0	–3.34	4233.17	2.58	–1.90	379.0	–3.93
4104.18	2.86	–5.42	10.0	–3.72	4178.44	5.96	–3.54	40.0	–3.58					
4111.87	5.96	–2.41	125.0	–3.79	4178.63	7.49	–4.29	1.0	–3.74					
6605.31	11.11	–1.45	17.0	–3.82	6665.59	11.17	–1.64	40.0	–3.28	6722.76	11.14	–.76	148.0	–3.28
6606.34	11.02	–2.78	1.2	–3.62	6668.51	11.05	–1.40	55.0	–3.42	6724.82	10.93	–.92	44.0	–3.90
6607.05	11.11	–1.76	2.0	–4.39	6672.83	11.09	–.65	50.0	–4.14	6728.44	11.08	–.53	90.0	–3.84
6612.04	7.28	–3.56	20.0	–3.39	6677.30	7.27	–1.89	165.0	–3.73	6730.12	11.24	–1.85	12.0	–3.60
6618.41	9.76	–1.32	35.0	–4.27	6679.75	10.91	–.47	67.0	–4.27	6732.09	11.25	–1.84	5.0	–3.79
6621.98	11.02	–.05	230.0	–3.55	6681.41	11.11	–1.22	10.0	–4.38	6735.62	9.07	–2.69	5.0	–3.85
6627.26	7.27	–1.91	165.0	–3.71	6684.18	10.91	–.65	90.0	–3.81	6741.40	11.22	–1.68	48.0	–3.03
6628.66	11.24	–1.90	9.0	–3.65	6685.47	10.93	–.72	80.0	–3.80	6743.68	11.21	–.82	62.0	–3.76
6632.59	11.24	–2.16	7.0	–3.54	6686.74	11.24	–2.57	4.0	–3.28	6744.85	11.05	–.86	34.0	–4.14
6632.64	7.71	–4.13	2.2	–3.52	6686.87	11.44	–1.29	5.0	–4.46	6747.98	9.90	–3.10	2.5	–3.57
6636.94	11.21	–1.93	25.0	–3.14	6689.08	11.35	–2.00	4.0	–3.76	6748.84	11.27	-.83	47.0	–3.84
6641.99	9.58	–2.51	13.0	–3.62	6689.66	11.15	–2.09	5.0	–3.71	6754.36	11.17	–.64	38.0	–4.31
6643.07	10.91	–.77	60.0	–3.89	6691.16	7.12	–3.97	6.5	–3.55	6755.08	9.90	–3.13	4.0	–3.30
6647.69	10.91	–.60	74.0	–3.99	6704.89	9.74	–3.15	5.0	–3.26	6767.57	9.85	–1.83	16.0	–3.91
6650.97	7.13	–2.59	50.0	–3.85	6708.88	10.91	–.52	150.0	–3.58	6770.90	11.20	–.18	168.0	–3.68
6658.58	7.99	–3.92	3.0	–3.52	6719.64	10.93	–.52	75.0	–4.09	6784.22	6.80	–3.17	53.0	–3.53
6662.83	11.11	–1.20	9.0	–4.45	6721.39	11.16	–1.90	20.0	–3.37					

Parameters and equivalent widths of Fe III lines and iron abundances ([Fe] = log N(Fe)/ΣN$_i$)

λ, Å	ε_i, eV	loggf	W_λ, mÅ	[Fe]	λ, Å	ε_i, eV	loggf	W_λ, mÅ	[Fe]	λ, Å	ε_i, eV	loggf	W_λ, mÅ	[Fe]
4053.11	20.61	.26	4.5	–4.21	4348.80	13.13	–2.10	20.0	–3.89	4395.76	8.26	–2.90	125.0	–4.02
4052.51	24.63	.21	1.0	–3.14	4352.58	8.25	–3.17	108.0	–3.85	4404.16	13.13	–2.38	13.0	–3.86
4059.44	11.22	–4.44	1.0	–3.75	4365.64	8.26	–3.40	59.0	–4.14	4419.59	8.24	–2.22	220.0	–3.92
4071.70	24.64	.37	1.0	–3.55	4371.34	8.24	–2.99	140.0	–3.80	4430.95	8.25	–2.56	270.0	–3.15
4323.78	11.22	–3.48	20.0	–3.50	4382.51	8.26	–3.02	110.0	–4.03					
5086.70	8.66	–2.89	168.0	–3.76	5219.13	22.22	–.08	.1	–4.04	5284.83	22.31	.47	2.0	–3.78
5105.33	22.27	–.06	1.0	–3.64	5235.22	22.28	–.40	.1	–3.79	5295.03	22.30	–.53	.1	–3.70
5127.38	8.66	–2.52	250.0	–3.70	5235.66	18.27	–.11	36.0	–3.64	5298.11	22.31	.37	.5	–3.88
5127.63	8.66	–2.86	155.0	–3.86	5243.30	18.27	.40	97.0	–3.49	5299.93	18.26	–.17	18.0	–3.83
5156.11	8.64	–2.02	364.0	–3.59	5276.40	18.26	.00	14.0	–4.18	5306.70	18.26	–.34	34.0	–3.47
5193.91	8.66	–2.85	136.0	–4.00	5282.30	18.27	.09	59.0	–3.55					
5194.16	8.66	–3.93	41.0	–3.72	5282.60	13.13	–3.65	2.0	–3.38					

Table 3. The abundances of elements in the model atmosphere of υ Sgr

Element	H	He	C	N	O	Ne	Mg	Al	Si	Ca	Fe
$\log N_k/\Sigma N_i$	−3.30	−0.01	−2.32	−1.89	−2.76	−2.76	−3.67	−4.75	−3.60	−4.82	−3.90

Table 4. Total absorption in a 25 Å band (W) and emission blocking coefficients (a_λ)

λ, Å	W, Å	a_λ	λ, Å	W, Å	a_λ	λ, Å	W, Å	a_λ	λ, Å	W, Å	a_λ
3500	3.20	1.14	4205	1.80	1.07	5680	1.93	1.08	6685	0.67	1.02
3525	2.80	1.12	4290	2.19	1.09	5705	1.07	1.04	6760	1.54	1.06
3665	2.84	1.12	4315	1.80	1.07	5800	1.76	1.08	6785	0.90	1.04
3690	2.96	1.13	4410	2.06	1.09	5825	1.73	1.08	6810	0.85	1.04
3725	3.49	1.16	4435	2.48	1.11	5950	2.98	1.13	7480	1.02	1.04
3750	4.57	1.22	4580	2.59	1.11	5975	1.92	1.08	7505	0.93	1.04
3780	3.32	1.15	4605	1.86	1.07	6180	0.78	1.03	7530	0.88	1.04
3805	3.30	1.15	4810	2.14	1.09	6205	0.71	1.03	7720	0.62	1.02
3840	3.41	1.16	4835	1.78	1.08	6230	2.26	1.10	7745	0.64	1.02
3865	2.76	1.12	5070	2.78	1.13	6350	1.91	1.08	8115	0.79	1.03
3940	2.42	1.11	5095	2.89	1.13	6375	2.12	1.09	8140	0.54	1.02
3965	3.37	1.15	5290	2.62	1.11	6400	2.45	1.11	8165	1.92	1.08
4070	2.96	1.13	5315	3.01	1.14	6610	0.84	1.04	8200	0.86	1.04
4095	2.48	1.11	5480	3.06	1.14	6635	0.97	1.04			
4180	2.93	1.13	5505	2.17	1.09	6660	2.00	1.09	15000		1.00

mean absorption coefficient calculated as a Rosseland mean (Mihalas 1982) and by subsequent iterations for the nongray absorption coefficient determined by the specified chemical composition.

3.2. Allowance for Blanketing

The blanketing effect in the model atmosphere of υ Sgr is difficult to take into account, because an accurate theoretical allowance for line absorption cannot be made due to the absence of a full list of lines in the spectrum of υ Sgr. Many lines have not yet been identified. In addition, OPDF calculations require reliable data on the abundances of elements with many spectral lines in the atmospheric temperature range. At the same time, the question regarding the abundances of some elements in υ Sgr requires detailed analyses based on high-resolution spectroscopic data (Leushin and Topil'skaya 1988). On the other hand, blanketing can be taken into account by directly measuring the spectrum for the primary component of υ Sgr. Table 4 gives the total absorption (W) measured in $\Delta\lambda = 25$ Å bands from echelle spectra for the wavelength range 3500 to 8200 Å. Also given here are the emission blocking coefficients

$$\mathbf{a}_\lambda = k_\lambda/k_\lambda^{\rm con} = (k_\lambda^{\rm lin} + k_\lambda^{\rm con})/k_\lambda^{\rm con} \cong H_\lambda^{\rm con}/H_\lambda,$$

$$\mathbf{a}_\lambda = 25/(25 - W),$$

where k_λ is the continuum absorption coefficient with line absorption, $k_\lambda^{\rm con}$ is the continuum absorption coefficient without line absorption, $k_\lambda^{\rm lin}$ is the line absorption coefficient averaged over a 25-Å band, $H_\lambda^{\rm con}$ is the emergent continuum flux integrated over a 25-Å band, and H_λ is the same flux with absorption lines.

In the spectral range under consideration, the blocking coefficients can be calculated from the total line absorption, because the continuum location between line blends for large wavelength regions is determined with a satisfactory accuracy. Models are computed for a grid of wavelengths with the largest value of 14 588 Å. There are no measured W and, consequently, $\mathbf{a}_\lambda$ in the range 8000 to 15 000 Å; nevertheless, by extrapolating the wavelength dependence of $\mathbf{a}_\lambda$, we may assume the blocking coefficient in this range to be close to 1.0.

In the ultraviolet (at $\lambda < 3000$ Å), the blending is so strong that the continuum location cannot be determined unambiguously. Therefore, to calculate the blocking coefficient in this range, we compared the observed energy distribution (Jamar *et al.* 1976; Trams *et al.* 1991) with a theoretical one for the model with $T = 13\,500$ K, $\log g = 2.0$, and $N(\mathrm{H})/\Sigma N_i = 5 \times 10^{-4}$.

Table 5 gives blocking coefficients in the wavelength range 1400–1500 Å for a grid of wavelengths of the model atmosphere. The coefficients from Tables 4 and 5 were entered into the code for model computations as factors of the continuum absorption coefficients to allow for additional line absorption; we took an interpolated value for the grid of model wavelengths at $\lambda > 3000$ Å and an extrapolated value for 500 and 1000 Å. Since blanketing affects the atmospheric structure through the integral condition of radiative equilib-

Table 5. Far-ultraviolet emission blocking coefficients for the spectrum of υ Sgr

λ, Å	a_λ	λ, Å	a_λ
500	3.10	1817	1.86
1000	2.60	1874	2.18
1443	1.36	1934	1.80
1444	2.11	1978	1.48
1484	1.84	2077	1.48
1520	2.11	2078	1.49
1521	2.14	2141	1.25
1578	2.46	2221	1.10
1622	2.17	2306	1.04
1647	2.09	2398	1.13
1677	2.05	2514	1.30
1713	2.02		

Table 6. Energy fluxes from υ Sgr at the boundary of the Earth's atmosphere (columns 2 and 3) and per unit surface area of the stellar atmosphere (columns 4 and 5)

λ, Å	$\log H_\lambda$, erg cm^{-2} s^{-1} nm^{-1}			
	Burnashev (1981)	Trams *et al.* (1991)	per unit stellar surface area	model calculation
2500		−9.41	8.52	8.61
3600	−9.00	−9.03	8.54	8.44
4400	−9.08	−9.02	8.47	8.29
5500	−9.30	−9.24	8.19	8.00

rium, the line opacity can be introduced by using an average absorption within the wavelength range chosen (Sakhibullin 1997). When computing our models, we assumed the blocking coefficients to be depth-independent and to satisfy the following boundary conditions:

$$\mathbf{a}_\lambda = \begin{cases} H_\lambda^{\rm con}/H_\lambda & \text{for} \quad \tau_\lambda \le 1 \\ 0 & \text{for} \quad \tau_\lambda > 1. \end{cases}$$

The assumption that $\mathbf{a}_\lambda$ is constant with depth does not introduce large errors in the model atmosphere (Sakhibullin 1997; Gustafsson 1981).

3.3. Spectral Energy Distribution for υ Sgr

To test the adequacy of our computed model, we compared the theoretically computed and observed spectral energy distributions for υ Sgr. The energy fluxes from υ Sgr ($\log H_\lambda$) for several wavelengths are given in Table 6.

Burnashev (1981) found the flux from υ Sgr at the boundary of the Earth's atmosphere for 5500 Å to be $H_\lambda = 10^{-2.3}$ erg cm^{-2} s^{-1} cm^{-1} or $10^{-9.3}$ erg cm^{-2} s^{-1} nm^{-1}. Given the inverse square law for $R_{\rm star} = (40–50)R_\odot$ (Dadley and Jeffery 1993; Leushin *et al.* 1997a) and the binary's distance of 500 pc (Rao and Venugopal 1985), the flux per unit stellar surface area is $H_{5500} = 10^{8.0}$ erg cm^{-2} s^{-1} nm^{-1}, which closely agrees with the model calculations. However, the interstellar extinction and interstellar reddening should be considered here. At a distance of 0.5 kpc, $A(V) = -0\overset{m}{.}48$ (Straizys 1977), which gives $\Delta\log H_{5500} = 0.19$ (the flux per unit stellar surface area corrected for interstellar extinction is $\log H_{5500} = 8.19$), while the flux at λ = 4400 Å is $\log H_{4400} = 8.41$. Applying a correction for the interstellar reddening using $E_{B-V} = A(V)/R$, where $R = 3.2 \pm 0.2$ (Walker 1990), yields $E_{B-V} = -0\overset{m}{.}48/3 = -0.16^m$ and $\Delta\log H_{4400} = 0.06$. In this case, the observed slope of the Balmer continuum (*B*–*V*) is equal to that computed for the model. A similar calculation for H_{3600} ($E_{U-B} = 0.8\,E_{B-V} = -0\overset{m}{.}13$, $\Delta\log H_{3600} = 0.05$) yields $\log H_{3600} = 8.54$. The interstellar extinction law for the far ultraviolet (Straizys 1977) leads to the flux $\log H_{2500} = 8.52$ ($E_{\lambda-V} = 6.8\,E_{B-V} = -1\overset{m}{.}1$, $\Delta\log H_{2500} = 0.44$).

A comparison of the observed and theoretical energy distributions shows that the distribution curves generally coincide, although the observed curve exhibits a far-ultraviolet deficit and visible and near-infrared excesses. The discrepancy can be explained by the presence of a thick envelope in the binary. This envelope is responsible for the absorption of far-ultraviolet radiation and its visible and infrared reemission. Allowing for this factor leads to an increase in flux at 1000–2500 Å ($\Delta\log H_\lambda \approx +0.1$) and to a decrease in flux at 3600–5500 Å ($\Delta\log H_\lambda \approx -0.2$). In Fig. 1, the observed energy distribution corrected in this way is compared with the theoretically computed one. The agreement between the data is satisfactory. Consequently, the model atmosphere may be assumed to faithfully represent the primary component of υ Sgr.

Other methods of reconciling the theoretical and observed energy distributions seem less accurate. A reduction in the model effective temperature results in a lower flux in all spectral bands, which increases the disagreement between theory and observations in the ultraviolet further still. An increase in blanketing (an increase in blanketing coefficients) at 1500–2600 Å requires that the radiation be redistributed only in the stellar atmosphere itself and that the envelope remain transparent, which is in conflict with observations (Dadley and Jeffery 1993; Rao and Venugopal 1985).

3.4. Hydrogen Lines

For the atmospheres of normal stars, the most accurate and sensitive indicator of the validity of the computed model parameters ($T_{\rm eff}$ and $\log g$) is a comparison of the theoretical and observed hydrogen-line profiles

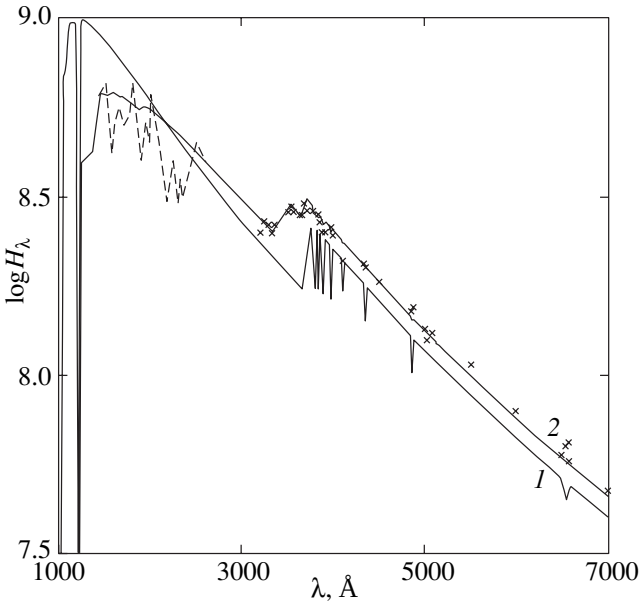

Fig. 1. Comparison of the observed spectral energy distribution for the primary component of υ Sgr (asterisks—Burnashev 1981; dashes—Jamar 1976) with those computed for the model with $T_{\rm eff}$ = 13 500 K and log$g$ = 2.0. Curves *1* and *2* correspond to solar chemical composition and to the composition from Table 3, respectively.

and equivalent widths. For υ Sgr, such a comparison is ambiguous, because, on the one hand, its hydrogen abundance is not known and, on the other, the envelope affects the line profiles and equivalent widths by distorting them.

In Fig. 2, the observed hydrogen-line profiles in the spectrum of υ Sgr are compared with those theoretically computed for the model with $T_{\rm eff}$ = 13 500 K, log$g$ = 2.0, and N(H)/ΣN_i = 0.0005. The coincidence is close for the Hγ and Hδ profiles. For Hβ, the theoretical profile gives a more intense line than observed. The discrepancy is probably attributable to the influence of the envelope emission, which reduces the intensity of the Hβ absorption line and completely floods the Hα line with emission. In the spectrum of υ Sgr, Hα is observed only in emission. For Hγ and Hδ, the emission is so weak that its effect is undetectable.

Table 7 gives the equivalent widths (W_λ) and central depths (R_c) for Hβ, Hγ, and Hδ in the spectrum of υ Sgr. Also given here are the theoretically calculated values of these parameters for models with different $T_{\rm eff}$, log$g$, and N(H)/ΣN_i.

A comparison of the Hγ and Hδ profiles and equivalent widths in the spectrum of υ Sgr with the theoreti-

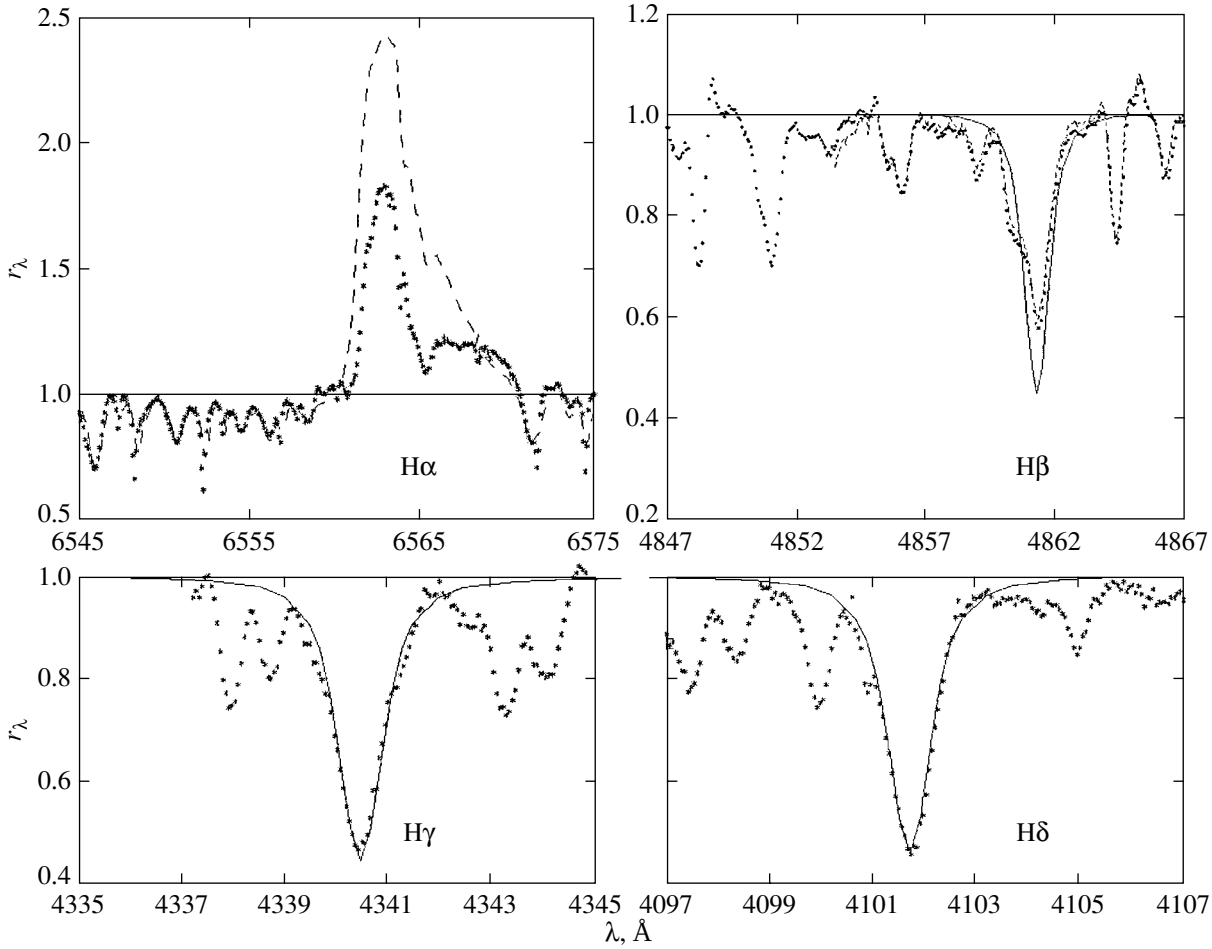

Fig. 2. Comparison of hydrogen line profiles. The asterisks and dashes represent the observations, and the solid lines represent the theory for the model with $T_{\rm eff}$ = 13 500 K, log$g$ = 2.0, and N(H)/ΣN_i = 5×10^{-4}.

Table 7. Hydrogen lines in the spectrum of υ Sgr

Model $T_{\rm eff}$, $N(\rm H)/\Sigma N_i$		W_λ, mÅ			R_c		
		Hβ	Hγ	Hδ	Hβ	Hγ	Hδ
υ Sgr		614.0	703.6	615.1	0.41	0.53	0.51
13500	0.0001	420.0	326.0	236.0	0.46	0.42	0.32
$\log g$ = 2.0	0.0005	672.0	600.0	537.0	0.53	0.52	0.50
	0.0010	896.0	835.0	797.0	0.57	0.57	0.56
13500	0.0001	302.0	212.0	141.0	0.34	0.23	0.16
$\log g$ = 1.5	0.0005	486.0	416.0	351.0	0.49	0.49	0.46
	0.0010	645.0	581.0	537.0	0.54	0.54	0.53
13000	0.0001	420.0	326.0	236.0	0.46	0.42	0.32
$\log g$ = 2.0	0.0005	672.0	600.0	537.0	0.53	0.52	0.50
	0.0010	896.0	835.0	797.0	0.57	0.57	0.56

cally calculated ones indicates that the model atmosphere with $T_{\rm eff}$ = 13500 K, $\log g$ = 2.0, and $N(\rm H)/\Sigma N_i$ = 0.0005 chosen from the spectral energy distribution faithfully describes the hydrogen lines in the primary component of υ Sgr.

4. ATMOSPHERIC IRON ABUNDANCE IN THE PRIMARY COMPONENT OF υ Sgr

To determine the atmospheric iron abundance in the primary component of υ Sgr, we measured the equivalent widths of blue and red Fe I, Fe II, and Fe III lines. Our measurements are given Table 2. This table lists wavelengths (λ, Å), lower-level excitation potentials (ε_i, eV), oscillator strengths ($\log gf$), line equivalent widths (W_λ, mA) measured from our spectra, and iron abundances [$\log(N(\rm Fe)/\Sigma N_i)$] for each line. The abundances given in the tables were obtained for two microturbulent velocities: V_t = 8 km s^{-1} and 12 km s^{-1} for lines in the wavelength ranges 4000–4400 and 5500–6800 Å, respectively. One of the most important features of the υ Sgr spectrum is that iron lines in three ionization stages (Fe I, Fe II, and Fe III) are reliably identified in its spectrum. The multiplicity of iron lines in the spectrum not only allows the iron abundances to be determined for the three stages but also makes it possible to study in detail the behavior of the microturbulent velocity in the stellar atmosphere. Table 8 gives the coefficients of the dependencies of relative iron abundance on line equivalent width for various microturbulent velocities

$$\log(N(\rm Fe)/\Sigma N_i) = \log(N(\rm Fe)/\Sigma N_i)_0 + kW_\lambda.$$

The dependencies were constructed for groups of lines in the three ionization stages and in different spectral ranges.

Two of the dependencies under consideration (V_t = 8 and 12 km s^{-1}) for Fe II lines in the wavelength range 6600–6800 Å are shown in Fig. 3.

An examination of the data in Table 8 and in Fig. 3 strongly suggests that the atmospheric microturbulent velocity in the primary component of υ Sgr undoubtedly changes with depth and depends on the place where the group of lines used to determine this velocity is formed. The microturbulent velocity derived from blue (4000–4400 Å) lines for Fe II and Fe III is V_t = 8 km s^{-1}. For the same ions in the red, V_t = 12 km s^{-1}. Fe I lines were found and measured only in the blue. Their intensities in the spectrum of υ Sgr are low and virtually

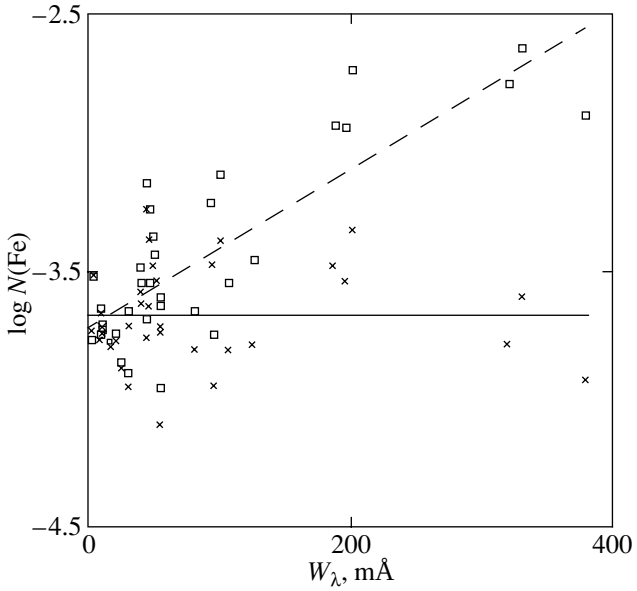

Fig. 3. Elemental abundance versus W_λ for Fe II lines at V_t = 8 km s^{-1} (asterisks) and V_t = 12 km s^{-1} (squares).

independent of the microturbulent velocity. Therefore, it is inappropriate to use the dependence

$$\log(N(\mathrm{Fe})/\Sigma N_i) = \log(N(\mathrm{Fe})/\Sigma N_i)_0 + kW_\lambda,$$

and the coefficients in Table 8 to choose V_t. Variations in V_t between 8 and 15 km s^{-1} for these lines change the mean $\log(N(\mathrm{Fe})/\Sigma N_i)$ only slightly.

The inferred difference in the microturbulent velocities determined from iron lines in different spectral ranges cannot be explained by measurement errors. Consequently, this difference is attributable to actual peculiarities of the atmospheric structure in the primary component of υ Sgr. Figure 4 shows the plots of effective Fe II line formation depth against equivalent width computed for our model atmosphere at λ = 4000 and 6500 Å. The effective line formation depth (τ_W) is given by

$$\tau_W = \int_0^\infty (1-r_\lambda)\tau_\lambda d\lambda / \int_0^\infty (1-r_\lambda)d\lambda,$$

where

$$\tau_\lambda = \int_0^\infty S_\lambda(t)E_2(t)tdt / \int_0^\infty S_\lambda(t)E_2(t)dt$$

gives the formation depth of the line flux.

We see from Fig. 4 that the red lines are formed much higher than the blue lines. On a linear scale, the difference in the formation heights for a line with W_λ = 70 mÅ ($\Delta\tau$ = 0.95) is 1.3×10^6 km; the entire atmosphere is about 4×10^6 km thick. Such a behavior of the microturbulent velocity is also noted for other supergiants (Lyubimkov and Samedov 1990) and suggests atmospheric instability, which is related to the Roche-lobe filling for υ Sgr.

Table 9 gives the mean atmospheric iron abundances for υ Sgr derived from Fe I, Fe II, and Fe III lines with standard deviations from the mean. All values coincide within the error limits. Thus, the mean iron abundance determined from the equivalent widths of 138 lines in three ionization stages is $\log(N(\mathrm{Fe})/\Sigma N_i) = -3.71 \pm 0.20$.

An analysis of the accuracy of determining the abundance of an element from the line equivalent width is primarily associated with the accuracy of drawing the line profile and measuring the line intensity. For strongly blended spectra, the task of identifying a line of the element under study is nontrivial and, occasionally, not accomplishable. An abundance analysis using line profiles with computations of synthetic-spectrum portions is largely free from the above factors. Here, blending is taken into account by including all the lines in a given spectral range in the synthetic profile. At the same time, the computational procedure requires that the parameters of all lines in the blend be known, which is not always possible, particularly for weak lines. In addition, the profiles of strong lines are affected by dynamical atmospheric parameters (envelope expansion and outflow, differential atmospheric rotation, meridional flows, height variations in microturbulent

Table 8. Coefficients of the dependencies of relative iron abundance on line equivalent width for various microturbulent velocities and the corresponding mean [$\log(N(\mathrm{Fe})/\Sigma N_i)$] and rms errors of these means [$\Delta(\log N)$]

V_t, km s^{-1}	k	$\log(N(\mathrm{Fe})/\Sigma N_i)_0$	$\log(N(\mathrm{Fe})/\Sigma N_i)$	±Δ(log N)
Fe I 4180–4415 Å				
15.0	+0.00101	−3.708	−3.689	0.020
10.0	+0.00256	−3.738	−3.688	0.021
8.0	+0.00348	−3.746	−3.681	0.022
5.0	+0.00624	−3.769	−3.651	0.028
Fe II 4030–4235 Å				
15.0	−0.00266	−3.615	−3.842	0.057
8.5	−0.00038	−3.672	−3.700	0.042
8.0	+0.00003	−3.680	−3.677	0.033
7.7	+0.00028	−3.685	−3.661	0.049
7.5	+0.00040	−3.688	−3.650	0.058
5.0	+0.00308	−3.718	−3.455	0.062
Fe II 6600–6800 Å				
15.0	−0.00050	−3.718	−3.744	0.050
13.0	−0.00035	−3.710	−3.722	0.042
12.5	−0.00003	−3.708	−3.714	0.033
12.0	−0.000001	−3.702	−3.702	0.030
8.0	+0.00186	−3.748	−3.661	0.061
Fe III 4050–4430 Å				
15.0	−0.00308	−3.639	−3.881	0.138
10.0	−0.00109	−3.740	−3.824	0.102
8.0	+0.00043	−3.806	−3.773	0.088
5.0	+0.00419	−3.876	−3.548	0.129
Fe III 5080–5310 Å				
15.0	−0.00070	−3.704	−3.755	0.052
12.0	+0.00024	−3.754	−3.738	0.046
8.0	+0.00246	−3.826	−3.646	0.078
5.0	+0.00568	−3.882	−3.470	0.145

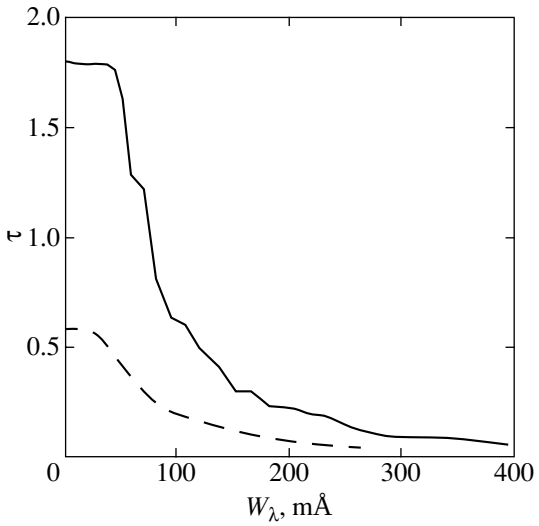

Fig. 4. Effective line formation depth versus equivalent width for the blue (solid line) and red (dashed line) spectral ranges.

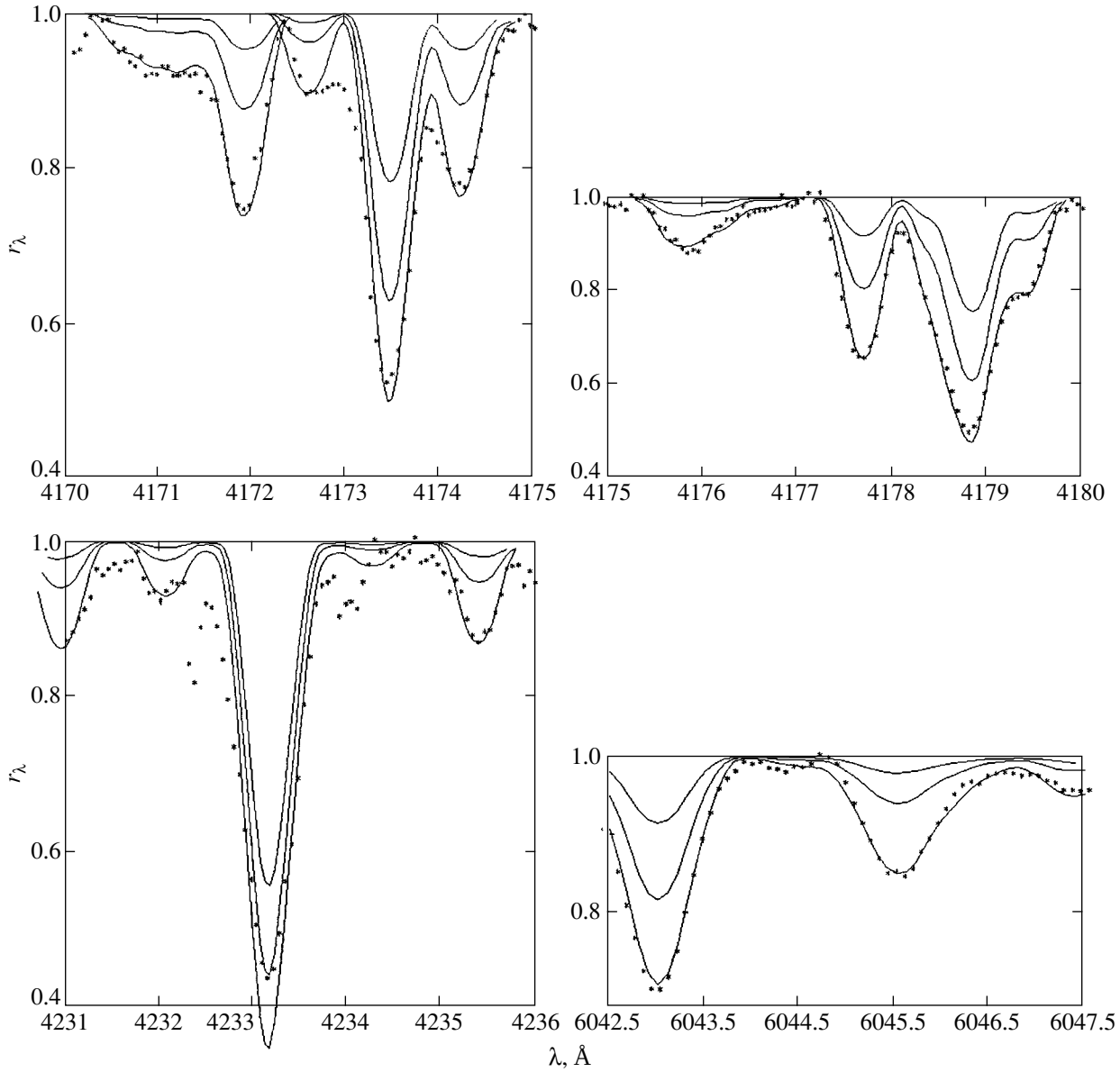

Fig. 5. The observed spectrum of υ Sgr (asterisks) and its computed spectrum for the elemental abundances in Table 10 and for those than are lower by –0.5 and –1.0 dex (solid lines).

velocity, etc.). Nevertheless, the abundances are determined from line profiles more reliably than they are from the total line intensity. In any case, comparing the observed and theoretical profiles is an additional source of increasing the accuracy of determining the elemental abundance.

Table 9. Atmospheric iron abundances for υ Sgr

Species	Spectral range	$\log(N(\mathrm{Fe})/\Sigma N_i)$	$\Delta\log N$
Fe I	Blue	–3.68	±0.10
Fe II	Blue	–3.68	±0.19
	Red	–3.70	±0.21
Fe III	Blue	–3.77	±0.30
	Red	–3.74	±0.18

In Fig. 5, the theoretically calculated portions of synthetic spectra are compared with the observed ones for the model atmosphere with T_{eff} = 13 500 K, $\log g$ = 2.0, and the elemental abundances from Table 3. As was noted previously, varying the elemental abundances within 0.5 dex of the data in Table 3 changes the atmospheric structure only slightly; therefore, when computing line profiles, we varied the abundances of each element whose lines were within the computed wavelength range. Table 10 gives parameters of the lines chosen for our calculations and the abundances of the corresponding element at which the coincidence of the theoretical and observed spectra was closest. Figure 5 also shows the curves computed with abundances that are lower by –0.5 and –1.0 dex.

Table 10. Line parameters for synthetic-spectrum computations

λ, Å	Species	log*gf*	ε_i, eV	$\log(N_r/\Sigma N_i)$	λ, Å	Species	log*gf*	ε_i, eV	$\log(N_r/\Sigma N_i)$	λ, Å	Species	log*gf*	ε_i, eV	$\log(N_r/\Sigma N_i)$
4170.30	Fe II	−3.66	9.37	−3.90	4173.07	Ti II	1.32	2.60	−6.35	4233.17	Fe II	−1.90	2.58	−4.20
4170.46	C I	−3.40	7.95	−2.32	4174.14	S II	0.76	17.40	−4.64	4233.24	Cr II	−1.94	3.86	−4.98
4170.61	Cr II	−3.04	3.10	−5.68	4174.53	Fe II	−5.29	2.58	−3.90	4233.60	Fe I	−0.60	2.48	−3.90
4170.65	C I	−4.14	7.95	−2.32						4233.85	Ti I	−2.65	3.13	−5.65
4170.84	Cr II	−3.57	5.66	−4.68	4175.40	Fe II	−2.31	11.15	−3.90	4234.26	V II	−1.73	1.67	−6.93
4171.03	Mn II	−2.36	6.13	−4.87	4175.67	N II	−1.18	23.20	−1.89	4235.33	Fe II	−1.74	11.11	−3.90
4171.37	Fe II	−2.67	7.71	−3.90	4175.75	Fe II	−2.80	6.81	−3.60	4235.39	Fe II	−0.76	11.15	−3.70
4171.60	N II	0.28	23.20	−2.99	4176.16	N II	0.60	23.20	−2.98					
4171.89	Fe I	−1.70	3.30	−3.90	4176.68	Ti II	−1.90	4.86	−5.35	6043.05	P II	0.38	10.80	−5.24
4171.90	Cr II	−2.38	3.10	−5.68	4177.69	Fe II	−3.75	2.54	−3.68	6044.54	Fe II	−5.24	3.15	−3.90
4171.91	Ti II	−0.27	2.60	−6.65	4178.44	Fe II	−3.54	5.96	−3.90	6044.78	C I	−2.07	9.00	−3.32
					4178.46	P II	−0.41	9.63	−6.24	6045.46	Fe II	−2.61	6.21	−3.80
4172.57	Fe I	−2.80	3.30	−3.90	4178.86	Fe II	−2.50	2.58	−4.20	6045.82	Fe II	−0.97	10.71	−3.70
4172.59	Cr II	−2.36	3.10	−5.85	4189.42	Cr II	−1.80	3.83	−5.68	6046.03	S I	−1.03	7.87	−4.94
4173.28	Fe II	−3.46	7.58	−3.90						6046.13	N I	−2.32	18.61	−2.76
4173.46	Fe II	−2.74	2.58	−4.20	4230.94	S II	0.56	17.45	−4.92	6046.44	O I	−1.37	10.99	−3.76
4173.54	Ti II	−1.82	1.08	−5.65	4232.04	V II	−0.59	3.97	−6.63	6047.22	C I	−2.88	9.00	−3.32
4174.00	S II	−1.24	17.39	−4.64	4232.56	Ce II	−0.74	0.72	−8.40	6047.43	Fe II	−1.93	8.84	−3.80

Thus, our synthetic-spectrum computations show that the iron abundance determined from line profiles is within the same error limits as that for line equivalent widths. Nevertheless, the mean value for line profiles is approximately 0.2 dex lower than that inferred from equivalent widths: $\log(N(\mathrm{Fe})/\Sigma N_i) = -3.90 \pm 0.20$.

5. CONCLUSION

Our analysis of the continuum and line spectra for the binary υ Sgr shows that the atmosphere of its primary component, within the observational error limits, is completely represented by the model with T_{eff} = 13 500 K, $\log g = 2.0 \pm 0.5$, and the following mass fractions of light elements: 10^{-4} for H, 0.91 for He, 0.013 for C, 0.049 for N, and 0.008 for O. In the stellar atmosphere, the microturbulent velocity varies within no less than 8–12 km s^{-1}.

The iron abundance in the atmosphere and, probably, in the entire star is $\log(N(\mathrm{Fe})/\Sigma N_i) = -3.80 \pm 0.20$, as determined from lines of iron ions in three ionization stages and virtually over the entire wavelength range.

The derived atmospheric elemental abundances in the primary component of υ Sgr reflect the evolutionary changes in chemical composition in the binary through the nuclear transformations of hydrogen into helium. Whereas the binary's initial chemical composition was nearly solar ($\log(N(\mathrm{H})/\Sigma N_i) = -0.04$, $\log(N(\mathrm{He})/\Sigma N_i) = -1.04$, $\log(N(\mathrm{Fe})/\Sigma N_i) = -4.50$), the total number of atoms after the complete conversion of hydrogen into helium decreased by a factor of 3.5, which also caused $\log(N_k/\Sigma N_i)$ to change by +0.6 dex for the elements that are not involved in nuclear reactions. For iron, this gives $\log(N(\mathrm{Fe})/\Sigma N_i) = -3.90$.

Thus, our derived iron abundance matches its initial value at the binary's formation time. The small enhancement (+0.1 dex) compared to the solar abundance is probably attributable to a general increase in Galactic heavy-element abundance.

ACKNOWLEDGMENTS

I am grateful to V.G. Klochkova, F.A. Musaev, and V.E. Panchuk, who took the spectra of υ Sgr. This study was supported by the Russian Foundation for Basic Research (project no. 00-02-16213a).

REFERENCES

1. V. I. Burnashev, Izv. Krym. Astrofiz. Obs. **53**, 104 (1981).
2. R. E. Dadley and C. S. Jeffery, Mon. Not. R. Astron. Soc. **262**, 945 (1993).
3. G. A. Galazutdinov, Preprint SAO (1992), issue 92.
4. B. Gustafsson, in *Physical Process in Red Giants*, Ed. by I. Iben and A. Renzini (Kluwer, Dordrecht, 1981), p. 25.
5. C. Jamar, D. Macau-Hercot, A. Monfils, *et al.*, *Ultraviolet Bright Star Spectrophotometric Catalogue* (European Space Agency, Paris, 1976).
6. V. V. Kravtsov and V. V. Leushin, *A Spectrophotometric Analysis of the Atmosphere of the Bright Component of the Binary υ Sgr*, Available from VINITI, No. 99-82 (1981).

7. R. L. Kurucz, *Magnetic Tape* (1989).
8. V. V. Leushin, Astron. Zh. **72**, 543 (1995) [Astron. Rep. **39**, 498 (1995)].
9. V. V. Leushin and G. P. Topil'skaya, Astrofizika **22**, 121 (1985).
10. V. V. Leushin and G. P. Topil'skaya, Astrofizika **25**, 103 (1986).
11. V. V. Leushin and G. P. Topil'skaya, Astrofizika **26**, 195 (1987).
12. V. V. Leushin and G. P. Topil'skaya, Astrofizika **28**, 554 (1988).
13. V. V. Leushin, L. I. Snezhko, and V. V. Chuvenkov, Bull. Spec. Astrophys. Obs. **43**, 55 (1997a).
14. V. V. Leushin, G. P. Topilskaya, and F. A. Musaev, in *Stellar Magnetic Field: Proceedings of the International Conference*, Ed. by Yu. V. Glagolevskij and I. I. Romanyuk (Spec. Astrophys. Obs., Russ. Acad. Sci., Moscow, 1997b), p. 143.
15. V. V. Leushin, L. I. Snezhko, and V. V. Chuvenkov, Pis'ma Astron. Zh. **24**, 45 (1998) [Astron. Lett. **24**, 39 (1998)].
16. L. S. Lyubimkov and Z. A. Samedov, Astrofizika **32**, 49 (1990).
17. D. Mihalas, *Stellar Atmospheres* (Freeman, San Francisco, 1978; Mir, Moscow, 1982).
18. F. A. Musaev, Pis'ma Astron. Zh. **19**, 776 (1993) [Astron. Lett. **19**, 315 (1993)].
19. V. E. Panchuk, I. D. Najdenov, V. G. Klochkova, *et al.*, Bull. Spec. Astrophys. Obs. **44**, 127 (1998).
20. N. K. Rao and V. R. Venugopal, J. Astrophys. Astron. **6**, 101 (1985).
21. T. A. Ryabchikova, N. E. Piskunov, H. C. Stempels, *et al.*, Phys. Scr. **80** (1999), Proc. of ASOS6 (in press).
22. N. A. Sakhibullin, *Modeling Methods in Astrophysics, 1: Stellar Atmosphere* (Fén, Kazan, 1997).
23. V. Straizys, *Multicolor Stellar Photometry* (Mokslas, Vilnius, 1977; Pachart Publ. House, Tucson, 1992).
24. N. R. Trams, L. B. F. M. Waters, H. J. G. L. M. Lamers, *et al.*, Astron. Astrophys., Suppl. Ser. **87**, 361 (1991).
25. G. Walker, *Astronomical Observations. An Optical Perspective* (Cambridge Univ. Press, Cambridge, 1987; Mir, Moscow, 1990).
26. S. L. Wright, Commun. Univ. London Obs. **76**, 1 (1975).

Translated by V. Astakhov

Astronomy Letters, Vol. 27, No. 10, 2001, pp. 645–647. Translated from Pis'ma v Astronomicheskiĭ Zhurnal, Vol. 27, No. 10, 2001, pp. 758–761.

Why Do We See So Few Black Holes in Massive Binaries?

S. V. Karpov* and V. M. Lipunov

Sternberg Astronomical Institute, Universitetskiĭ pr. 13, Moscow, 119899 Russia

Received April 6, 2001

Abstract—We offer a simple explanation for the small number of black holes observed in pairs with massive stars. In detached massive binaries, spherically symmetric accretion takes place. This accretion could result in effective energy release in the hard band only if the equipartition of the gravitational and magnetic energy of plasma is established (Shvartsman's theorem). However, we show that due to the magnetic exhaust effect this equilibrium is virtually never established for the actual magnetic fields observed on massive stars: Shvartsman's theorem does not work. As a result, it is virtually impossible to detect black holes in detached massive binaries by currently available means (mainly, through X-ray observations). *© 2001 MAIK "Nauka/Interperiodica".*

Key words: *massive binaries, black holes*

INTRODUCTION

Simple estimates based on the Salpeter function and on the assumption that black holes are formed from massive (~40–50$M_\odot$) stars predict the presence of ~50–100 million black holes in our Galaxy. Despite all the uncertainties and the development of new exotic scenarios for the formation of stellar-mass black holes, the actual number of black holes in the entire Galaxy cannot be fewer than 10^7. Much of them must form pairs, for example, with massive stars. The expected number of massive binaries with black holes can be determined by multiplying the total number of black holes by the small ratio of the lifetime of a massive star to the Hubble time, i.e., $10^7 \times 10^6/10^{10} = 1000$. Here, we took the lifetime of a massive star, assuming that the optical companion (given the interchange of roles) is no less massive than the black-hole progenitor. Thus, one might expect ~1000 black-hole candidates in massive binaries. This number is in conflict with experimental data: we currently observe slightly more than ten candidates in binary systems. Remarkably, among these candidates only three belong to massive binaries, where they must be formed; moreover, some of them are not in our Galaxy. It should be added that the black-hole candidate Cygnus X-1 is a very close binary with an optical component that almost fills its Roche lobe. Clearly, there must be hundreds of times more detached binaries composed of a massive OB star and a stellar-wind accreting black hole. However, we do not see such systems.

Here, we draw attention to the fact that accretion in massive binary systems does not result in the effective generation of a hard radiation component, whose detection alone can point to the presence of a black-hole companion in the system. This is because the accretion in most systems of interest is spherically symmetric. This accretion can result in effective energy release in the hard band only if the equipartition is established between the magnetic and gravitational energies in the accretion flow.

However, the regime of magnetic exhaust operates in such systems (Lipunov 1987), which prevents the establishment of such equilibrium. As a result, most black holes in pairs with massive stars are unobservable.

NO DISK IS FORMED IN DETACHED MASSIVE BINARIES WITH A BLACK HOLE

First, we note that an accretion disk is virtually never formed in detached massive binaries with stellar wind. The condition under which the matter captured by the black hole does not form a disk is the smallness of its mean momentum (see, e.g., Lipunov 1987)

$$\eta_t \Omega R_G^2 < \sqrt{3 r_g G M},$$

$$\Omega^2 = \frac{G(M + M_*)}{a^3},$$

where $\eta_t < 1/4$ and the radius of capture R_G is determined from the equality of the wind kinetic and gravitational energies

$$\frac{1}{2}\rho V^2 = \frac{GM\rho}{R_G},$$

$$R_G = r_g\left(\frac{c}{V}\right)^2.$$

Accordingly, we constrain the velocity

* E-mail address for contacts: karpov@sai.msu.ru

$$V < V_{\rm cr} = c\eta_t^{1/4}\left(\frac{1+q}{3q}\right)^{1/8} r_{\rm g}^{3/8} a^{-3/8},$$

$$V_{\rm cr} = 500\eta_{0.1}^{1/4}\left(\frac{1+q_1}{3q_1}\right)^{1/8} M_{10}^{3/8} a_{200}^{-3/8}\ {\rm km\ s^{-1}}.$$

Since the stellar-wind velocity far from massive stars is no less than 1500–2000 km s^{-1}, an accretion disk is clearly never formed in such systems.

Note that the situation in Cygnus X-1 is completely different. The optical component virtually fills its Roche lobe, and the wind has not yet gathered speed at the distance of the black-hole orbit (about two stellar radii); therefore, favorable conditions for the formation of an accretion disk arise.

Thus, we emphasize the first important distinction of detached massive pairs with a black hole: the accretion in them is spherical.

WHAT CAN WE SEE IN BINARY SYSTEMS?

Because of the large optical luminosity of OB stars, the only evidence for the presence of a black-hole companion is hard X-ray radiation. The hard radiation from a black hole depends significantly on the accretion regime. Thus, for example, a classical accretion disk is optically thick and sinks slowly enough for the free–free radiation to become noticeable, which yields a considerable X-ray luminosity, while the situation for spherical accretion is much more complex.

In detached binaries, the rate of accretion from the stellar wind is always lower than the Eddington rate; i.e., the halo optical depth is very small. In the presence of even a very small initial field, the main energy release mechanism is electron synchrotron radiation. However, at typical accretion-flow temperatures, the synchrotron mechanism mainly produces optical radiation (Shvartsman 1971), which we cannot distinguish against the background of a normal star.

Which nonthermal mechanisms can produce a hard radiation component? Bremsstrahlung is ineffective (Shvartsman 1971); the inverse Compton effect would be important at an appreciable efficiency of energy release in the low-energy range and in the presence of a large number of hot electrons. However, for magnetic fields weaker than those for the equipartition, the efficiency of synchrotron energy release is low, and the hard Compton component is actually absent as well.

Note, however, that this situation radically differs from the advective accretion flow (ADAF) model, which has recently gained wide acceptance. Narayan's ADAF (Narayan and Yi 1995) is essentially a disk model; the efficiency of energy release in it is low even in the presence of a strong magnetic field because of the weak energy exchange between the radiating electrons and protons heated through viscous stresses.

In our case, however, the accreted matter has virtually no momentum, its motion is radial, the heating mechanism is compression (electrons and protons are heated equally), and, in general, the efficiency of energy release in the optical range does not need to be very low: only the hard radiation component is absent.

In the absence of equipartition, the conceivable generation mechanisms for the high-energy particles that could radiate in the hard band [turbulent acceleration, see Gruzinov and Quataert (1999); acceleration in fast reconnections, see Bisnovatyĭ-Kogan and Lovelace (2000)] do not work either.

Thus, we may say that the criterion for the absence of a hard radiation component and, accordingly, for a black hole being unobservable is whether an equipartition of the magnetic and gravitational energies has time to be established in the accretion flow.

STELLAR-WIND MAGNETIC FIELD

The magnetic field frozen in the outflow of matter from the star (stellar wind) must have a quasi-radial structure (the tangential components are suppressed at the wind acceleration stage); therefore, we can take the following law of variations in magnetic-field strength

$$B(r) = B_*\left(\frac{r_*}{r}\right)^2,$$

where B_* is the stellar surface magnetic field. Note that under this *a priori* assumption, the radial magnetic-field distribution does not depend (to within a small tangential component) on the stellar-wind acceleration law.

NO EQUIPARTITION IS ESTABLISHED

We cannot detect a black hole with spherically symmetric accretion when there is not enough time for an equipartition between the magnetic and gravitational energies to be established in the accretion flow.

The ratio of the magnetic- and gravitational-energy densities in the accreted matter with a frozen-in field increases with decreasing distance from the black hole as

$$\kappa = \frac{B^2}{8\pi}\frac{r}{GM\rho} \propto r^{-3/2}.$$

Accordingly, in order for an equipartition not to be established down to radius $R_{\rm eq} = r_{\rm eq}/r_{\rm g}$, it is necessary that within the stellar wind at the capture radius (where the wind kinetic energy is equal to the gravitational energy)

$$\kappa_0 < \left(\frac{R_{\rm G}}{r_{\rm g}}\right)^{-3/2} R_{\rm eq}^{3/2} = \left(\frac{c}{V}\right)^{-3} R_{\rm eq}^{3/2},$$

$$\kappa_0\left(\frac{c}{V}\right)^3 < R_{\rm eq}^{3/2},$$

$$\kappa_0 = \frac{B^2}{8\pi}\frac{2}{\rho V^2} = \frac{B^2}{8\pi}\frac{8\pi a^2}{\dot{M}_* V} = \frac{B^2 a^2}{\dot{M}_* c}\left(\frac{c}{V}\right) = \frac{B_*^2 r_*^4}{\dot{M}_* c a^2}\left(\frac{c}{V}\right).$$

Accordingly, the criterion for an equipartition not to be established in the accretion flow is

$$\frac{B_*^2 r_*^4}{\dot{M}_* c a^2}\left(\frac{c}{V}\right)^4 < R_{\rm eq}^{3/2}.$$

Normalizing the stellar radius to the solar radius, the outflow rate to $10^{-6}M_\odot$ year^{-1}, the binary's semimajor axis $200R_\odot$, and the radius $r_{\rm eq}$ at which an equipartition is established to $3r_{\rm g}$, we obtain

$$\left(\frac{B_*}{1\ {\rm G}}\right)^2\left(\frac{r_*}{1R_\odot}\right)^4\left(\frac{\dot{M}_*}{10^{-6}M_\odot/{\rm year}}\right)^{-1} \times\left(\frac{a}{200R_\odot}\right)^{-2}\left(\frac{1000\ {\rm km/s}}{V}\right)^4\left(\frac{r_{\rm eq}}{3r_{\rm g}}\right)^{-3/2} < 10^4. \quad (1)$$

Rewriting (1) as a condition on the initial magnetic field, we obtain

$$B_* < 1\left(\frac{r_*}{10R_\odot}\right)^{-2}\left(\frac{\dot{M}_*}{10^{-6}M_\odot/{\rm year}}\right)^{1/2}\left(\frac{a}{200R_\odot}\right) \times\left(\frac{1000\ {\rm km/s}}{V}\right)^{-2}\left(\frac{r_{\rm eq}}{3r_{\rm g}}\right)^{3/4}{\rm G}. \quad (2)$$

We know almost nothing about the magnetic fields on OB stars. Until now, no strong magnetic field has been detected in any OB star (Mathys 1998). However, the low accuracy of such measurements (~200–300 G) does not allow us to draw conclusions about the presence of a weak field, which is of interest here. Nevertheless, some theoretical considerations (the absence of convection and, accordingly, of dynamo mechanisms for field enhancement) also suggest that the magnetism on these stars is weak. That may be why accreting black holes are unobservable in such systems.

BLACK HOLES IN PAIRS WITH WOLF–RAYET STARS

As numerical simulations of the evolution of massive binaries show, a considerable fraction of binary systems with black holes survive after the second mass transfer, and pairs of helium stars (Wolf–Rayet stars) with black holes must be formed in nature. Their number must be an order of magnitude smaller than the number of such systems with OB stars, i.e., at least several tens in the Galaxy. Nevertheless, here, there is a conflict with observations as well. Apart from Cygnus X-3, no other black hole + Wolf–Rayet candidate systems are known at present.

Indeed, let us substitute the typical parameters of helium stars in (1) and (2). First, we take into account the fact that their radii are almost an order of magnitude smaller than those of OB stars, and, in general, their stellar-wind velocity (because of a higher escape velocity) is a factor of 2 or 3 higher, in some cases reaching 5000 km s^{-1}! This all makes the formation of an accretion disk in binary systems and the establishment of energy equipartition for spherical accretion unlikely, which may be responsible for the observed deficit of such systems.

CONCLUSION

We have shown that for the typical parameters of a wide massive star–black hole binary system, spherical accretion takes place. Massive OB and WR stars do not have strong magnetic fields; because of magnetic exhaust, the field in the accretion flow is also weak (weaker than for equipartition), and the matter cannot produce hard radiation. Accordingly, we cannot see the black hole. We actually see no hard radiation sources in wide pairs with such stars.

ACKNOWLEDGMENTS

We wish to thank V.S. Beskin, S.V. Bogovalov, and M.E. Prokhorov for fruitful discussions. This work was supported by the Russian Foundation for Basic Research (project no. 00-02-17164) and the State Science and Technology Program "Astronomy" (1.4.2.3).

REFERENCES

1. G. S. Bisnovatyĭ-Kogan and R. V. E. Lovelace, Astrophys. J. **529**, 978 (2000).
2. A. Gruzinov and E. Quataert, Astrophys. J. **520**, 248 (1999).
3. V. M. Lipunov, *Astrophysics of Neutron Stars* (Nauka, Moscow, 1987).
4. G. Mathys, in *Variable and Non-Spherical Stellar Winds in Liminous Hot Stars: Proceedings of IAU Colloquium No. 169, Heidelberg, 1998*, Ed. by B. Wolf, A. Fullerton, and O. Stahl (Springer-Verlag, Berlin, 1998); Lect. Notes Phys. **523**, 95 (1999).
5. R. Narayan and I. Yi, Astrophys. J. **444**, 231 (1995).
6. V. F. Shvartsman, Astron. Zh. **48**, 438 (1971) [Sov. Astron. **15**, 342 (1971)].

Translated by G. Rudnitskiĭ

Astronomy Letters, Vol. 27, No. 10, 2001, pp. 648–657. Translated from Pis'ma v Astronomicheskiĭ Zhurnal, Vol. 27, No. 10, 2001, pp. 762–773.

Observations of the X-ray Binaries 4U 1700-37 and GRO J1655-40 during the Grif Experiment onboard the Mir Orbiting Station

M. I. Kudryavtsev[1], S. I. Svertilov[2]*, and V. V. Bogomolov[2]

[1] *Space Research Institute, Russian Academy of Sciences, ul. Profsoyuznaya 84/32, Moscow, 117810 Russia*
[2] *Institute of Nuclear Physics, Moscow State University, Vorob'evy gory, Moscow, 119899 Russia*

Received March 23, 2001

Abstract—Various areas of the sky, including the Galactic-center region and the region with the X-ray binaries 4U 1700-37 and GRO J1655-40, were observed in the hard (10–300 keV) energy range during the Grif experiment onboard the Mir orbiting station. An epoch-folding analysis of the data has revealed periodicities with periods of 82 and 62 h, which are equal to the orbital periods of 4U 1700-37 and GRO J1655-40. Previously, these periodicities were observed during the Prognoz-9 X-ray experiment. Periodicities with periods in the range of days, 98 and 152 h, which were also observed during the Prognoz-9 experiment, were not revealed by the Grif data. We obtained upper limits on the intensities of these periodicities in various energy ranges. For the 62-h periodicity, we constructed an average 25–50-keV light curve and estimated the spectral flux density, which characterizes the intensity of the periodic component at different energies in different observing intervals during 1995–1997. The Prognoz-9 and Grif observations of GRO J1655-40 are compared with its CGRO, RXTE, and BeppoSax observations. The orbital periodicity is shown to manifest itself in the hard emission from the extremely bright X-ray transient GRO J1655-40, a likely black-hole candidate, even at the epochs between its X-ray outbursts. © *2001 MAIK "Nauka/Interperiodica".*

Key words: *space-borne observatories, X-ray binaries, periodicities, transients, X-ray novae*

INTRODUCTION

The timing characteristics of hard emission from X-ray binaries are an important channel for obtaining information on the high-energy processes in them. Of particular interest are observations of periodic X-ray and gamma-ray flux variations.

The main classes of X-ray binaries known to date are characterized by various types of periodic variability. This variability can result from the orbital motion of the binary's components (eclipse- or dip-type periodicities), from the rotation of the compact component (pulsations), and from the precession of an accretion disk (long-period cycles) or the spin axis of the compact object. Such periodic intensity variations were discovered in the emission from Galactic X-ray binaries during observations from UHURU, the first space-borne X-ray observatory (Giacconi *et al.* 1971; Forman *et al.* 1978), and were subsequently analyzed in detail during the flights of various spacecraft (see, e.g., Corbet 1986; Nagase 1989; and Priedhorsky and Holt 1987). Thus, hard X-ray and gamma-ray periodicities were studied from the Granat space-borne observatory (SIGMA; see, e.g., Sitdikov *et al.* 1993) during the BATSE/CGRO (Fishman *et al.* 1989) and OSSE/CGRO (Johnson *et al.* 1993) experiments, as well as from the BeppoSAX satellite (Frontera *et al.* 1998) and other spacecraft. The BATSE/CGRO long-term monitoring revealed periodicities in the hard emission from many X-ray pulsars (Bildsten *et al.* 1997). At present, the RXTE catalog (Levine 1999; Wen *et al.* 1999) appears to be most complete in terms of X-ray observations of orbital periods.

Periodicities in the hard (10–200 keV) emission from Galactic sources were studied during the Prognoz-9 X-ray experiment (Kudryavtsev and Svertilov 1984). Based on this experiment, we compiled a catalog of periods in the ranges of hours and days (Kudryavtsev *et al.* 1998). This catalog includes the periodicities that were previously observed in the X-ray emission from well-known astrophysical objects (4U 1700-37, 82 h; Cen X-4, 8.2 h; and 4U 1755-33, 4.4 h) (Kudryavtsev and Svertilov 1991; Kudryavtsev *et al.* 1995b) and new periodicities associated with sources in the Galactic-center region (152, 98, 67, 62, 13, 9.4, 7.8, 3.4, 1.96, and 1.45 h) (Kudryavtsev *et al.* 1988, 1998; Kudryavtsev and Svertilov 1992). At least two of the new periodicities in the range of days were found to be associated with X-ray novae: the 152- and 62-h periods were identified with Nova Ophiuchi 1977 (H 1705-25) (Kudryavtsev *et al.* 1996b) and Nova Scorpii 1994 (GRO J1655-40) (Kudryavtsev *et al.* 1998).

* E-mail address for contacts: sis@srdlan.npi.msu.su

We also obtained evidence that the 13-h period could be associated with the transient 4U 1543-47.

Analysis of the periodicities in the X-ray and gamma-ray emission from astrophysical objects was also one of the objectives of the Grif astrophysical program, which was carried out during 1995–1997 onboard the Mir space station (Pankov *et al.* 1990; Kudryavtsev *et al.* 1995a). In this paper, we analyze the Grif data regarding the search for and study of periodicities in the range of days, 62, 82, 98, and 152 h, which were previously observed during the Prognoz-9 experiment.

EXPERIMENTAL CONDITIONS

The Grif experiment was carried out on the Spectrum module of the Mir station (mean height ~400 km, orbital inclination 51°, orbital period ~90 min) from October 1995 through June 1997. Its objectives covered astrophysical observations (cosmic gamma-ray bursts, X-ray binaries, and pulsars), analyses of spatial distributions and variations of charged-particle and neutron fluxes in near-Earth space (Kudryavtsev *et al.* 1996a; Bogomolov *et al.* 1997), and methodological issues related to the background in gamma-ray astronomical experiments (Bogomolov *et al.* 1999, 2000).

The Grif experiment included four instruments:

(1) A PX-2 directional hard X-ray and gamma-ray scintillation spectrometer (photon energy range ΔE_γ = 10–300 keV, effective area S ~ 300 cm^2, field of view $\Omega \sim 1$ sr). This instrument was designed mainly for astrophysical observations, including patrols of solar flare activity.

(2) A NEGA-1 omnidirectional gamma-ray and neutron spectrometer (ΔE_γ = 0.15–50 MeV, E_n > 20 MeV, $S_\gamma \sim 250$ cm^2, $S_n \sim 20$ cm^2). This instrument was designed to study the characteristics of background gamma-ray and neutron fluxes on Mir orbits.

(3) A FON-1 charged-particle spectrometer (ΔE_e = 40–500 keV, ΔE_p = 1–3 MeV) with a large geometric factor $\Gamma \sim 80$ cm^2 sr. This instrument was designed to measure low charged-particle fluxes outside the Earth's emission belts.

(4) A FON-2 charged-particle spectrometer FON-2 (ΔE_e = 0.04–1.5 MeV, ΔE_p = 2–200 MeV) with a small geometric factor $\Gamma \sim 0.5$ cm^2 sr. This instrument was designed to measure large charged-particle fluxes in the emission belts.

The PX-2 data were used to search for and analyze periodicities in the hard emission from astrophysical objects (Pankov *et al.* 1989). The PX-2 instrument consisted of seven identical detection units and an electronic system, which processed and transformed information. The main detecting element in each detection unit was a CsI(Na) crystal (0.35 cm in thickness, 8.0 cm in diameter). Passive shielding was used to suppress background X-ray and gamma-ray emission. This shielding included an azimuthally symmetric lead collimator and lead (8 cm in diameter, 1.0 cm in thickness) and barium (8 cm in diameter, 0.5 cm in thickness) glasses, which absorbed the local emission from the spacecraft (the barium glass was intended to absorb the characteristic X-ray emission from lead). The detecting of charged particles by the PX-2 detection units was prevented by the phoswich method: the main detector, the passive shielding elements, and the collimator were placed under an anticoincidence cap of a plastic scintillator, which was viewed (from the lead glass) by the same photomultiplier as the CsI(Na) crystal. The events related to the detecting of charged particles in the plastic scintillator were identified by analyzing the time profile of the current pulse at the photomultiplier output. If the photomultiplier output signal contained a short (~5 ns in duration, corresponding to the characteristic decay time of the plastic scintillator) component of sufficient intensity, a special electronic circuit generated a logic inhibit signal, which was fed to the anticoincidence circuits. The triggering threshold of this phoswich circuit was chosen to ensure that no charged particles would be detected in the entire PX-2 energy range, 10 to 300 keV, with a 99% efficiency. The count rate of inhibit signals was measured in a separate charged-particle channel.

During the entire experiment, we measured the 5-s-averaged count rates of X-ray photons in the 10–50, 25–50, 50–100, 100–200, and 200–300 keV energy ranges and of the accompanying charged particles.

Each detection unit had a wide (~0.7 sr) field of view. Its beam, which was formed by the azimuthally symmetric collimator, was isotropic in azimuthal angle and linearly fell from maximum ($\theta = 0°$) to zero ($\theta = 45°$) in offset from the detector axis.

A major factor that determines the efficiency of X-ray and gamma-ray astronomical observations is known to be the acceptability of background conditions in a space experiment. One of the main peculiarities of the Grif experiment was the possibility of simultaneously monitoring all the principal components of background-producing emissions in near-Earth space on Mir orbits. Thus, for example, the NEGA-1 large-volume scintillation detectors independently detected the local gamma-ray photons and neutrons produced by the interaction of cosmic rays with the spacecraft material and the Earth's atmosphere. A sensitive FON-1 electron detector was used to check the sporadic increases in X-ray flux attributable to the detecting of bremsstrahlung from precipitating energetic magnetospheric electrons, which could simulate astrophysical phenomena (gamma-ray bursts, transients). Having a large geometric factor, it could detect even relatively small electron flux variations outside the zones of captured emission. The FON-2 charged-particle detector, which was free from overloads in the emission zones because of its small geometric factor, was used for background measurements when the Mir station crossed the Brazil anomaly region and spurs of the outer emission belt.

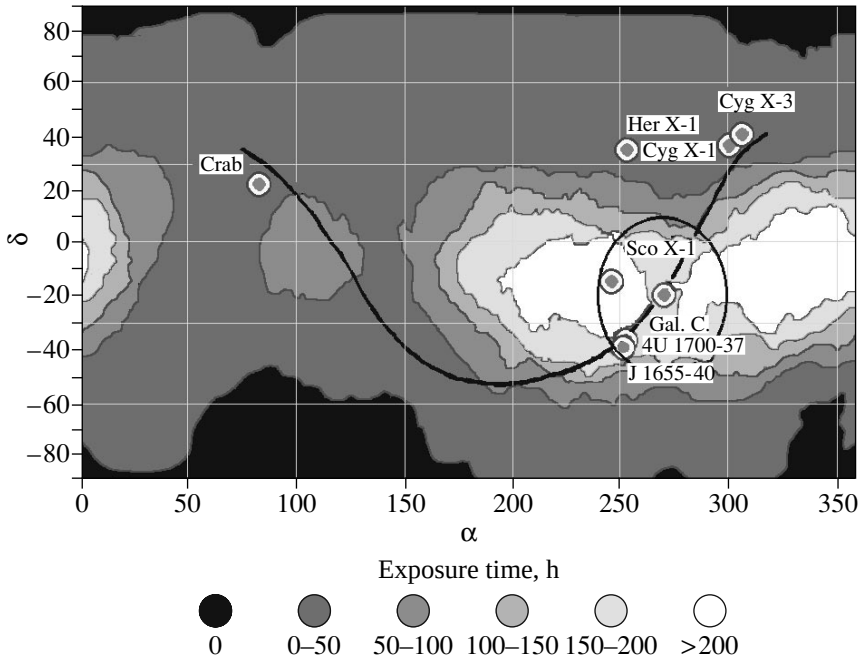

Fig. 1. The sky region observed during the Grif experiment onboard the Mir station, in equatorial coordinates. Different shades mark the sky areas observed with different exposure times. Some of the brightest sources of hard emission are indicated. The Galactic equator and the region whose boundaries correspond to the beam FWHM of PX-2 oriented to the Galactic-center region ($\alpha = 18^h00^m00^s$, $\delta = -22.^\circ0$) are marked.

It should be noted that, despite the intense and diverse background-emission variations, there were long periods during which the background conditions remained favorable for X-ray astronomical observations.

THE METHOD OF OBSERVING PERIODIC SOURCES DURING THE GRIF EXPERIMENT

The PX-2 detection units were positioned on the external panel of the Mir module in such a way that six units were arranged symmetrically around one central (seventh) unit. The axes of all seven detectors were separated by 5°. This arrangement and the large field of view of each detection unit, on the one hand, provided an overlapping (within ~35° of the central-detector axis) of the field of views of all units (in practice, this made it possible to use the total working area of all detectors when observing a given source) and, on the other hand, allowed the angular coordinates of sources to be estimated by a comparative analysis of the output data from individual detectors.

The PX-2 instrument was rigidly fixed to the module surface in such a way that the axis of its central detector (which coincided with the axis of the entire instrument) made 45° with the Spectrum axis (–*Y* axis of the Mir station) and with the Mir principal axis (+*X* axis). During the flight, there were two main orientations: three-axes stabilization and orbital (gravitational) orientation. In the former case, the Mir axes (and, accordingly, the PX-2 axes) had a fixed direction in space; i.e., the instrument was oriented to a specified point in the sky. The angle between the PX-2 axis and the nadir-zenith direction along the orbital turn varied over the range 0° (the direction toward zenith, i.e., toward the sky) to 180° (the direction toward nadir, i.e., toward the Earth), and, accordingly, the PX-2 field of view was regularly eclipsed by the Earth. In the latter case, the PX-2 axis was always directed at 45° to the zenith-nadir axis (i.e., the field of view of some of the detectors was shadowed by the Earth's atmosphere only slightly), and it slowly rotated in space with the Mir station in each turn during the flight. Thus, the sky was slowly scanned (~4° min^{-1}). During the entire experiment, various regions of the sky, including the Galactic-anticenter region, areas offset from the Galactic equator, and the Galactic-center region, could be observed.

Information was transmitted to the Earth in 16-h-long sessions of continuous observations; the interval between them typically ranged from several hours to several days. A total of ~200 sessions were conducted during the experiment, from which ~150 were chosen for subsequent analysis (sessions with many telemetry failures, incorrect times of output data writes, and the like were filtered out).

The sky region observed during the experiment is shown in Fig. 1 in equatorial coordinates. Different shades of gray represent the exposure time throughout the entire experiment that refers to the points with the corresponding coordinates. When estimating the expo-

sure time, we assumed the angle between the source direction and the PX-2 axis to be no larger than 30°. In addition, we excluded the Mir residence time in the regions of captured emission. As a condition for the source being not shadowed by the Earth, we considered the requirement of PX-2 orientation to the sky, i.e., the angle between the PX-2 axis and the nadir-zenith direction must have been in the range 0°–90°. The figure also shows the brightest X-ray sources and the Galactic equator.

We can assess the capabilities of the Grif experiment to study periodicities in hard emission from Galactic sources. The typical exposure time can be determined by using observing conditions for the Galactic center as an example. Figure 1 shows a circumference with a radius of 30° whose center coincides with the Galactic center. There are sources within the region in the sky bounded by this circumference during the observations of which the PX-2 effective area accounted for no less than 50% of its geometric area. As we see from the figure, the total observing time of the Galactic center with ≥50% efficiency was ~200 h. The exposure times of other Galactic sources (for example, 4U 1700-37) are similar. To separate periodicities, we analyzed the initial time series of mean count rates in the PX-2 X-ray channels by the epoch-folding technique (nonparametric regression; see, e.g., Terebizh 1992). Given the above mean exposure times and the mean count rates in the PX-2 X-ray channels (~2.5×10^{-1} pulses cm^{-2} s^{-1} in the 25–50 keV channel and ~1.2×10^{-1} pulses cm^{-2} s^{-1} in the 50–100 keV channel), the minimum detectable fluxes (5σ) that correspond to the intensities of periodic components with periods in the ranges of hours and days (≥7 h) for a purely statistical (Poisson) distribution of count rates are then ~4×10^{-5} phot. cm^{-2} s^{-1} in the 25–50 keV range (~10 mCrab) and ~10^{-5} phot. cm^{-2} s^{-1} in the 50–100 keV range (~5 mCrab).

Since the Mir orbit was peculiar (large orbital inclination and periodic crossings of the zones of captured emission), the PX-2 background count rates underwent variations. However, the combination of active and passive shielding of the PX-2 main detectors greatly reduced the background variations, in particular, the latitudinal variations in the main X-ray channels, 25–50 and 50–100 keV. At the same time, to extend the sensitivity range of the instrument using its readings in high-energy photon channels, we used a method that removed the count-rate variations attributable to latitudinal variations. This method is based on a regression analysis of readings in the PX-2 X-ray channels (N_x) and in the NEGA-1 gamma-ray channels (N_γ). Since the NEGA-1 detectors were inside the orbiting Mir module, they detected mainly the local gamma-ray emission. The additional count rate in a given X-ray channel attributable to the local emission may be assumed to depend linearly on the count rate of gamma-ray photons detected by NEGA-1. In this case, the initial count rates in the analyzed time series N_x can be represented as a superposition of the X-ray count rate proper $\tilde{N}_x$, which characterizes the photon flux under study, and the additional count rate αN_γ attributable to the local gamma-ray emission:

$$N_x = \tilde{N}_x + \alpha N_\gamma. \quad (1)$$

The linear regression coefficients α were determined over the entire observing interval when there were no bright sources of hard emission within the PX-2 field of view. The coefficients α were used to obtain the time series of count rates $\tilde{N}_x = N_x - \alpha N_\gamma$ for the subsequent analysis.

The suppression of background variations by using readings in the 150–500 keV gamma-ray channel yielded the most significant result. After applying the regression procedure, the residual variations in the X-ray channels attributable to the latitudinal variations accounted for no more than ~3% of the corresponding means, which is several times less than the expected amplitude of the variations attributable to the emission from the most intense Galactic sources.

For the subsequent analysis, we singled out the time series of 10-min-averaged X-ray count rates in various energy ranges, which were "cleaned" of background variations attributable to latitudinal variations. To separate periodicities by the epoch-folding technique, these time series were formed for intervals of observation of a particular source chosen according to the above criteria. We modified the epoch-folding technique by taking into account the peculiarities of the Mir experimental data. The analyzed observing intervals were broken down into segments whose duration was equal to the trial period under study. The sequences of count rates that corresponded to these segments were added together, and an average phase dependence of the count rate was constructed for this trial period. The amplitude of the process corresponding to the trial period (actual periodic or randomly simulated) can be described by the rms deviation (σ^2) of the numbers M_i, which constitute the average phase dependence:

$$\sigma^2 = \frac{\sum_{i=1}^{k} (M_i - \overline{M})^2}{k-1}. \quad (2)$$

Here, $\overline{M}$ is the mean count rate determined from the entire analyzed time series, $k = T/\Delta T$, where ΔT is the bin duration of the count rates constituting the average phase profile and T is the trial period. Here, when constructing a periodogram for each trial period, we calculated the average phase profiles broken down into 40 independent bins. For example, at an exposure time of ~200 h for 10-min averaging of the count rates that constituted the initial time series, there were, on the average, 30 independent count rates in each bin.

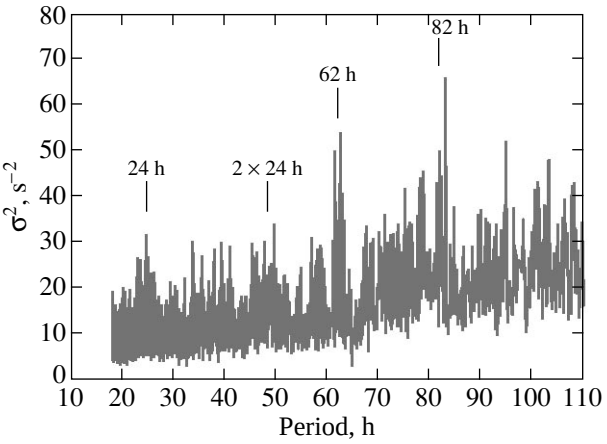

Fig. 2. The periodogram constructed by an epoch-folding analysis of the time series of 10-min-averaged photon count rates in the PX-2 25–50 keV channel obtained for the total exposure time when the instrument was oriented to the region with 4U 1700-37 and GRO J1655-40 (the PX-2 axis was offset from the point in the sky with $\alpha = 17^h00^m00^s$ and $\delta = -37\overset{\circ}{.}0$ by no more than 30°). The peaks corresponding to the 82-h (the orbital period of the X-ray binary 4U 1700-37) and 62-h (the orbital period of the X-ray binary GRO J1655-40) periods, as well as to the period of a day and its harmonic, are marked in the periodogram.

If the process that refers to the period under study simultaneously contains an actual periodicity and a noise component, because the processes are independent, σ^2 can be represented as the superposition

$$\sigma^2 = \sigma_p^2 + \sigma_{noise}^2, \quad (3)$$

where σ_p^2 and σ_{noise}^2 characterize the amplitudes of the corresponding components.

In general, the dependence $\sigma^2(T)$ (periodogram) can be represented as a superposition of a noise continuum (ideally, a smooth function of T) and discrete peaks corresponding to the fundamental period and its multiples for the present periodicities.

RESULTS

Figure 2 shows the periodogram constructed by the above method from the Grif experimental data for the time series of the count rates in the 25–50 keV channel selected for observing intervals in 1995–1997, when the PX-2 axis was oriented to the sky region with the well known sources of hard emission 4U 1700-37 and GRO J1655-40. The condition for choosing these observing intervals was the requirement that the offset of the PX-2 axis from the direction of 4U 1700-37 be no larger than 30° (since the angular positions of 4U 1700-37 and GRO J1655-40 are close in the sky, the time series constructed for the latter under the same condition for the PX-2 axis offset virtually coincided with the time series for 4U 1700-37). The periodogram exhibits distinct discrete peaks that correspond to periods of 62 and 82 h. A number of broad peaks corresponding to periods of 24, 48, and 72 h, which are attributable to the diurnal variations of the instrumental background in the PX-2 channels, are also seen on the periodogram. The significance of the separated peaks is specified by the dispersion σ_σ, which characterizes the scatter of points on the noise portions of the continuum near the analyzed peak. The noise continuum on the periodogram is determined by a set of various factors, including shot noise, attributable to a finite number of detected photons with a Poisson distribution, nonperiodic variations in the flux from the source within the PX-2 field of view; and variations in the instrumental background. The amplitudes of the peaks marked in Fig. 2 are $5.5\sigma_\sigma$ (62 h) and $8\sigma_\sigma$ (82 h). Assuming a normal (Gaussian) distribution of the noise values of $\sigma^2(T)$, this leads us to conclude that the corresponding periodicities are statistically significant [see Kudryavtsev *et al.* (1998) for more details on the selection criterion for significant peaks].

As was pointed out above, the 82- and 62-h periodicities associated with these objects were previously observed in the hard emission during the Prognoz-9 experiment. The 82-h period is the orbital period of the eclipsing X-ray binary 4U 1700-37, which is known from observations of several space experiments: UHURU (Jones *et al.* 1973), OSO-8 (Dolan *et al.* 1980), EXOSAT (Doll and Brinkmann 1987), BATSE CGRO (Rubin *et al.* 1996), SIGMA Granat (Sitdikov *et al.* 1993), and others. The 62-h period is equal, within the error limits, to the optical orbital period of the X-ray binary GRO J1655-40 (Bailyn *et al.* 1995), which is known as the X-ray Nova Scorpii 1994 (Zhang *et al.* 1994).

Average phase dependencies (light curves) were constructed for the most probable periods corresponding to the periodicities in 4U 1700-37 and GRO J1655-40.

Figure 3 shows the average 25–50 keV light curves obtained for the 82-h period during the Prognoz-9 (1983–1984) and Grif experiments. Also shown in the figure is the average 20–120 keV light curve for 4U 1700-37 obtained from its long-term BATSE observations (Rubin *et al.* 1996). The curves constructed from different experimental data were brought into coincidence by the middles of the phases of intensity minima. The curves shown in the figure have similar eclipse-type shapes with a characteristic rapid rise and fall in X-ray flux at orbital phases close to the eclipse phase. As we see from the figure, the duration of the eclipse phase, as inferred from the data of all three experiments, is virtually the same, ~15% of the period. The fluxes indicated for the Prognoz-9 and Grif curves were determined by taking into account the actual offset of the source from the instrumental axis and characterize its absolute observed luminosity. As follows from the figure, the mean 25–50 keV intensities of the 82-h periodicity in both experiments are equal, within the error limits. Given such a peculiarity of 4U 1700-37 as

the quasi-stationarity of its hard emission, this equality of the light-curve amplitudes may be considered an additional energy calibration of the PX-2 X-ray channels and suggests that its energy thresholds are essentially constant. A comparison of the light curves obtained during the Prognoz-9 and Grif experiments, on the one hand, and during the BATSE/CGRO experiment, on the other, indicates that the measured fluxes, which characterize the source's observed luminosity in various energy ranges, agree with one another.

The Prognoz-9 (1983–1984) and Grif average 25–50 keV light curves for the 62-h period are shown in Fig. 4. Also shown in this figure is the light curve (Kudryavtsev *et al.* 1998) obtained by averaging the OSSE/CGRO observational data (Kroeger *et al.* 1996) for GRO J1655-40 over the 62-h period. The orbital period for this system was found from optical observations to be 2.62 days = 62.9 hours (Bailyn *et al.* 1995), which is equal to the 62-h period, within the error limits. The Prognoz-9 and CGRO light curves were brought in coincidence in phase based on the maximum of the correlation coefficient between the 25–50 keV (Prognoz-9) and 50–100 keV (OSSE/CGRO) light curves, which is 0.76 (Kudryavtsev *et al.* 1998). The Grif and Prognoz-9 curves were brought into coincidence by the middles of the phases of intensity minima. We see from the figure that the shapes of all time profiles agree with one another, although it should be noted that the Grif profile is slightly asymmetric compared to the Prognoz-9 profile. The durations of the minimum phase, as inferred from the data of all three experiments, are almost equal, ~10% of the period. Since the X-ray nova GRO J1655-40 is known to be a highly variable source, it would be unreasonable to expect the amplitudes of the 62-h periodicity measured in its hard emission to be equal at different epochs. At the same time, as follows from Fig. 4, the intensities of the 62-h periodicity measured during the Prognoz-9, Grif, and OSSE/CGRO experiments may be considered to agree with one another, at least to within an order of magnitude.

Based on the time series of count rates in the PX-2 10–50, 25–50, and 50–100 keV channels, we also constructed periodograms for the observing intervals when the PX-2 axis was oriented to the Galactic center and to the region with H1705-25 (Nova Ophiuchi 1977; Watson *et al.* 1978) by the epoch-folding technique. As was noted above, during the Prognoz-9 observations, the 98-h periodicity was separated in the hard emission from the Galactic-center region and the 152-h periodicity was identified with H1705-25. However, the Grif periodograms for the above PX-2 orientation revealed no significant peaks corresponding to the 98- and 152-h periods. We cannot rule out the possibility that the corresponding exposure time ($\leq$200 h) for the 152-h periodicity is not enough for its more or less reliable separation by the epoch-folding technique. The estimated upper limits on the spectral flux densities averaged over the 10–50, 25–50, and 50–100 keV energy ranges, which characterize the intensities of the 98- and 152-h periodicities, show that they cannot exceed the values given in the table, within 1σ.

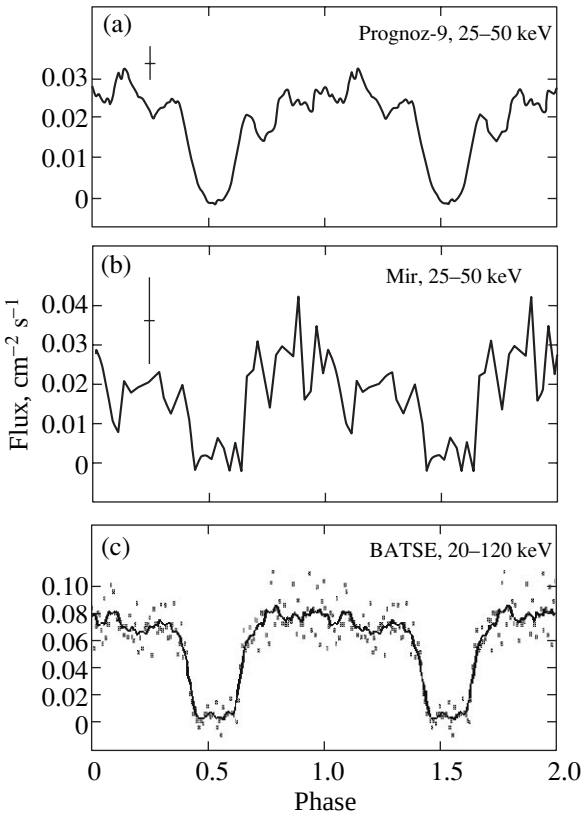

Fig. 3. The average phase profiles of hard emission from the X-ray binary 4U 1700-37 (T = 82 h) obtained through the (a) Prognoz-9 (Kudryavtsev *et al.* 1998), (b) Grif/Mir, and (c) BATSE/CGRO (Rubin *et al.* 1996) observations.

DISCUSSION

Thus, by comparing the results of the searches for periodicities in Galactic sources of hard emission during the Prognoz-9 and Grif experiments, we conclude that among those processes with periods in the range of days that were detected in 1983–1984, the 62- and 82-h periodicities continued to be observed in 1995–1997. The fact that the 98- and 152-h periods were not observed in 1995–1997 can be explained by the nature of their sources. Since the 152-h periodicity was identified with an object belonging to the class of X-ray novae, which are known to be highly variable on various time scales, we conclude that this object (H1705-25) was not active in 1995–1997. A similar conclusion can be reached with regard to the source of the 98-h periodicity. Although this source has not been identified, it appears to also be a highly variable transient-type object.

Of great interest is the activity of the source of the 62-h periodicity, the X-ray Nova Scorpii 1994

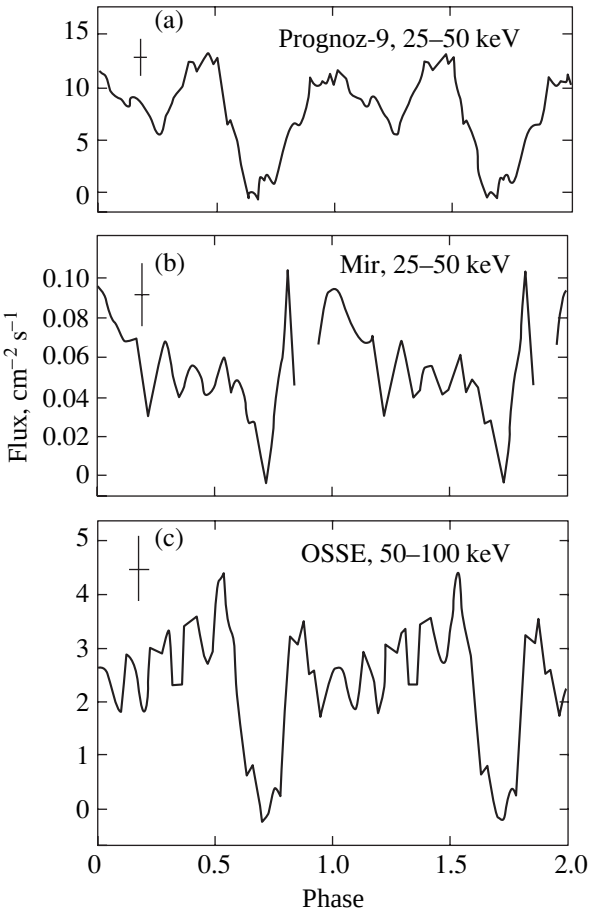

Fig. 4. The average phase profiles of hard emission from the bright X-ray transient GRO J1655-40, a black-hole candidate (T = 62 h), obtained through (a) the Prognoz-9 observations in November–December 1983 (Kudryavtsev *et al.* 1998), (b) the Grif/Mir observations in November 1995–June 1997, and (c) the OSSE/CGRO observations in August and December 1994 and March–April 1995 (Kroeger 1996; Kudryavtsev *et al.* 1998).

(GRO J1655-40). The X-ray binary GRO J1655-40 is a unique astrophysical object in all respects. Apart from the fact that this source is considered among the main black-hole candidates, it shows up during radio observations as the so-called microquasar, an object with jets, i.e., plasma ejections moving in opposite directions at relativistic velocities ($v/c = 0.92 \pm 0.02$) (Hjellming and Rupen 1995; Tavani *et al.* 1996). The corresponding peaks in periodograms were used to determine the amplitudes of the 62-h periodicity in various energy ranges. Given the mean offset of the source from the instrumental axis, this made it possible to determine the spectral flux density of the periodicity at various energies for the specified spectral representation. The power-law energy dependence of the spectral flux density, which characterizes the intensity of the 62-h periodicity averaged over the observing period from November 1995 until June 1997, is shown in Fig. 5.

Table

Period	25–50 keV	50–100 keV	100–200 keV
98 h	$<5.8 \times 10^{-4}$ cm^{-2} s^{-1} keV^{-1}	$<9.0 \times 10^{-5}$ cm^{-2} s^{-1} keV^{-1}	$<3.1 \times 10^{-4}$ cm^{-2} s^{-1} keV^{-1}
152 h	$<9.1 \times 10^{-4}$ cm^{-2} s^{-1} keV^{-1}	$<2.6 \times 10^{-4}$ см$^{-2}$ с$^{-1}$ keV^{-1}	$<2.2 \times 10^{-4}$ cm^{-2} s^{-1} keV^{-1}

It is of interest to compare the Prognoz-9 and Grif observations of the GRO J1655-40 activity and other observations (see Fig. 6). The activity of this object in its hard emission, which has subsequently become known as the X-ray Nova Sco 1994 (Zhang *et al.* 1994; Harmon *et al.* 1995), was apparently first observed during the Prognoz-9 experiment in 1983 (Kudryavtsev *et al.* 1998). According to the CGRO data, this source was most active in the hard energy range from July 1994 through August 1995 (Kroeger *et al.* 1996; Zhang *et al.* 1997). Subsequently, late in April 1996, an outburst was again detected first in the soft X-ray (2–10 keV) range with the All Sky Monitor (ASM) of the RXTE Observatory and, about a month later, in the hard energy range at the Compton Gamma-ray Observatory (Hynes *et al.* 1998). The source continued to be more or less active at least for 16 months (Remillard *et al.* 1999), and it was observed from various spacecraft, including RXTE, CGRO, and BeppoSAX. To trace the dynamics of its activity from the Grif data, we searched for the 62-h period on three independent observing intervals that corresponded to the following epochs: November 16, 1995–January 6, 1996; October 23, 1996–January 9, 1997; and May 12–June 18, 1997. For each of these intervals, we constructed time series of the data selected according to the condition of the instrumental axis being oriented toward GRO J1655-40. These time series in various energy ranges (10–50, 25–50, 50–100, and 100–200 keV) were then analyzed by the epoch-folding technique. Although the fluxes that characterize the amplitude of the 62-h periodicity cannot be reliably determined because of the smaller amount of data on individual time intervals (see Fig. 6), it should be noted that the amplitude of the periodicity was largest during November 16, 1995–January 6, 1996. At this epoch, which occurred at the time between the periods of the source's highest activity, the RXTE and BeppoSAX Observatories were not yet operational. The BATSE/CGRO data (see Fig. 6) suggest that the activity in the source's hard emission between outbursts is characterized by fluxes $\sim(3\text{–}5) \times 10^{-2}$ phot. cm^{-2} s^{-1} in the 20–200 keV energy range. The intensity of the 62-h periodicity in the hard emission from GRO J1655-40 was estimated from the Grif data for the entire observing period (1995–1997) to be $\sim(4.5 \pm 1.85) \times 10^{-2}$ phot. cm^{-2} s^{-1} (25–200 keV), which agrees with the BATSE/CGRO upper limit on the total flux, within the error limits. The flux that characterizes the amplitude of the 62-h periodicity for the observing interval November 16, 1995–January 6, 1996, apparently exceeds this limit insignificantly because of large measurement errors.

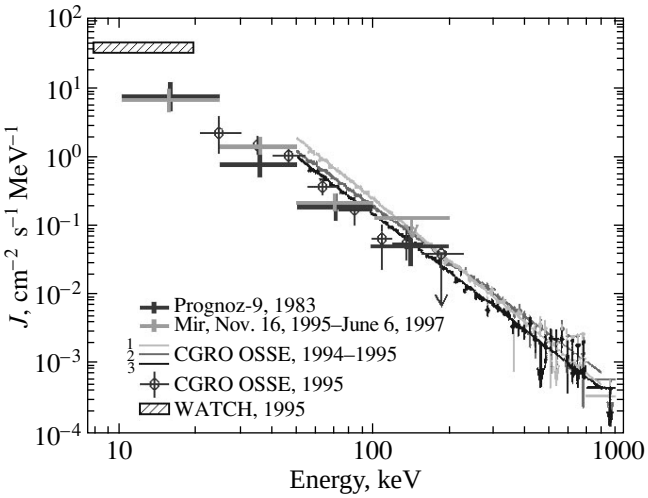

Fig. 5. The Prognoz-9 and Grif/Mir energy dependencies of spectral flux density (J), which characterize the intensity of the 62-h periodicity in the hard emission from GRO J1655-40. Also shown are the measurements of the spectral density, which characterizes the total flux in different energy ranges, during the OSSE/CGRO (August 1994, line *1*; December 1994, line *2*; March–April 1995, line *3*; Kroeger *et al.* 1996), BATSE/CGRO, and WATCH/Granat (both in July–August 1995; Zhang *et al.* 1997) observations of the source's outbursts.

It is generally believed that GRO J1655-40 belongs to the class of soft X-ray transients and, according to theoretical models based on optical and X-ray observations, is a low-mass binary composed of an F3–F4 star with a mass of 1.7–3.3$M_\odot$ and a black hole with a mass of 5.5–7.9$M_\odot$ as the compact component (Bailyn *et al.* 1995; Orosz and Bailyn 1997; van der Hooft *et al.* 1998; Shanbaz *et al.* 1999). At the same time, it has a number of atypical properties for X-ray binaries of this type (Esin *et al.* 2000). As was pointed out above, the 62-h period observed in the hard energy range is equal to the optically measured orbital period. According to data from the PCA and ASM instruments onboard the RXTE Observatory, narrow (~1 min in duration) dips were traceable on the X-ray (2–12 keV) light curve during the outbursts of GRO J1655-40 in April 1996–October 1997. These dips occurred at phases 0.72–0.86 of the orbital cycle, which is known from optical measurements; the dip occurrence period (62.9112 h) is virtually equal to the optical orbital period (Kuulkers *et al.* 1998). At this time (August–October 1996, March–April, August, 1997), such dips were also observed in the soft X-ray (2–8 keV) emission from GRO J1655-40 with the WFC instrument onboard the BeppoSAX Observatory. According to the WFC data, dips occurred

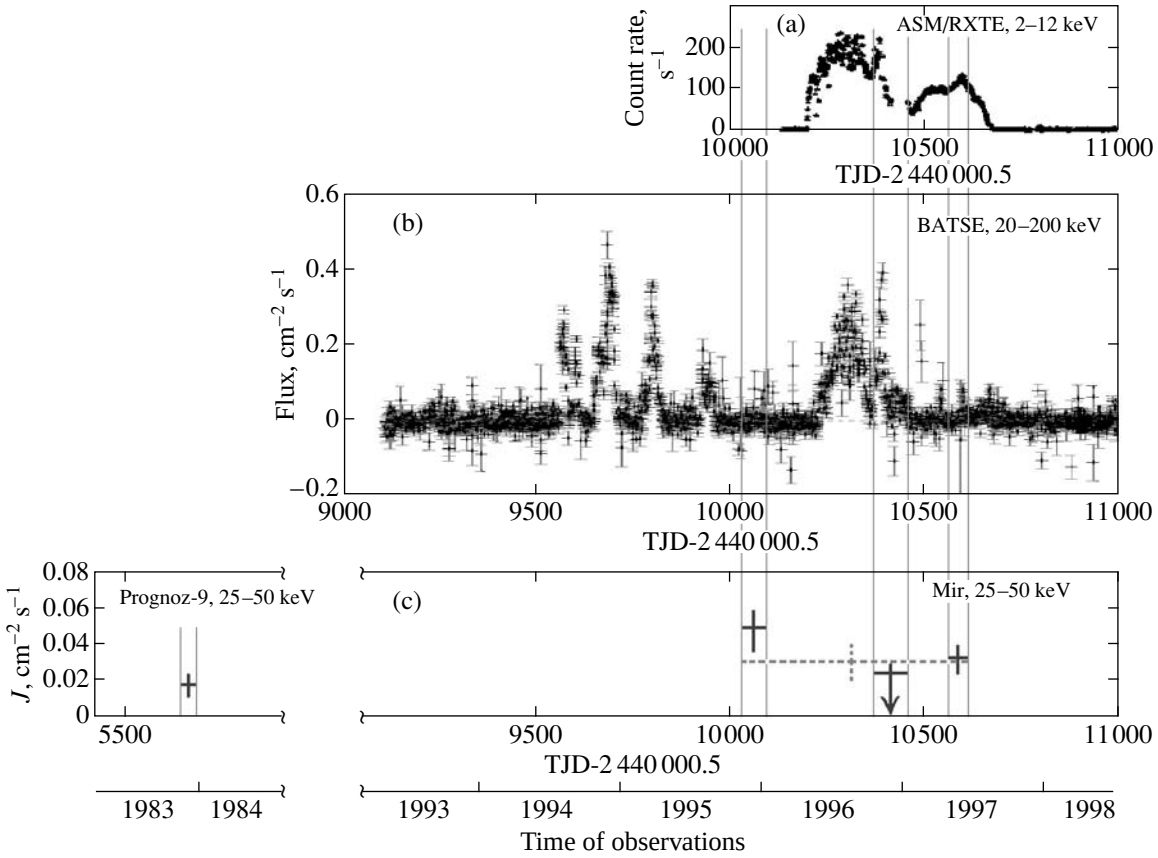

Fig. 6. The light curves of GRO J1655-40 in the (a) X-ray (ASM/RXTE observations; Kuulkers *et al.* 1998) and (b) hard (BATSE/CGRO; Gerels *et al.* 2000) energy ranges during various periods of its activity in 1994–1997. (c) The fluxes in the 62-h periodicity estimated at different epochs during the Prognoz-9 (1983) and Grif/Mir (1995–1997) observations.

at orbital phases 0.68–0.89 (Kuulkers *et al.* 2000). Because of the presence of dips at certain orbital phases, the X-ray light curve proves to be modulated with the orbital period; this periodicity is not eclipsing in nature, because, despite the large modulation depth (~92%), the flux did not drop to zero even at minima on the light curve. The duration of the phases of reduced intensity on the X-ray light curve attributable to dips accounts for ~0.2 of the orbital period (Kuulkers *et al.* 1998). The duration of the phase of minimum on the Prognoz-9, Grif, and OSSE/CGRO average phase profiles for the hard emission is similar (see Fig. 4). It should be noted that the BATSE/CGRO data revealed no manifestations of the periodicity in the hard emission from GRO J1655-40 (Zhang *et al.* 1996). This may be because the amplitude of the 62-h periodicity in the hard energy range depends weakly on the total flux. In that case, the periodicity would show up most clearly when the source's activity is relatively low (to all appearances, the Prognoz-9 and Mir observations occurred precisely at such epochs). However, during outbursts, the total flux can increase by more than an order of magnitude. This severely hampers the observation of the periodicity, because it proves to be strongly noised by fluctuations in the total flux.

Thus, the Prognoz-9 and Grif/Mir observations lead us to conclude that there is a strict periodicity in the hard emission from GRO J1655-40, which is traceable during difference cycles of the source's activity separated by a long time interval (~12 years). This periodicity is apparently attributable to the orbital motion of the binary's components. The energy spectrum of the 62-h periodicity in the emission from GRO J1655-40 agrees with various spectral measurements of the total hard flux from this source and, thus, is consistent with the model of a two-component spectrum typical of compact binaries, black-hole candidates (Shakura and Sunyaev 1973). The observation of the 62-h periodicity in the hard emission from GRO J1655-40 at different epochs suggests that even between its X-ray outbursts, the source was not completely quiescent in the hard energy range. In particular, it was active between the X-ray outbursts in August 1995 and February 1996. This gives grounds to reduce the typical recurrence time, which is important for estimating the mean rate mass transfer from the binary's optical companion to its compact object $\dot{M}_T$ (Esin *et al.* 2000) by at least half. The Grif data also suggest that, given the source's distance of ~3.5 kpc (Hjellming and Rupen 1995), its luminosity between X-ray outbursts in the periodicity of hard emission at energies $E \geq 25$ keV is $\sim 4 \times 10^{35}$ erg s^{-1}, which is more than three orders of magnitude higher than the luminosity that has been believed to be typical of the quiescent state of such objects (Esin *et al.* 2000).

REFERENCES

1. C. Bailyn, J. Orosz, J. McClintock, and R. Remillard, IAU Circ., No. 6173 (1995).
2. L. Bildsten, D. Chakrabarty, J. Chiu, *et al.*, Astrophys. J., Suppl. Ser. **113**, 367 (1997).
3. A. V. Bogomolov, V. V. Bogomolov, Yu. I. Denisov, *et al.*, Izv. Akad. Nauk, Ser. Fiz. **63**, 1665 (1999).
4. A. V. Bogomolov, V. V. Bogomolov, Yu. I. Denisov, *et al.*, Kosm. Issled. **38**, 377 (2000).
5. A. V. Bogomolov, Yu. I. Logachev, M. I. Kudryavtsev, *et al.*, Izv. Akad. Nauk, Ser. Fiz. **61**, 1130 (1997).
6. R. H. D. Corbet, Mon. Not. R. Astron. Soc. **220**, 1047 (1986).
7. J. F. Dolan, M. J. Coe, C. J. Grannell, *et al.*, Astrophys. J. **238**, 238 (1980).
8. H. Doll and W. Brinkmann, Astron. Astrophys. **173**, 86 (1987).
9. A. A. Esin, J.-P. Lasota, and R. I. Hynes, Astron. Astrophys. **354**, 987 (2000).
10. G. J. Fishman, C. A. Meegan, R. B. Wilson, *et al.*, in *Proceedings of the GRO Scientific Workshop, Greenbelt, NASA/GSFC, 1989*, Ed. by W. N. Johnson, p. 2.39.
11. W. Forman, C. Jones, L. Cominsky, *et al.*, Astrophys. J., Suppl. Ser. **38**, 357 (1978).
12. F. Frontera, D. Dal Fiume, G. Malaguti, *et al.*, astro-ph/9802078 (1998).
13. N. Gerels, J. Norris, and J. D. Myers, http://coscc.gsfc.nasa.gov/batse/hilev/occ.html, webmaster J. D. Myers (2000).
14. R. Giacconi, H. Gursky, E. Kelly, *et al.*, Astrophys. J. Lett. **167**, L67 (1971).
15. B. A. Harmon, C. A. Wilson, S. N. Zhang, *et al.*, Nature **374**, 703 (1995).
16. R. M. Hjellming and M. P. Rupen, Nature **375**, 464 (1995).
17. R. I. Hynes, C. A. Haswell, C. R. Shrader, *et al.*, Mon. Not. R. Astron. Soc. **300**, 64 (1998).
18. W. N. Johnson, R. L. Kinzer, J. D. Kurfess, *et al.*, Astrophys. J., Suppl. Ser. **86**, 693 (1993).
19. C. Jones, W. Forman, H. Tananbaum, *et al.*, Astrophys. J. Lett. **181**, L43 (1973).
20. R. A. Kroeger, M. S. Strickman, J. E. Grove, *et al.*, Astron. Astrophys., Suppl. Ser. **120**, 117 (1996).
21. M. I. Kudryavtsev and S. I. Svertilov, Vestn. Mosk. Univ., Ser. 3: Fiz., Astron. **25**, 81 (1984).
22. M. I. Kudryavtsev and S. I. Svertilov, Pis'ma Astron. Zh. **17**, 410 (1991) [Sov. Astron. Lett. **17**, 175 (1991)].
23. M. I. Kudryavtsev and S. I. Svertilov, Pis'ma Astron. Zh. **18**, 588 (1992) [Sov. Astron. Lett. **18**, 235 (1992)].
24. M. I. Kudryavtsev, Yu. I. Logachev, and S. I. Svertilov, Pis'ma Astron. Zh. **14**, 893 (1988) [Sov. Astron. Lett. **14**, 379 (1988)].
25. M. I. Kudryavtsev, V. M. Pankov, A. V. Bogomolov, *et al.*, in *Proceedings of the 24th International Cosmic Ray Conference, 1995a*, Vol. 3, p. 567.
26. M. I. Kudryavtsev, S. I. Svertilov, and V. V. Bogomolov, Pis'ma Astron. Zh. **21**, 256 (1995b) [Astron. Lett. **21**, 224 (1995b)].

27. M. I. Kudryavtsev, V. M. Pankov, A. V. Bogomolov, *et al.*, Izv. Vyssh. Uchebn. Zaved., Ser. Radiofiz. **39**, 1539 (1996a).
28. M. I. Kudryavtsev, S. I. Svertilov, and V. V. Bogomolov, Pis'ma Astron. Zh. **22**, 896 (1996b) [Astron. Lett. **22**, 803 (1996b)].
29. M. I. Kudryavtsev, S. I. Svertilov, and V. V. Bogomolov, Pis'ma Astron. Zh. **24**, 663 (1998) [Astron. Lett. **24**, 572 (1998)].
30. E. Kuulkers, R. Wijnands, T. Belloni, *et al.*, Astrophys. J. **494**, 753 (1998).
31. E. Kuulkers, J. J. M. in't Zand, R. Cornelisse, *et al.*, Astron. Astrophys. **358**, 993 (2000).
32. A. M. Levine, Nucl. Phys. B (Proc. Suppl.) **69**, 196 (1999).
33. F. Nagase, Publ. Astron. Soc. Jpn. **41**, 1 (1989).
34. J. A. Orosz and C. D. Bailyn, Astrophys. J. **82**, 1086 (1997).
35. V. M. Pankov, M. I. Kudryavtsev, Yu. G. Shkurkin, *et al.*, in *Proceedings of the IV International Workshop "Scientific Space Instrument-Making,"* Ed. by V. M. Balebanov (Inst. Kosm. Issled. Akad. Nauk SSSR, Frunze, 1990), Part 3, p. 42.
36. W. C. Priedhorsky and S. S. Holt, Space Sci. Rev. **45**, 291 (1987).
37. R. A. Remillard, E. H. Morgan, J. E. McClintock, *et al.*, Astrophys. J. **522**, 397 (1999).
38. B. S. Rubin, M. H. Finger, B. A. Harmon, *et al.*, Astrophys. J. **459**, 259 (1996).
39. N. I. Shakura and R. A. Sunyaev, Astron. Astrophys. **24**, 337 (1973).
40. T. Shanbaz, F. van der Hooft, J. Casares, *et al.*, Mon. Not. R. Astron. Soc. **306**, 689 (1999).
41. A. F. Sitdikov, M. R. Gilfanov, R. A. Sunyaev, *et al.*, Pis'ma Astron. Zh. **19**, 483 (1993) [Astron. Lett. **19**, 188 (1993)].
42. M. Tavani, A. Fruchter, S. N. Zhang, *et al.*, Astrophys. J. Lett. **473**, L103 (1996).
43. V. Yu. Terebizh, *Analysis of Astrophysical Time Series* (Nauka, Moscow, 1992).
44. F. van der Hooft, M. H. M. Heemskerk, F. Alberts, and J. van Paradijs, Astron. Astrophys. **329**, 538 (1998).
45. M. G. Watson, M. J. Ricketts, and R. E. Griffiths, Astrophys. J. Lett. **221**, L69 (1978).
46. L. Wen, H. Bradt, W. Cui, *et al.*, in *Proceedings of the American Astronomical Society HEAD Meeting, 1999*, Vol. 31, p. 3406.
47. S. N. Zhang, C. A. Wilson, B. A. Harmon, *et al.*, IAU Circ., No. 6046 (1994).
48. S. N. Zhang, B. A. Harmon, W. S. Paciesas, *et al.*, Astron. Astrophys., Suppl. Ser. **120**, 227 (1996).
49. S. N. Zhang, K. Ebisawa, R. A. Sunyaev, *et al.*, Astrophys. J. **479**, 381 (1997).

Translated by V. Astakhov

Astronomy Letters, Vol. 27, No. 10, 2001, pp. 658–670. Translated from Pis'ma v Astronomicheskiĭ Zhurnal, Vol. 27, No. 10, 2001, pp. 774–787.

On the Excitation of Free Oscillations on the Moon

T. V. Gudkova* and V. N. Zharkov

Schmidt Joint Institute of Physics of the Earth, Russian Academy of Sciences, ul. Bol'shaya Gruzinskaya 10, Moscow, 123810 Russia

Received April 26, 2001

Abstract—Since the Moon's outer shells are very inhomogeneous, a global, spherically symmetric model of its interior structure is difficult to construct by using only seismic body-wave data. We study the diagnostic capabilities of the free-oscillation method. The sources of the largest moonquakes are located in the outer 200-km thick layer. Their seismic moments reach 10^{22} dyn. cm. Current seismometers are capable of detecting ground accelerations of $\sim 10^{-8}$ cm s^{-2}. Taking $M_0 \approx 10^{22}$ dyn. cm, we show that torsional modes ${}_nT_l$ with $l \geq 7$ and $n = 0$ (l is the degree of oscillation, and n is the overtone number) can be detected. These modes contain information about the outer layers to a depth of ≈500 km and can allow a global model to be constructed for the outer, most inhomogeneous layers of the satellite. The largest moonquakes excite spheroidal modes ${}_nS_l$ much worse, and it is unlikely that they can be detected with current instruments. We provide detailed information on the excitation of free oscillations for various moonquake focal mechanisms and focal depths. © *2001 MAIK "Nauka/Interperiodica".*

Key words: *seismology, planetary internal structure, free oscillations*

INTRODUCTION

Besides the Earth, the Moon is the only cosmic body in the Solar system for which seismic data have been obtained. These data suggest that its internal structure is very inhomogeneous. The outer (15–20 km) scattering layer is particularly inhomogeneous. The presence of this layer results in long lunar seismograms and makes it difficult to interpret the arrival of body waves. The Moon has a crust, a mantle, and a core; the lower part of the mantle possesses significant dissipative properties and may be partially molten (Latham *et al.* 1973; Toksoz *et al.* 1974; Nakamura *et al.* 1974; Goins *et al.* 1981; Nakamura 1983).

The seismic models of the lunar interiors (seismic velocity profiles of longitudinal, V_P, and transverse, V_S, waves) proposed by different authors (Bills and Ferrari 1977; Goins *et al.* 1981b; Nakamura 1983; Khan *et al.* 2000) based on analyses of lunar seismograms differ markedly (Fig. 1a, Table 1). This difference can be explained by the low quality of S-arrivals in the seismograms due to the signal weakness and due to intense scattering in the low velocity, high-Q upper crust (Dainty *et al.* 1974). When seismic velocity profiles are constructed, lateral inhomogeneities close to the seismic stations also introduce significant systematic errors. The method used by Khan *et al.* (2000) allowed the possible error limits for the velocity profiles to be determined (Fig. 1b).

Until recently, the crust thickness has been taken to be 60 km in virtually all models (Table 1). A reanalysis of the lunar seismic data (Chenet *et al.* 2000; Khan *et al.* 2000) has yielded a crust thickness of 45 km. The crust thickness was determined near the seismic stations, and it was referred to the Moon's near side. An analysis of "Clementine" and "Lunar Prospector" data on the gravitational field and topography (Smith *et al.* 1997; Lemoin *et al.* 1997; Konoplive *et al.* 1998) has shown that the lunar crust thickness varies over a wide range, ≈20–110 km (Hood and Zuber 2000), with its average thickness for the Moon's far side being appreciably larger than for the near side.

Judgments on the lunar core radius are still preliminary. The model by Nakamura *et al.* (1974) allows for the existence of a lunar core with a radius of 170–360 km. Based on current gravitational-field data, Konoplive *et al.* (1998) found the Moon's core radius to be in the range 220–450 km. The radius of the Moon's metallic core (340 ± 90 km) was estimated by Hood *et al.* (1999), who analyzed the data obtained when the Moon passed through the Earth's magnetospheric tail.

Thus, the core radius, the seismic velocity distribution, and the locations of possible density discontinuities in the lunar mantle are still uncertain.

One of the central problems is to construct a spherically symmetric model of the Moon's interior structure, which, as in the case of the Earth, could serve as a zero approximation, a reference model. Since the Moon's outer layers are very inhomogeneous, it is difficult to use body waves to construct the interior structure model in the zero approximation. For this purpose, data on the free-oscillation spectrum and surface waves are more

* E-mail address for contacts: gudkova@uipe-ras.scgis.ru

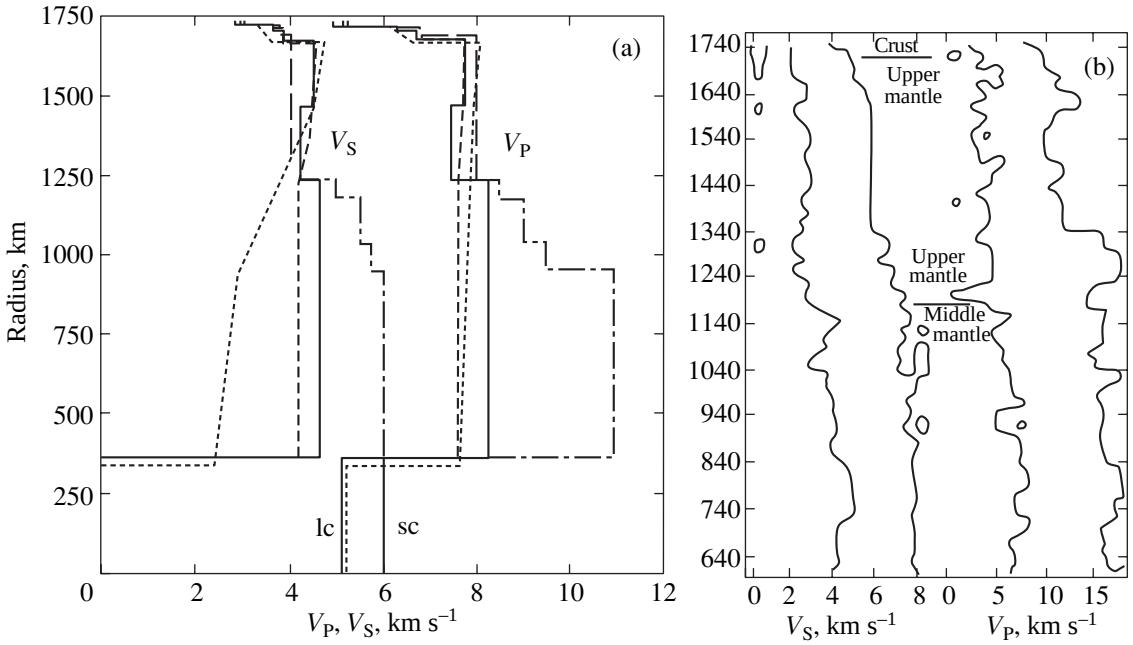

Fig. 1. (a) A composite plot of the velocity distributions for longitudinal V_P and transverse V_S waves in the Moon's seismic models by Khan *et al.* (2000) (dot-dashed lines), Nakamura (1983) (solid lines), Goins *et al.* (1981b) (dashed lines), and Bills and Ferrari (1977) (dotted lines) and (b) the band of possible velocity distributions in the model by Khan *et al.* (2000) due to uncertainty in the data.

suitable. The second problem is to obtain information on the lunar core by seismic methods. The Moon has a small core surrounded by a low-*Q* layer. That may be why the body P- and S-waves from far-side moonquakes that passed through the lunar core were not recorded at the Moon's seismic stations.

The free-oscillation spectra and dispersion curves for surface waves for the various models of the Moon's interior structure available at that time were computed by Takeuchi *et al.* (1961), Carr and Kovach (1962), Derr (1969), Bolt and Derr (1969), and Zharkov *et al.* (1969). A detailed review on the seismology of the Moon was published by Lognonne and Mosser (1993).

Previously (Gudkova and Zharkov 2000), we studied the diagnostic capabilities of the torsional-oscillation method for sounding the Moon's interior structure; calculated the periods of torsional oscillations for the n = 2–100 fundamental modes and four overtones for several models with no core, with a liquid core, and with a solid core and constructed the dispersion curves for Love waves; calculated and tabulated the derivatives of the dimensionless eigenfrequency with respect to the dimensionless shear modulus and density, which can be used to determine the corrections to the model density and shear modulus distributions due to their small changes; and considered the damping of torsional oscillations.

To judge whether the free-oscillation method can be used to study the lunar interiors, it is necessary to estimate the amplitudes for various types of free oscillations during moonquakes and to determine how these amplitudes depend on focal depth and excitation processes based on the available data for the Moon's seismic activity and the sensitivity of current instruments.

In this paper, we consider the free-oscillation method for sounding the lunar interiors. We calculate the amplitudes of torsional and spheroidal oscillations for sources at different depths and with different focal mechanisms using the velocity model by Nakamura (1983) (MNlc model), which, as can be seen from Fig. 1a, is a characteristic model.

PECULIARITIES OF THE LITHOSPHERIC MOONQUAKES

The Moon's seismic activity was studied by Lammlein *et al.* (1974), Toksoz (1975), Binder and Oberst (1985), Oberst (1987), Lognonne and Mosser (1993), and Lognonne *et al.* (1996).

More than twelve thousand seismic events were recorded on the Moon. They were classified as meteoritic impacts, shallow moonquakes (or high-frequency teleseismic moonquakes), and deep moonquakes.

We are primarily interested in the strongest shallow moonquakes, which are summarized in Binder and Oberst (1985) and Oberst (1987); parameters for some of these moonquakes are listed in Table 2. Over five years of the seismic station network operation, 28 such events were recorded (Fig. 2). These events are not repeated at the same place and do not correlate with the characteristic lunar tidal periods. The sources of these moonquakes are variously estimated (Nakamura *et al.*

Table 1. Seismic wave velocities in the models, $x = r/1738$

Region	Radius, km	V_P, km s^{-1}	V_S, km s^{-1}
MB model (Bills and Ferrari 1977)			
Core	0–338	$5.220 - 0.206x$	0
Lower mantle	338–938	$7.613 + 0.347x$	$2.219 + 1.243x$
Transition region	938–1438	$7.631 + 0.314x$	$0.068 + 5.227x$
Upper mantle	1438–1668	$6.522 + 1.654x$	$2.400 + 2.406x$
Crust	1668–1718	$20.23 - 14.29x$	$10.37 - 7.143x$
	1718–1738	5.22	3.02
MG model (Goins *et al*. 1981b)			
Lower mantle	?–1258	7.6 ± 0.6	4.2 ± 0.1
Transition region	1258–1338	$(6.813 + 1.087x) \pm 0.15$	$(1.524 + 3.696x) \pm 0.05$
Upper mantle	1338–1678	$(7.255 + 0.513x) \pm 0.15$	$(3.580 + 1.026x) \pm 0.05$
Crust	1678–1718	6.8	3.9
	1718–1738	5.1	2.96
MN model (Nakamura 1983)			
Core	0–350	5.1(6.0)	0(2.8)
Lower mantle	350–1238	8.26 ± 0.40	4.65 ± 0.16
Transition region	1238–1468	7.46 ± 0.25	4.25 ± 0.10
Upper mantle	1468–1678	7.74 ± 0.12	4.49 ± 0.03
Crust	1678–1708	6.68	3.86
	1708–1723	6.25	3.61
	1723–1737	4.9	2.83
	1737–1738	0.51	0.294
MK model (Khan *et al*. 2000)			
Lower mantle	?–958	11.0 ± 2.1	6.0 ± 0.7
Transition region	958–1038	9.0 ± 1.9	5.5 ± 0.9
	1038–1133	9.9 ± 1.9	5.9 ± 0.9
	1133–1193	8.5 ± 1.5	4.8 ± 4.8
Upper mantle	1193–1693	8.0 ± 0.8	4.0 ± 0.4
Crust	1693–1718	6.7	3.61
	1718–1738	4.9	2.83

Note: The data in parentheses are for a solid core.

1979; Goins 1978; Khan *et al.* 2000) to be located in the 200-km cold part of the thick lunar lithosphere. For such events, the largest seismic moment M_0 is $\approx 10^{22}$ dyn. cm. For some moonquakes, the stress drops reach 2000 bar.

For the Earth, the stress drops are ~50 bar. The seismic moment is known to be defined as the product of the shear modulus, the fault area, and the average displacement on the fault plane ($M_0 = \mu Sb$). The elastic energy W is equal to the work of the average stress τ on the fault plane ($W = Sb\bar{\tau}$). We see that for the same energy, the larger is the stress drop, the smaller is the fault area and, naturally, the smaller is the fault size; that is why long waves are excited worse.

By terrestrial standards, the strongest moonquakes are weak. However, since the background seismic noise on the Moon is very low, seismometers that are many orders of magnitude more sensitive than those employed on the Earth can be used to record such events (Lognonne *et al.* 1996).

The deep moonquakes that correlate with lunar tides are much weaker than lithospheric moonquakes and are not considered here.

As we will see below, mainly torsional oscillations and Love waves are excited during lithospheric moonquakes. The kinetic energy released during the largest meteoritic impacts detected by the Apollo lunar seismic station network is estimated to be 10^{18}–10^{19} erg (Goins *et al.* 1981a). However, since the coefficient of seismic efficiency is very small, $\approx 10^{-3}$–10^{-5} (Melosh 1989), such impacts actually do not excite free oscillations. To excite free oscillations requires the impacts of very large meteorites with energies that are several orders of

Table 2. Lithospheric moonquakes [the data from Binder and Oberst (1985), Oberst (1987), and Khan *et al*. (2000)]

Event, year, day	Seismic moment, dyn. cm	Energy release, J	Stress drop Δ, bar	Latitude, longitude	Body-wave magnitude	Source depth, km
1971, 107	4.4×10^{21}	$>9.2 \times 10^{11}$	>1000	48° N, 35° E	>5.5	75 ± 21
1971, 140	6.6×10^{20}	$>2.1 \times 10^{10}$	>150	42° N, 24° W	>4.8	48 ± 46
1972, 2	2.3×10^{21}	$>1.5 \times 10^{11}$	>300	54° N, 101° E	>5.1	173 ± 55
1973, 72	6.6×10^{21}	$>2.1 \times 10^{12}$	>1500	84° S, 134° W	>5.6	49 ± 35
1973, 171	1.3×10^{21}	$>8.0 \times 10^{10}$	>300	1° S, 71° W	>5	115 ± 23
1974, 192	2.5×10^{21}	$>3.0 \times 10^{11}$	>550	21° N, 88° E	>5.3	133 ± 41
1975, 3	1.6×10^{22}	$>6.9 \times 10^{12}$	>2100	29° N, 98° W	>5.8	75 ± 16
1975, 12	1.1×10^{21}	$>5.8 \times 10^{10}$	>250	75° N, 40° E	>5	102 ± 26
1976, 12	1.1×10^{21}	$>3.6 \times 10^{10}$	>150	38° N, 44° E	>4.9	
1976, 66	3.0×10^{21}	$>2.6 \times 10^{11}$	>400	50° N, 20° W	>5.3	74 ± 27

magnitude higher. Naturally, recording such events would be of great scientific interest.

RESULTS

The Moon's free-oscillation spectrum consists of torsional and spheroidal modes.

In a spherical coordinate system $r(r, \theta, \phi)$, where r is the radius, θ is the polar distance, and ϕ is the longitude, the components of displacement vector $\mathbf{s}(s_r, s_\theta, s_\phi)$ are

$$s_r = 0,$$
$$s_\theta = imW(r)\operatorname{cosec}\theta Y_l^m(\theta, \phi), \quad (1)$$
$$s_\phi = -W(r)\partial_\theta Y_l^m(\theta, \phi)$$

for torsional oscillations
and

$$s_r = U(r)Y_l^m(\theta, \phi),$$
$$s_\theta = V(r)\partial_\theta Y_l^m(\theta, \phi), \quad (2)$$
$$s_\phi = imV(r)Y_l^m(\theta, \phi)$$

for spheroidal oscillations,
where

$$X_l^m(\theta) = (-1)^m\left[\frac{(2l+1)(l-m)!}{4\pi(l+m)!}\right]^{1/2}P_l^m(\cos\theta),$$
$$(0 \le m \le l) \quad (3)$$
$$X_l^m(\theta) = X_l^{-m}(\theta),$$
$$Y_l^m(\theta, \phi) = X_l^m(\theta)\exp[im\phi]$$

is the spherical function of degree l and order m and $P_l^m(\cos\theta)$ are the associated Legendre polynomials.

Since the model is spherically symmetric, the eigenfrequencies do not depend on m and depend only on l and n, the radial number (overtone number), which is equal to the number of nodes along the radius in the functions $W(r)$ and $U(r)$ for torsional and spheroidal oscillations, respectively. The oscillation modes depend on all three indices. The free-oscillation problem for planets was described in detail by Alterman *et al.* (1959) and, as applied to the case under consideration, by Gudkova and Zharkov (1996a, 1996b). This problem can be numerically solved by the finite-difference method.

For $m = -l, -l + 1, \ldots, l$, eigenfunctions ${}_ns_l^m(x)$ correspond to each eigenfrequency ${}_n\omega_l = 2\pi/{}_nT_l$. Denote the torsional and spheroidal oscillations by ${}_nT_l$ and ${}_nS_l$, respectively.

The kinetic energy for the torsional and spheroidal modes is given by the formulas

$$E_{\text{tors}} = \omega^2\int\rho r^2W^2dr, \quad (4)$$

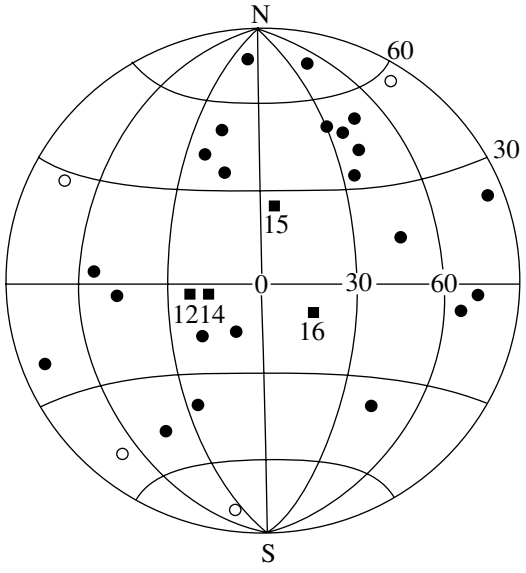

Fig. 2. The distribution of lithospheric moonquake epicenters (Binder and Oberst 1985) and the locations of Apollo seismic stations. The open circles refer to far-side events.

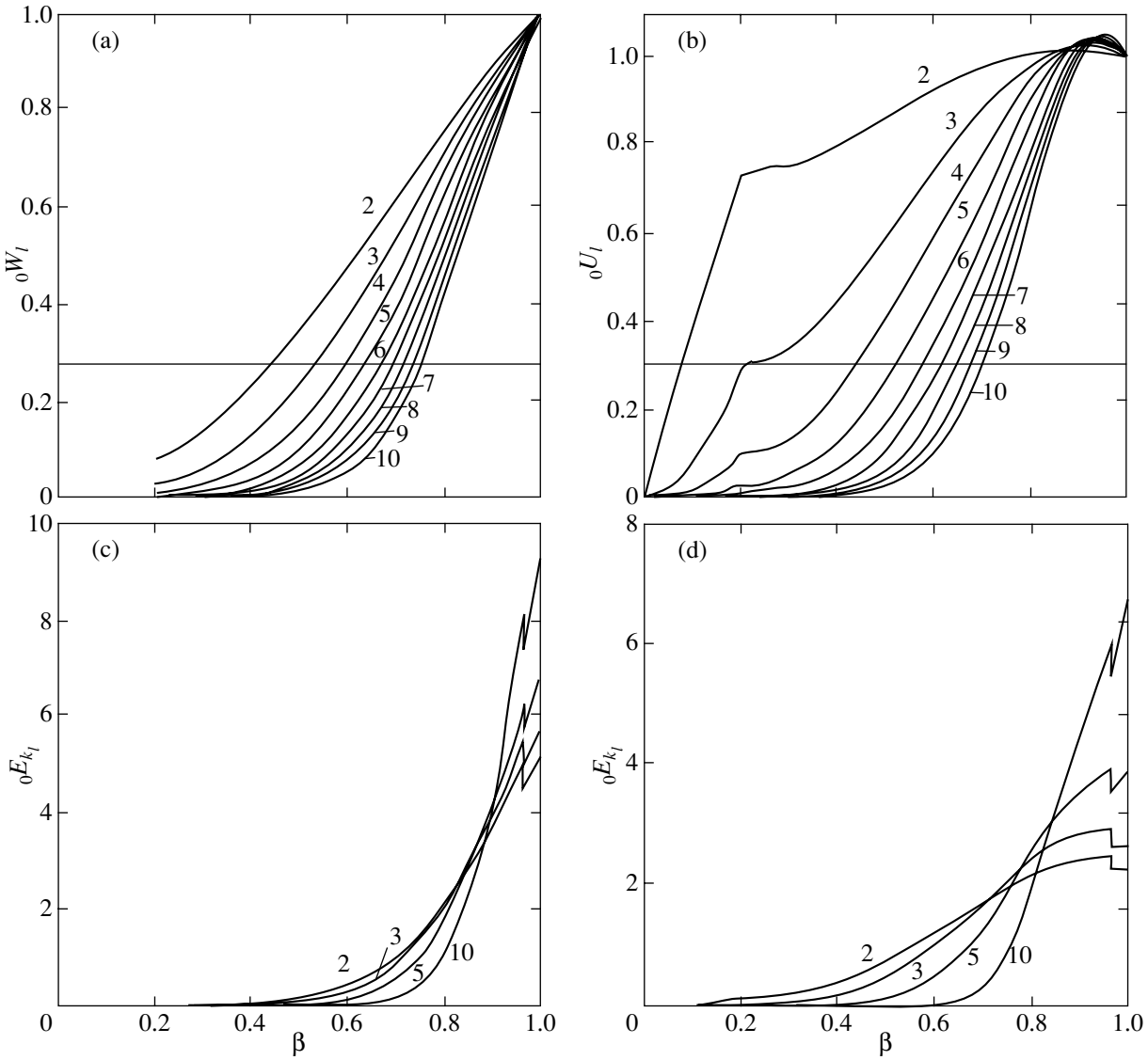

Fig. 3. The functions (a) $_0W_l$ and (b) $_0U_l$ proportional to the displacements of torsional and spheroidal oscillations for the fundamental mode, l = 2–10, and the kinetic energy $_0E_{k_l}$ for (c) torsional and (d) spheroidal oscillations, l = 2,3,5, and 10, versus relative radius $\beta = r/R$. In (a, b), $_0W_l$ and $_0U_l$ are on the surface, and in (c, d), the areas under the curves are normalized to unity.

$$E_{\text{spher}} = \omega^2 \int \rho r^2 [U^2 + l(l+1)V^2] dr. \qquad (5)$$

The radial functions $_0U_l(r)$ and $_0W_l(r)$ for the MN model with a liquid core (MNlc) are shown in Fig. 3. In Figs. 3a and 3b, the amplitudes of these functions are normalized to unity at the Moon's surface. Qualitatively, the eigenmodes sound regions of the lunar interior with displacements ≥0.3 (Zharkov 1986). The crust

Table 3. The periods of torsional oscillations for the MNlc model (min)

n/l	2	3	4	5	6	7	8	9	10
0	16.57	10.79	8.228	6.717	5.704	4.970	4.412	3.972	3.615
1	5.669	4.792	4.170	3.704	3.341	3.049	2.810	2.609	2.438
2	3.812	3.365	3.018	2.748	2.529	2.347	2.193	2.059	1.943
3	2.867	2.630	2.415	2.335	2.085	1.956	1.843	1.743	1.655
4	2.305	2.174	2.029	1.894	1.777	1.678	1.591	1.515	1.447
5	1.910	1.834	1.740	1.643	1.554	1.477	1.409	1.347	1.292
6	1.623	1.579	1.522	1.456	1.387	1.322	1.264	1.212	1.165
7	1.414	1.385	1.347	1.301	1.248	1.195	1.146	1.103	1.065
8	1.245	1.225	1.199	1.168	1.133	1.094	1.054	1.017	0.983
9	1.115	1.102	1.085	1.063	1.038	1.008	0.975	0.942	0.911
10	1.012	1.001	0.988	0.972	0.952	0.929	0.904	0.877	0.851

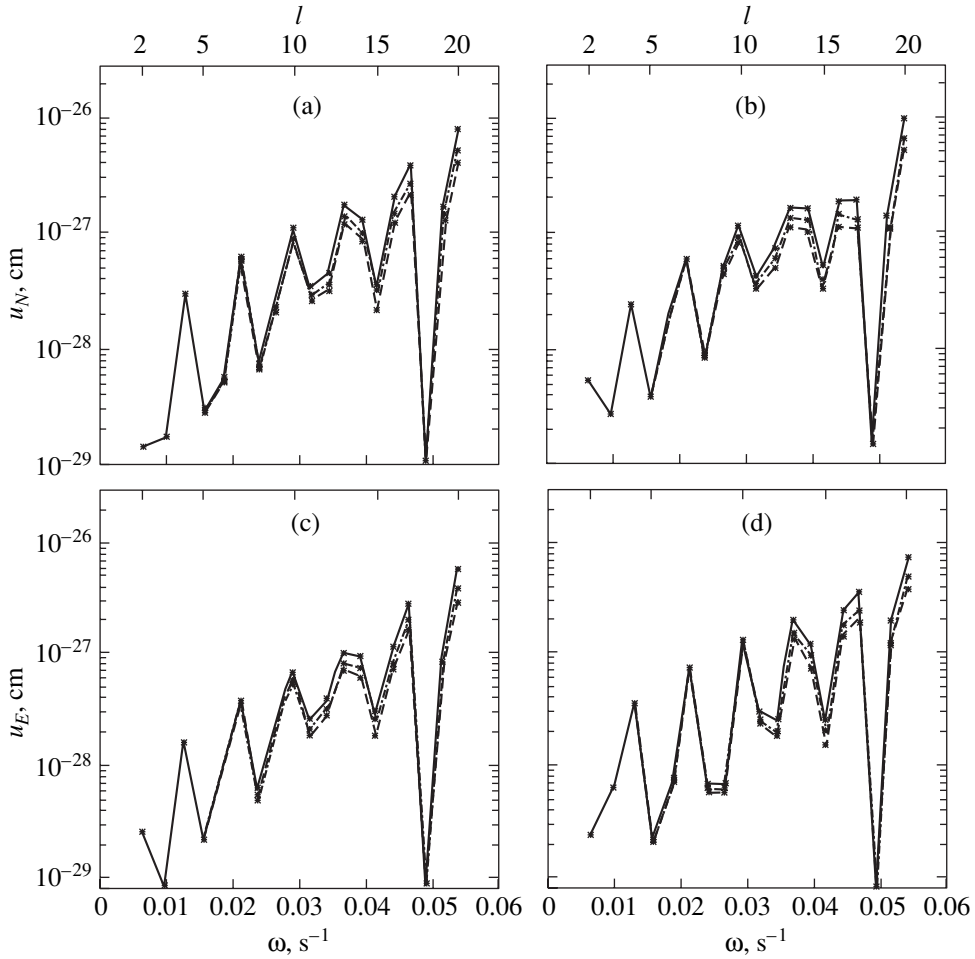

Fig. 4. The amplitude of displacements u_N (a, b) and u_E (c, d) for the modes of torsional oscillations with l = 2–20 and n = 0 versus frequency $\omega = 2\pi/T$ and degree of oscillation l for two focal mechanisms. M_0 is set equal to 1. The focal mechanisms are 45°, 45°, 45° (a, c) and 90°, 90°, 0° (b, d) for the dip, strike, and slip angles at focal depths of 50 km (solid lines), 150 km (dot-dashed lines), and 200 km (dashed lines). The epicenter coordinates are 29° N, 98° W; the seismometer coordinates are 0° N, 45° W; and the epicentral distance is 58°.

and the upper mantle are sounded by torsional oscillations with $l \approx 60$ and $l \approx 10$–20, respectively; the sounding of the middle mantle (transition zone) begins with $l \approx 7$; the lower mantle is controlled by $l \approx 2$–7; and only torsional oscillations with l = 2 and 3 penetrate the core. As we see from Fig. 3, spheroidal oscillations with $l < 3$ penetrate the core and oscillations with $l \approx 3$–80 and $l > 80$ sound the mantle and the crust, respectively. Figures 3c

Table 4. The periods of spheroidal oscillations for the MNlc model (min.)

n/l	2	3	4	5	6	7	8	9	10
0	15.59	10.23	8.050	6.760	5.868	5.199	4.673	4.244	3.887
1	8.847	6.545	5.217	4.356	3.750	3.302	2.959	2.688	2.470
2	5.846	4.648	3.778	3.310	2.994	2.739	2.523	2.337	2.175
3	4.181	3.682	3.233	2.738	2.414	2.220	2.070	1.945	1.838
4	3.945	3.354	2.904	2.568	2.246	2.010	1.858	1.736	1.634
5	2.952	2.723	2.526	2.333	2.135	1.901	1.699	1.591	1.502
6	2.584	2.289	2.120	1.995	1.882	1.774	1.646	1.476	1.367
7	2.329	2.148	1.942	1.771	1.652	1.569	1.495	1.424	1.322
8	1.972	1.873	1.781	1.692	1.589	1.481	1.389	1.313	1.252
9	1.838	1.661	1.549	1.487	1.428	1.369	1.310	1.249	1.190
10	1.660	1.605	1.509	1.395	1.304	1.241	1.193	1.150	1.109

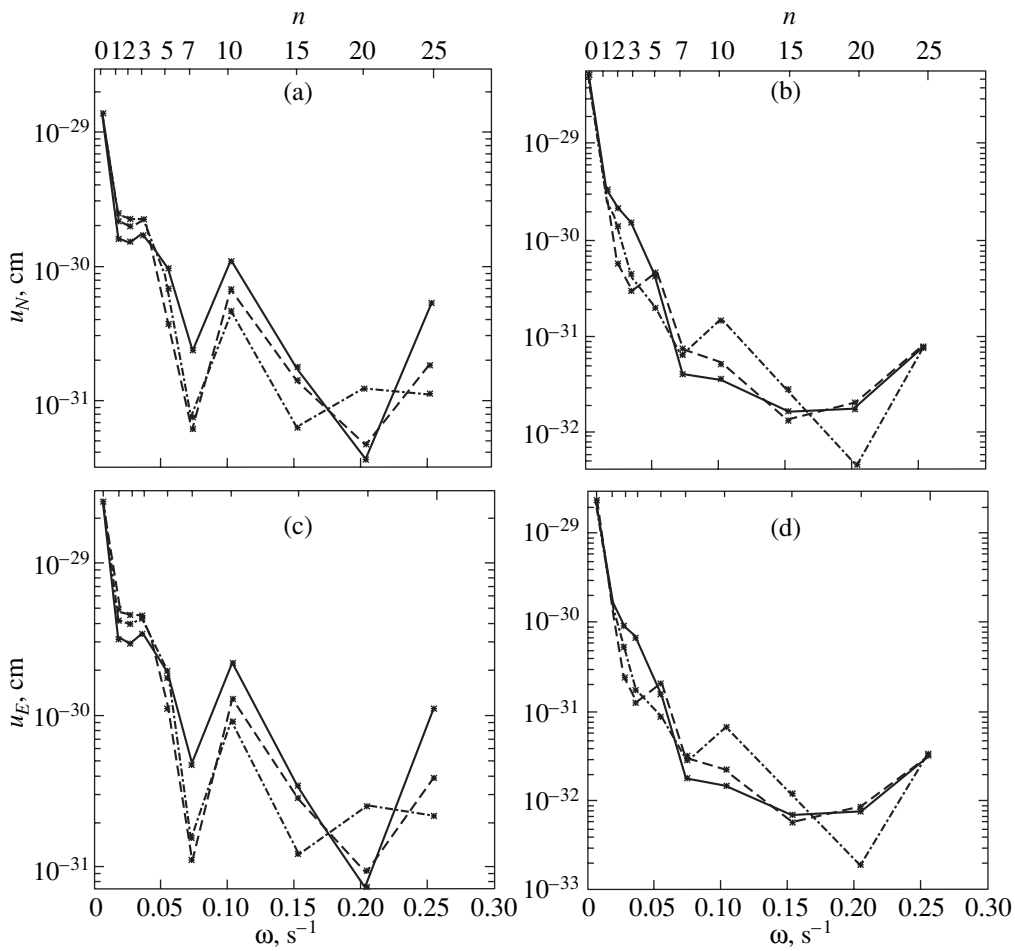

Fig. 5. The amplitudes of displacements u_N (a, b) and u_E (c, d) for the $l = 2$ fundamental tone of torsional oscillations and for the 1, 2, 3, 5, 7, 10, 15, 20, and 25 overtones for two focal mechanisms versus frequency $\omega = 2\pi/T$ and overtone number n. See also the caption to Fig. 4.

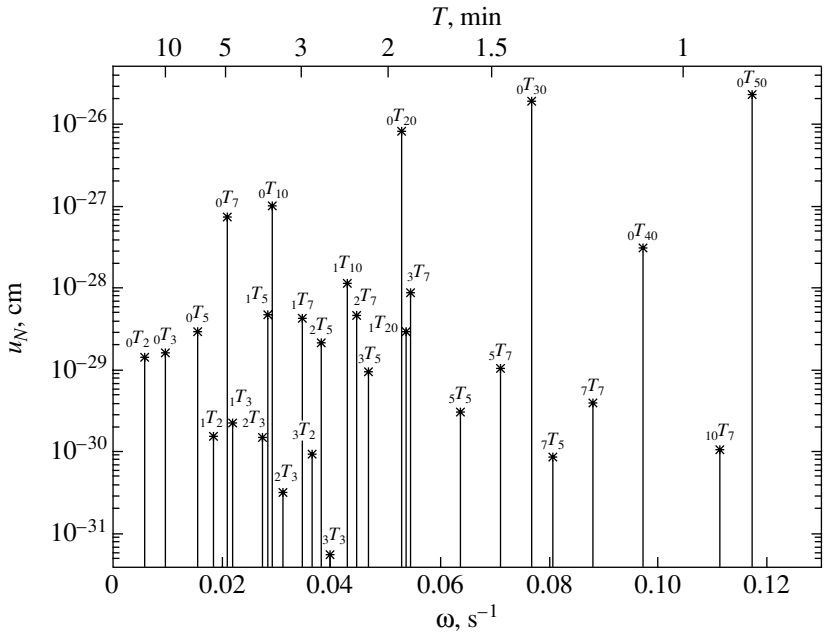

Fig. 6. The amplitude spectrum for the fundamental tones of torsional oscillations with $l = 2$, 3, 5, 7, 10, 20, 30, 40, and 50 and their first overtones. The frequency $\omega = 2\pi/T$ and period T (min) are along the x axis; the amplitude of displacements u_N (cm) is along the y axis. The seismic moment is set equal to 1. The focal mechanism is 45°, 45°, 45° for the dip, strike, and slip angles at a focal depth of 50 km. The epicenter coordinates are 29° N, 98° W; the seismometer coordinates are 0° N, 45° W; and the epicentral distance is 58°.

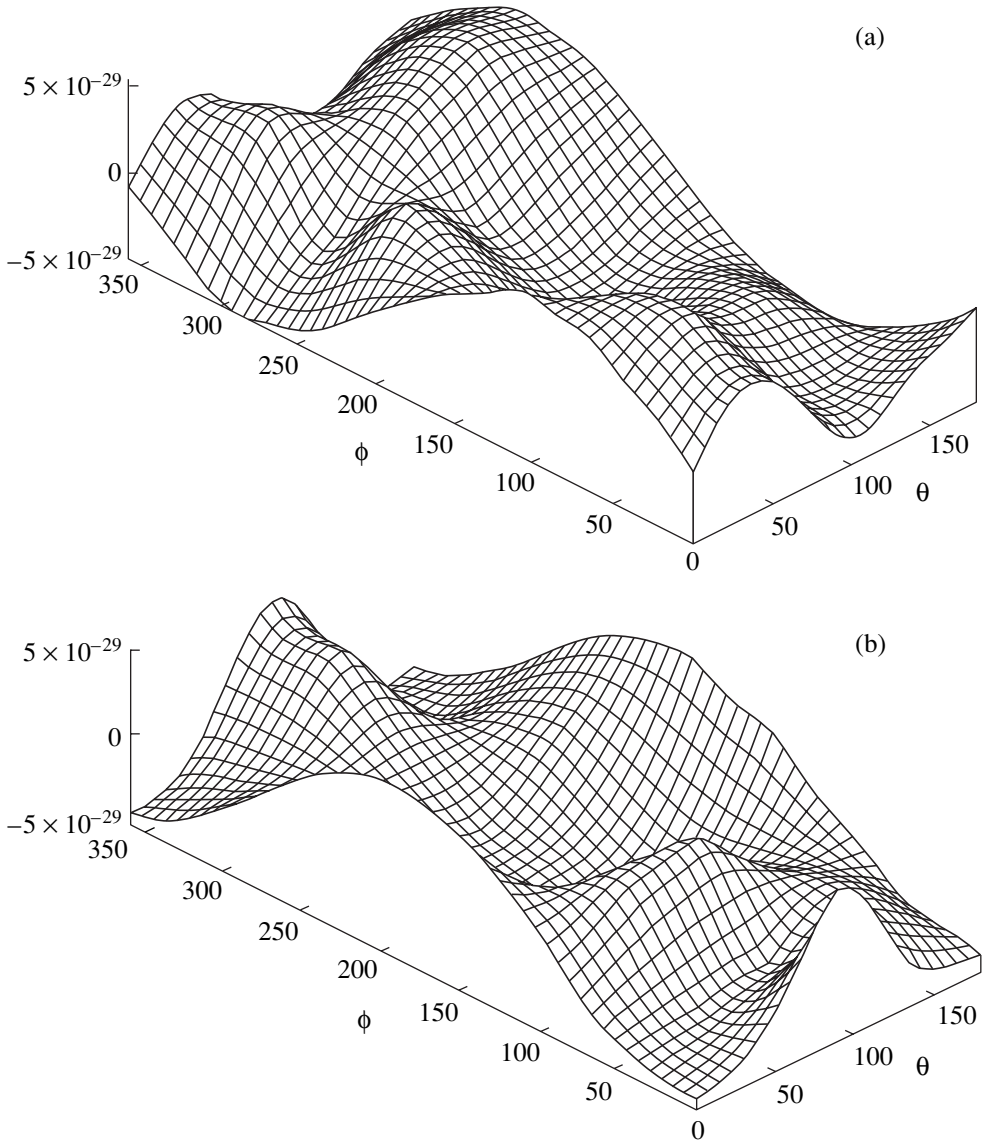

Fig. 7. The amplitude distribution of horizontal motion displacements u_N (a) and u_E (b) for the $l = 2$ fundamental mode of torsional oscillations. The longitude ϕ and polar distance θ are along the *x* and *y* axes, respectively. The seismic moment is set equal to 1. The focal mechanism is 45°, 45°, and 45° for the dip, strike, and slip angles at a focal depth of 50 km. The epicenter coordinates are 29° N, 98° W.

and 3d) also show the energy distributions for the fundamental modes with $l = 2, 3, 5, 10$ (the areas under the curves are normalized to unity).

The periods of torsional and spheroidal oscillations with $l = 2$–10 and their first ten overtones for the MNlc model are given in Tables 3 and 4.

The theory for the excitation of free oscillations was presented by Dziewonski and Woodhouse (1983). Based on their paper, it is easy to write out the corresponding formulas, which were used for our calculations. These formulas are given in the Appendix.

Judging by the available data on the Moon's seismic activity, one might expect torsional oscillations to be detected first. The horizontal displacement components u_N (northward) and u_E (eastward) are proportional to the seismic moment M_0 of the source. For the largest lithospheric moonquakes, $M_0 \approx (1–16) \times 10^{21}$ dyn. cm (see Table 2). Seismic events on the Moon have been recorded for five years. The possibility that larger moonquakes will also be detected in the future is not ruled out.

Currently available broadband seismometers can measure accelerations (Lognonne *et al.* 1996)

$$a_{N,E} = -\omega^2 u_{N,E} \approx 10^{-8} \text{ cm s}^{-2}. \quad (6)$$

Thus, the problem is to find the modes that satisfy condition (6) and to assess their diagnostic capabilities.

Figures 4 and 5 show the amplitudes of horizontal displacements u_N and u_E for the fundamental tones and overtones for two different focal mechanisms. We see

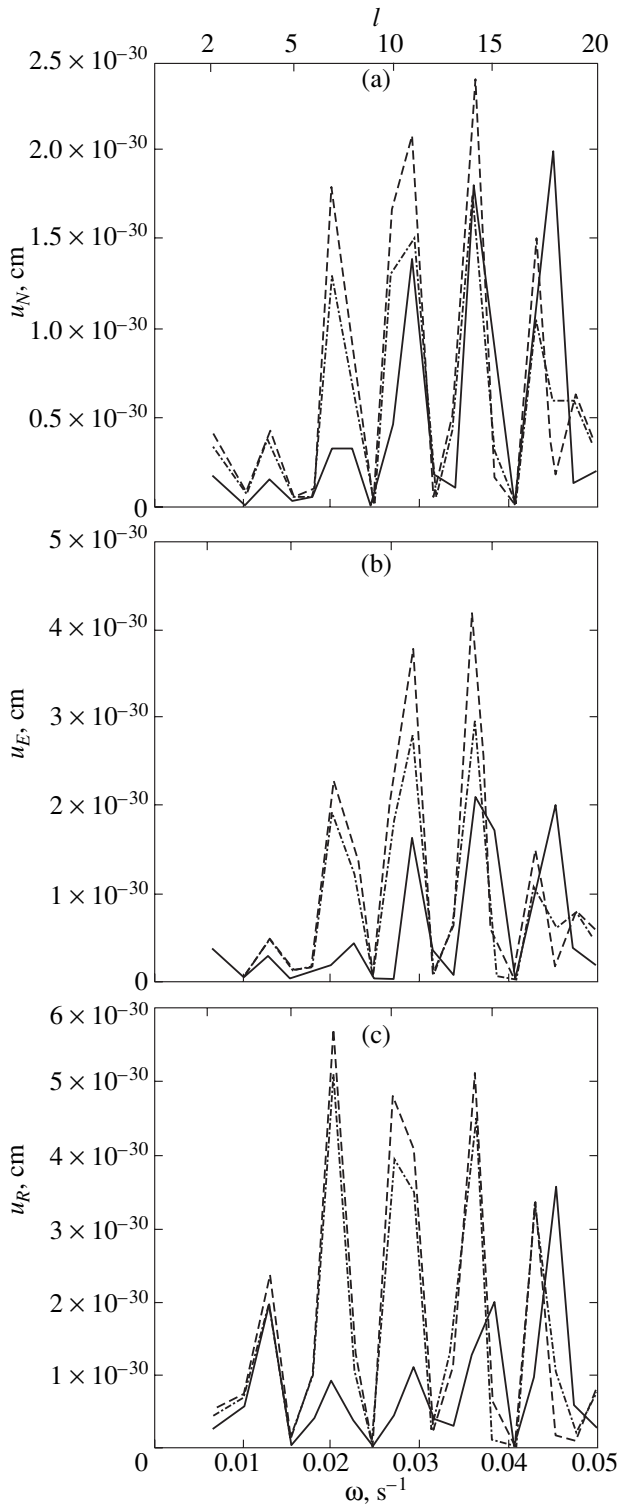

Fig. 8. The amplitudes of displacements u_N (a), u_E (b), and u_R (c) versus frequency $\omega = 2\pi/T$ and degree of oscillation l for the fundamental modes of spheroidal oscillations with l = 2–20. M_0 is set equal to 1. The focal mechanism is 45°, 45°, 45° for the dip, strike, and slip angles at focal depths of 50 km (solid lines), 150 km (dot-dashed lines), and 200 km (dashed lines). The epicenter coordinates are 29° N, 98° W; the seismometer coordinates are 0° N, 45° W; and the epicentral distance is 58°.

from Fig. 4 that the displacements of the torsional fundamental modes lie in the range 10^{-29}–10^{-26} cm for a unit seismic moment, which gives displacements of ~10^{-7}–10^{-4} for a lithospheric moonquake with M_0 = 10^{22} dyn. cm. A displacement of ~10^{-5} for $\omega \approx 0.03$ s^{-1} satisfies condition (6), and, consequently, the modes ${}_0T_l$ with l larger than 7–10 can be detected by currently available instruments. Turning to Fig. 3a, we see that

Table 5. The relative values of u_N and u_E normalized to the amplitude of mode ${}_0T_2$, 1.4×10^{-29}, for various focal depths. The focal mechanism is 45°, 45°, and 45° for the dip, strike and slip angles. The epicenter coordinates are 29° N, 98° W; the seismometer coordinates are 0° N, 45° W; and the epicentral distance is 58°

${}_nT_l$	T, min	50 km		150 km		200 km	
		u_N	u_E	u_N	u_E	u_N	u_E
${}_0T_2$	16.57	1.0	1.9	1.0	1.9	1.0	1.9
${}_1T_2$	5.669	0.1	0.2	0.2	0.3	0.2	0.4
${}_2T_2$	3.812	0.1	0.2	0.1	0.3	0.2	0.3
${}_3T_2$	2.867	0.1	0.2	0.2	0.3	0.2	0.3
${}_0T_3$	10.79	–1.2	0.6	–1.2	0.6	–1.2	0.6
${}_1T_3$	4.792	–0.2	0.2	–0.1	0.2	–0.1	0.2
${}_2T_3$	3.365	–0.02	0.04	0.003	0.05	0.02	0.05
${}_3T_3$	2.63	–0.004	0.02	0.007	0.02	0.01	0.02
${}_0T_5$	6.717	–2.1	–1.0	–2.1	–1.6	–2.0	–1.6
${}_1T_5$	3.704	–3.8	–3.3	–2.7	–2.7	–1.9	–2.3
${}_2T_5$	2.747	–1.4	–1.3	–0.6	–0.9	–0.1	–0.5
${}_3T_5$	2.235	–0.7	–0.7	–0.2	–3.9	0.2	–1.2
${}_0T_7$	4.970	45	26	41	24	39	23
${}_1T_7$	3.049	2.9	1.8	1.6	1.1	0.7	0.7
${}_2T_7$	2.347	3.5	2.4	0.7	0.9	–1.1	–0.05
${}_3T_7$	1.956	2.3	1.6	–0.4	0.3	–1.8	–0.6
${}_0T_{10}$	3.62	–79	–47	–69	–41	–64	–37
${}_0T_{20}$	1.951	586	407	379	264	300	207
${}_0T_{30}$	1.372	–1429	–1000	–621	–450	–407	–293
${}_0T_{40}$	1.076	22	17	6.4	4.8	3.4	2.5
${}_0T_{50}$	0.894	1571	1071	286	186	121	79

the torsional modes ${}_0T_l$ with $l \geq 7$ can sound the Moon's outer shells, including the transition zone.

As we see from Fig. 5, the displacement amplitude for the overtones is smaller than that for the fundamental modes. Therefore, the overtones with $l \leq 7$–10 do not satisfy condition (6).

The amplitude spectrum for the fundamental modes ${}_0T_l$ and their first overtones are shown in Fig. 6. We see that when M_0 increases to 10^{23} dyn. cm or when the seismometer sensitivity increases to $a \approx 10^{-9}$ cm s^{-2} [see (6)], the first overtones of torsional oscillations with $l \geq 5$ can be detected.

Figure 7 shows the pattern of ground displacements for the mode ${}_0T_2$. The distribution of oscillation amplitudes is seen to depend on the relative positions of the source and the receiver. For some epicentral distances, the receiver can be located in the nodal zone.

Since the actual mechanism of lithospheric moonquakes is not known with certainty, we calculated the oscillation amplitudes for various combinations of strike, dip, and slip angles at 45° intervals. The calculations show that the amplitudes for different focal mechanisms differ by several times. The minimum and maximum displacements u_N (in cm) at $M_0 = 1$ dyn. cm for several modes ${}_0T_l$ are as follows: $l = 2$: 1×10^{-29}–6×10^{-29}; $l = 3$: 1.5×10^{-29}–6×10^{-29}; $l = 5$: 1.2×10^{-29}–4.5×10^{-29}; $l = 7$: 3×10^{-28}–8×10^{-28}; $l = 10$: 7×10^{-28}–1×10^{-27}; and $l = 20$: 2×10^{-27}–1×10^{-26}.

The displacements for the spheroidal modes ${}_0S_l$ with $l = 2$–20 are shown in Fig. 8. We see that a moonquake with the seismic moment $M_0 = 10^{25}$ dyn. cm is required for them to be detected.

The relative values of ground displacement components u_N and u_E for a source at depths of 50, 150, and 200 km are given in Table 5. The focal mechanism is 45°, 45°, and 45° for the strike, dip, and slip angles. The epicenter of the event has the coordinates of a strong shallow moonquake, 29° N and 98° W; the seismometer was placed at the point with coordinates 0° N, 45° W near the Apollo seismic station network. The displacements are normalized with respect to the component u_N of mode ${}_0T_2$; the source is at a depth of 50 km. The amplitude u_N of oscillation mode ${}_0T_2$ is 1.4×10^{-29} cm at $M_0 = 1$ dyn. cm. The amplitudes of components u_N and u_E increase with l, and the displacements of the overtones are smaller than those of the fundamental modes. The amplitudes of the fundamental oscillation modes decrease with increasing depth of the source, which is noticeable for the modes with l larger than 5.

CONCLUSION

A spherically symmetric model of the Moon's interior structure is difficult to construct using only body-wave seismic data, because its outer shells are highly inhomogeneous.

Accordingly, it seemed reasonable to study the diagnostic capabilities of the free-oscillation method to construct an averaged model of the Moon's internal structure. For this purpose, using the free-oscillation excitation theory for the Earth (Dziewonski and Woodhouse 1983), we derived formulas for the ground displacement components as functions of the moonquake focal mechanism (see the Appendix). It turned out that the strongest lithospheric moonquakes with a seismic moment $M_0 \approx 10^{22}$ dyn. cm are capable of exciting the torsional modes ${}_0T_l$ with $l \geq 7$, which can be detected by currently available high-sensitivity broadband instruments. These modes are capable of sounding the Moon's outer layers to a depth of ≈500 km, given that the Moon's inhomogeneities extend approximately to this depth (physically, this can be related to the depth of the "magma ocean" that appeared during the lunar formation, whose solidification led to this deep inhomogeneous layer of the satellite).

We have shown that the largest lithospheric moonquakes excite spheroidal modes ${}_nS_l$ much worse. These modes cannot be detected by available instruments because of the Moon's low seismic activity. Modes ${}_nS_l$ are excited by meteoritic impacts on the lunar surface much more effectively. However, the impacts on the lunar surface detected so far are too weak to excite free oscillations that could be recorded.

Briefly, as our general conclusion, we can say that recording the spectrum of torsional modes ${}_nT_l$ would allow noticeable progress to be made in constructing a global model of the Moon's interior structure.

ACKNOWLEDGMENTS

This study was supported by the Russian Foundation for Basic Research, project no. 99-02-16013.

APPENDIX

Following Dziewonski and Woodhouse (1983), let us derive the formulas that were used in our calculations. The source is assumed to be pointlike and instant. The components of displacement vector $\mathbf{s}_i$ for torsional and spheroidal oscillations are given by formulas (1) and (2); the radial functions are normalized as follows:

$$\omega_k^2 \int_0^R \rho(r)[{}_nW_l(r)]^2 r^2 dr = 1, \quad \text{(A.1)}$$

$$\omega_k^2 \int_0^R \rho(r)([{}_nU_l(r)]^2 + [{}_nV_l(r)]^2) r^2 dr = 1. \quad \text{(A.2)}$$

An arbitrary mode k is defined by four numbers (l, m, n, q), where q specifies the type of oscillation, torsional or spheroidal.

In general form, the displacement on the satellite's surface for the kth mode is

$$\mathbf{u}(\mathbf{x}, t) = h_k(t - t_s)]M_{ij}\bar{e}_{ij}^{(k)}(\mathbf{x}_s)\mathbf{s}_k(\mathbf{x}), \quad \text{(A.3)}$$

where $h_k(t - t_s) = 1 - \exp[-\alpha_k(t - t_s)]\cos\omega_k(t - t_s)$; (t_s, x_s) is the time of the source and its coordinates; M_{ij} is the seismic moment tensor, a force characteristic of the source; $e_{ij}^{(k)}(\mathbf{x}_s)$ is the strain tensor in the source; $\alpha_k = \omega_k/2Q_k$ are the decay coefficients of the kth mode; and Q_k are corresponding dissipative functions. The summation is performed over repeated indices the bar denotes conjugation.

To simplify the mathematics, we pass to the epicentral coordinate system, in which the source is located at the pole ($\theta = 0$). Substituting expression (1) and (2) for the displacement vector for torsional and spheroidal oscillations, respectively, in the strain tensor $e_{ij}^{(k)}$ written in spherical coordinates, we obtain

	Torsional modes			Spheroidal modes		
	$m = 0$	$m = \pm1$	$m = \pm2$	$m = 0$	$m = \pm1$	$m = \pm2$
$\bar{e}_{rr}$	0	0	0	$k_0\dot{U}$	0	0
$\bar{e}_{\theta\theta}$	0	0	$\mp ik_2 r^{-1}W$	$\frac{1}{2}k_0F$	0	$k_2r^{-1}V$
$\bar{e}_{\phi\phi}$	0	0	$\pm ik_2r^{-1}W$	$\frac{1}{2}k_0F$	0	$-k_2r^{-1}V$
$\overline{2e}_{r\theta}$	0	$\pm ik_1E_T$	0	0	$-k_1E_S$	0
$\overline{2e}_{r\phi}$	0	k_1E_T	0	0	$\pm ik_1E_S$	0
$\overline{2e}_{\theta\phi}$	0	0	$-2k_2r^{-1}W$	0	0	$\mp 2k_2 r^{-1}V$

where $k_n = \frac{1}{2^n}\left(\frac{2l+1}{4\pi}\frac{(l+n)!}{(l-n)!}\right)^{1/2}$, $E_T = \dot{W} - r^{-1}W$, $E_S = \dot{V} - r^{-1}(V - U)$, and $F = r^{-1}[2U - l(l+1)V]$; the dot denotes differentiation with respect to the radius. The values of U, V, and W are taken at $r = x_s$.

A moonquake is modeled by a fault in a continuum for which the fault edges b are displaced over area S. The quantity $M_0 = \mu bS$ is called the seismic moment, where μ is the shear modulus in the source region. In general, the force model of a source is described by the seismic moment tensor M_{ij}. The notation of the M_{ij} components and their dependence on dip δ, strike ϕ, and slip α angles are given by the formulas

$$\begin{aligned} f_1 &= M_{rr} = M_0 \sin 2\delta \sin\alpha, \\ f_2 &= M_{\theta\theta} \\ &= M_0(\sin 2\delta \sin\alpha \sin^2\phi + \cos\alpha \sin\delta \sin 2\phi), \\ f_3 &= M_{\phi\phi} \\ &= M_0(-\sin 2\delta \sin\alpha \cos^2\phi + \cos\alpha \sin\delta \sin 2\phi), \\ f_4 &= M_{r\theta} \\ &= M_0(-\cos 2\delta \sin\alpha \sin\phi - \cos\alpha \cos\delta \cos\phi), \\ f_5 &= M_{r\phi} \\ &= M_0(-\cos 2\delta \sin\alpha \cos\phi + \cos\alpha \cos\delta \sin\phi), \\ f_6 &= M_{\theta\phi} \\ &= M_0(-\sin\delta \cos\alpha \cos 2\phi - 1/2 \sin\alpha \sin 2\delta \sin 2\phi). \end{aligned} \tag{A.5}$$

The dip δ, strike ϕ, and slip α angles are shown in Fig. A1.

We can get a general idea of the signal if we choose these angles to be 45, 45, and 45 and set M_0 equal to unity. We then have $f_1 = \sqrt{2}/2$, $f_2 = -(2 + \sqrt{2})/4$, $f_3 = (2 - \sqrt{2})/4$, $f_4 = -\sqrt{2}/4$, $f_5 = \sqrt{2}/4$, $f_6 = -\sqrt{2}/4$, and $f_1 + f_2 + f_3 = 0$. A shift in the strike is characterized by $\delta = 90$, $\phi = 90$, and $\alpha = 0$. In that case, we have $f_1 = 0$, $f_2 = 0$, $f_3 = 0$, $f_4 = 0$, $f_5 = 0$, $f_6 = 1$, and $f_1 + f_2 + f_3 = 0$.

Substituting (1), (2), (3), (A.4), and (A.5) in (A.3) and summing over repeated indices, we derive the following expressions for the displacement components on the satellite's surface in epicentral coordinates, because the multiplets with $m = 0, \pm 1, \pm 2$ are degenerate (see A.4):

$$\begin{aligned} &u_\theta(a, \theta, \phi, t) \\ &= (-2k_1 E_T(r_s) W(a) \operatorname{cosec}\theta X_l^1(\theta)(f_4 \cos\phi + f_5 \sin\phi) \\ &\quad + 4k_2 r_s^{-1} W(r_s) W(a) \operatorname{cosec}\theta X_l^2(\theta) \\ &\quad \times [(f_2 - f_3)\cos 2\phi + 2f_6 \sin 2\phi])h_k(t - t_s), \end{aligned} \tag{A.6}$$

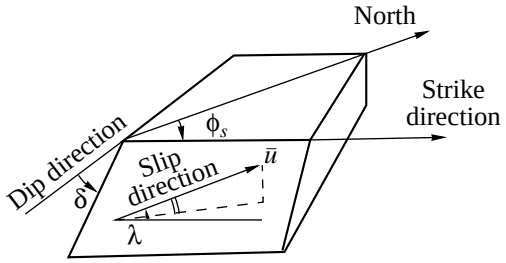

Fig. A1. The parameters that characterize the orientation of the fault plane (strike ϕ_s, dip δ) and the slip direction. The angle ϕ_s is measured clockwise from the northward direction, the dip of the fault plane is to the right from the strike direction ($0 \le \phi_s < 2\pi$), and δ is measured downward from the horizontal plane ($0 \le \delta < \pi/2$).

$$\begin{aligned} &u_\phi(a, \theta, \phi, t) \\ &= (2k_1 E_T(r_s) W(a) X_l^1(\theta)(f_4 \sin\phi - f_5 \cos\phi) \\ &\quad - 2k_2 r_s^{-1} W(r_s) W(a) \partial_\theta X_l^2(\theta) \\ &\quad \times [(f_2 - f_3)\sin 2\phi - 2f_6 \cos 2\phi])h_k(t - t_s) \end{aligned} \tag{A.7}$$

for torsional oscillations and

$$\begin{aligned} u_r(a, \theta, \phi, t) &= \left(k_0\left[f_1 \dot{U} + \frac{1}{2}(f_2 + f_3)F\right]U(a)X_l^0(\theta)\right. \\ &\quad - 2k_1 E_S(x_s)(f_4 \cos\phi + f_5 \sin\phi)U(a)X_l^1(\theta) \\ &\quad + 2k_2 r_s^{-1} V(r_s)[(f_2 - f_3)\cos 2\phi \\ &\quad \left. + 2f_6 \sin 2\phi]U(a)X_l^2(\theta)\right)h_k(t - t_s), \end{aligned} \tag{A.8}$$

$$\begin{aligned} u_\theta(a, \theta, \phi, t) &= \left(k_0\left[f_1 \dot{U} + \frac{1}{2}(f_2 + f_3)F\right]V(a)\partial_\theta X_l^0(\theta)\right. \\ &\quad - 2k_1 E_S(x_s)(f_4 \cos\phi + f_5 \sin\phi)V(a)\partial_\theta X_l^1(\theta) \\ &\quad + 2k_2 r_s^{-1} V(r_s)[(f_2 - f_3)\cos 2\phi \\ &\quad \left. + 2f_6 \sin 2\phi]V(a)\partial_\theta X_l^2(\theta)\right)h_k(t - t_s), \end{aligned} \tag{A.9}$$

$$\begin{aligned} &u_\phi(a, \theta, \phi, t) \\ &= (2k_1 E_S(x_s)[f_4 \sin\phi - f_5 \cos\phi]V(a)X_l^1(\theta) \\ &\quad - 4k_2 r_s^{-1} V(r_s)[(f_2 - f_3)\sin 2\phi - 2f_6 \cos 2\phi] \\ &\quad \times V(a)X_l^2(\theta))h_k(t - t_s) \end{aligned} \tag{A.10}$$

for spheroidal oscillations.

The seismographs record the directions of upward, northward, and eastward displacements. We pass to the geographical coordinate system by using the formulas

$$u_N = -u_\theta \cos\psi - u_\phi \sin\psi,$$
$$u_E = -u_\theta \sin\psi + u_\phi \cos\psi, \quad \text{(A.11)}$$

where the subscripts N and E refer to the northward and eastward components and ψ is the source's azimuth with respect to the receiver. The azimuth is the angle between the arc of the great circle passing through the pole and the source and the arc of the great circle connecting the receiver and the source.

$$\cos\psi = \mathrm{cosec}\theta[\sin\theta_r \cos\theta_s$$
$$- \cos\theta_r \sin\theta_s \cos(\phi_s - \phi_r)], \quad \text{(A.12)}$$
$$\sin\psi = \mathrm{cosec}\theta \sin\theta_s \sin(\phi_s - \phi_r),$$

where the source's coordinates are (r_s, θ_s, ϕ_s), the receiver's coordinates are (a, θ_r, ϕ_r), and θ is the epicentral distance. Here, we estimated the displacements u_N and u_E for different moonquake focal mechanisms.

REFERENCES

1. Z. Alterman, H. Jarosch, and C. L. Pekeris, Proc. R. Soc. London, Ser. A **259**, 80 (1959).
2. B. G. Bills and A. J. Ferrari, J. Geophys. Res. **82**, 1306 (1977).
3. A. B. Binder and J. Oberst, Earth Planet. Sci. Lett. **74**, 149 (1985).
4. B. A. Bolt and J. S. Derr, Vistas Astron. **11**, 69 (1969).
5. R. E. Carr and R. L. Kovach, Icarus **1**, 75 (1962).
6. H. Chenet, Ph. Lognonné, J. Gagnepain-Beyneix, and L. P. Vinnik, in *Proceedings of the 25th General Assembly of the European Geophysical Society*, ISSN:1029-7006, 2000, Vol. 2.
7. A. M. Dainty, M. N. Toksoz, K. R. Anderson, *et al.*, Moon **9**, 11 (1974).
8. J. S. Derr, Phys. Earth Planet. Inter. **2**, 61 (1969).
9. A. M. Dziewonski and J. H. Woodhouse, in *Proceedings of the International School of Physics "Enrico Fermi," 1983*, Vol. 85, p. 45.
10. N. R. Goins, *Lunar Seismology: The Internal Structure of the Moon*, *Ph.D. Thesis* (Massachusetts Inst. of Technology, Cambridge, 1978).
11. N. R. Goins, A. M. Dainty, and M. N. Toksoz, J. Geophys. Res. **86**, 378 (1981a).
12. N. R. Goins, A. M. Dainty, and M. N. Toksoz, J. Geophys. Res. **86**, 5061 (1981b).
13. T. V. Gudkova and V. N. Zharkov, Planet. Space Sci. **44**, 1223 (1996a).
14. T. V. Gudkova and V. N. Zharkov, Planet. Space Sci. **44**, 1231 (1996b).
15. T. V. Gudkova and V. N. Zharkov, Astron. Vestn. **34**, 506 (2000).
16. L. L. Hood and M. T. Zuber, in *Origin of the Earth and Moon*, Ed. by R. M. Canup and K. Righter (Univ. Arizona Press, Tucson, 2000), p. 397.
17. L. L. Hood, D. L. Mitchell, R. P. Lin, *et al.*, Geophys. Res. Lett. **26**, 2327 (1999).
18. A. Khan, K. Moseggard, and K. L. Rasmussen, Geophys. Res. Lett. **27**, 1591 (2000).
19. A. S. Konopliv, A. Binder, L. Hood, *et al.*, Science **281**, 1476 (1998).
20. D. R. Lammlein, G. V. Latham, J. Dorman, *et al.*, Rev. Geophys. Space Phys. **12**, 1 (1974).
21. G. V. Latham, M. Ewing, J. Dorman, *et al.*, Moon **7**, 396 (1973).
22. F. G. R. Lemoine, D. E. Smith, M. T. Zuber, *et al.*, J. Geophys. Res. **102**, 16 339 (1997).
23. Ph. Lognonné and B. Mosser, Surv. Geophys. **14**, 239 (1993).
24. Ph. Lognonné, J. G. Beyneix, W. B. Banerdt, *et al.*, Planet. Space Sci. **44**, 1237 (1996).
25. H. J. Melosh, *Impact Cratering: A Geologic Process* (Oxford Univ. Press, Oxford, 1989), Oxford Monographs on Geology and Geophysics, No. 11.
26. Y. Nakamura, J. Geophys. Res. **88**, 677 (1983).
27. Y. Nakamura, G. Latham, D. Lammlein, *et al.*, Geophys. Res. Lett. **1**, 137 (1974).
28. Y. Nakamura, G. V. Latham, H. J. Dorman, *et al.*, in *Proceedings of the 10th Lunar and Planetary Science Conference, Houston, 1979* (Pergamon, New York, 1979), Vol. 3, p. 2299.
29. J. Oberst, J. Geophys. Res. **92**, 1397 (1987).
30. D. E. Smith, M. T. Zuber, G. A. Neumann, and F. G. Lamoine, J. Geophys. Res. **102**, 1591 (1997).
31. H. Takeuchi, M. Saitov, and N. Kobayashi, J. Geophys. Res. **66**, 3895 (1961).
32. M. N. Toksoz, Rev. Geophys. Space Phys. **13**, 306 (1975).
33. M. N. Toksoz, A. M. Dainty, S. C. Solomon, and K. R. Anderson, Rev. Geophys. Space Phys. **12**, 539 (1974).
34. V. N. Zharkov, *Interior Structure of the Earth and Planets* (Harwood Academic Publ., Chur, 1986).
35. V. N. Zharkov, V. A. Pan'kov, A. A. Kalachnikov, and A. I. Osnach, *An Introduction to the Physics of the Moon* (Nauka, Moscow, 1969).

Translated by T. Gudkova

Astronomy Letters, Vol. 27, No. 10, 2001, pp. 671–677. Translated from Pis'ma v Astronomicheskiĭ Zhurnal, Vol. 27, No. 10, 2001, pp. 788–794.

Orbital Evolution of Jupiter's New Outer Satellites

M. A. Vashkov'yak*

Keldysh Institute of Applied Mathematics, Russian Academy of Sciences, Miusskaya pl. 4, Moscow, 125047 Russia

Received April 9, 2001

Abstract—Data on recently discovered outer satellites of Jupiter are used to analyze their long-period orbital evolution. We determine the extreme eccentricities and inclinations, as well as the circulation periods of the pericenter arguments and of the longitudes of the ascending nodes. The satellite orbital elements are plotted against time. The methods of analysis are identical to those that we used to analyze the orbital evolution of Uranus's and Saturn's new outer satellites. *© 2001 MAIK "Nauka/Interperiodica".*

Key words: *Jupiter's outer satellites, orbital evolution*

1. INTRODUCTION. INPUT DATA

Reports on a new celestial object and on its identification as an outer satellite of Jupiter appeared in the middle of 2000 (Marsden 2000a, 2000b). It was discovered through the joint efforts of many scientists: J.V. Scotti, T.B. Spahr, R.S. McMillan, J.A. Larsen, J. Montani, A.E. Gleason, T. Gehrels, B.G. Marsden, G.V. Williams, and B. Gladman. The new satellite was tentatively designated as S/1999 J1, because it was identified with the object 1999 UX18 discovered in 1999.

In November 2000, S.S. Sheppard, D.C. Jevitt, Y. Fernandez, and G. Magnier reported the discovery of yet another satellite of Jupiter, which was tentatively designated as S/2000 J1. However, based on B.G. Marsden's calculations and on M. Holman's observations, it was identified with the well-known satellite S/1975 J1, which was previously discovered by C.T. Koval and E. Roemer. This identity was confirmed by G.V. Williams's numerical calculations (Marsden 2000c). Subsequently, he refined the orbits of S/1999 J1 and S/2000 J1 (Marsden 2000d).

The short period from late 1999 until early 2000 was marked by the discovery of ten new satellites of Jupiter, S/2000 J2, J3, …, J11. They were discovered by a group of scientists: S.S. Sheppard, D.S. Jevitt, Y.R. Fernandez, G. Magnier, S. Dahm, and A. Evans. The orbital elements of all these satellites were obtained by Marsden (2001a, 2001b).

Table 1 gives the orbital elements of Jupiter's new outer satellites required to analyze the orbital evolution. They were taken from the Internet source at http://cfa-www.harvard.edu/iau/mpc.html with Circular numbers MPEC 2001-A28 and A29. The semimajor axis a is given in astronomical units, and the angular Keplerian elements in the standard notation i, ω, and Ω (in degrees) refer to the ecliptic and equinox 2000.0. For all twelve satellites, the initial epoch t_0 is the same, 2001 Apr. 1.0 TT = JDT 2 452 000.5.

Below, we also give numerical values of the constant parameters that characterize the Sun–Jupiter system and that we adopted in this paper:

μ = 126 712 840 km^3 s^{-2} is Jupiter's gravitational constant;

a_0 = 73 398 km is Jupiter's mean equatorial radius;

c_{20} = –0.014736 is the coefficient of the second zonal harmonic of its attractive potential;

μ' = 132 712 442 007 km^3 s^{-2} is the solar gravitational constant;

a' = 778 357 700 km is Jupiter's orbital semimajor axis;

i' = 1.°3064 is Jupiter's orbital inclination at initial epoch t_0;

Ω' = 99.°865 is the longitude of the ascending node of Jupiter's orbit at initial epoch t_0.

2. EVOLUTION OF THE NEW SATELLITE ORBITS

2.1. Peculiarities of Jupiter's Satellite System

The discoveries in 1999 and 2000 have significantly extended our knowledge of Jupiter's satellite system and its structure. The new satellites S/2000 J1 and S/2000 J11 were included in group I of the outer satellites with direct motions, while S/1999 J1 ≡ S/1975 J1, S/2000 J2, J3, …, J10 were included in group II with retrograde motions.

Peculiarities of the orbital dynamics for Jupiter's previously discovered satellites have been described in many papers [see, e.g., the special monograph by Ferraz-Mello (1983) and the review by Ural'skaya (1991)].

* E-mail address for contacts: vashkov@spp.keldysh.ru

Table 1. Orbital elements for Jupiter's new outer satellites

Satellite	*a*, AU	*e*	*i*, deg	ω, deg	Ω, deg
S/1999 J1	0.1570775	0.2061509	143.48974	56.96157	282.84304
S/2000 J1	0.0494535	0.2055437	45.37763	238.85643	202.12202
S/2000 J2	0.1613366	0.3177403	165.79188	230.49170	39.08737
S/2000 J3	0.1379890	0.2686209	149.90562	84.21828	270.98971
S/2000 J4	0.1461769	0.3464728	160.90878	354.28364	321.58017
S/2000 J5	0.1398263	0.2002700	149.28845	106.36579	36.29295
S/2000 J6	0.1524400	0.2809114	165.03895	139.97510	144.83367
S/2000 J7	0.1410321	0.1458198	146.35342	202.60056	284.99206
S/2000 J8	0.1566806	0.5277172	151.69961	303.66947	302.58327
S/2000 J9	0.1448674	0.2460425	163.54516	269.83625	314.16830
S/2000 J10	0.1356935	0.1553197	165.62039	172.52190	155.62290
S/2000 J11	0.0843796	0.2152076	28.55170	178.01785	290.87294

The main perturbations in the motion of Jupiter's inner satellites are attributable to its oblateness. In addition, the Galilean satellites are subjected to appreciable mutual attraction, which is enhanced by the resonant nature of their motion. For the outer satellites, the main perturbing factor is solar attraction.

A convenient characteristic of the satellite system of any planet, including Jupiter, is the dependence of the following parameter on the satellite orbital semimajor axis:

$$\gamma = -\frac{\mu a_0^2 c_{20} a'^3}{\mu' a^5}. \quad (1)$$

This parameter is the ratio of the perturbing accelerations from planetary oblateness and from solar attraction. For Jupiter's satellite system, dependence (1) is shown in Fig. 1 (solid curve) on a logarithmic scale. The heavy segments on the horizontal axis correspond to the ranges of orbital semimajor axes for the inner, Galilean, and outer satellites. The number of satellites within a given range (except for the large number of particles that form Jupiter's ring) is indicated above each of these segments. A characteristic feature of Jupiter's satellite system is the existence of two "empty" segments, which are free from satellites (except for S/2000 J1):

$$2 \times 10^6 \text{ km} \le a \le 11 \times 10^6 \text{ km},$$

$$12.6 \times 10^6 \text{ km} \le a \le 20 \times 10^6 \text{ km}.$$

The first of these segments separates the inner and Galilean satellites from the outer satellites, while the second segment separates the two groups of outer satellites with direct and retrograde motions.

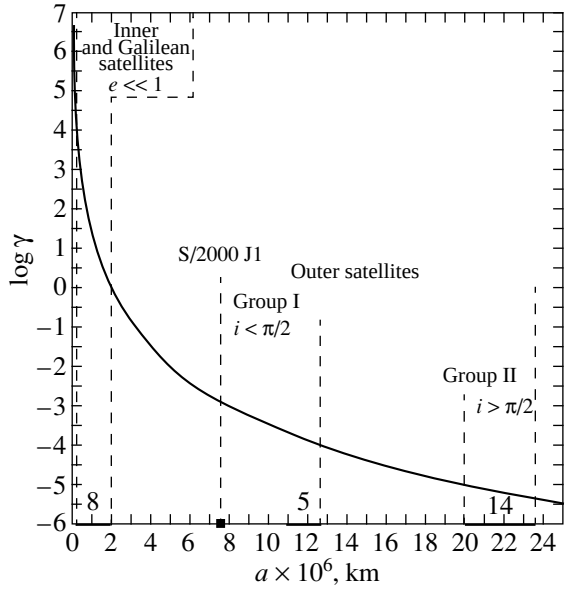

Fig. 1. Logarithmic dependence of γ on *a* for Jupiter's satellite system.

Small γ correspond to the satellite orbits that experience the dominant influence of solar perturbations. For the outer satellites of group II, this parameter varies over the range

$$0.5 \times 10^{-5} \le \gamma \le 10^{-5}.$$

For the outer satellites of group I, it takes on values in the range $10^{-4} \le \gamma \le 2 \times 10^{-4}$, except for the "intermediate" satellite S/2000 J1 with $\gamma \approx 1.5 \times 10^{-3}$.

It is of interest to compare the orbital structures of Jupiter's, Saturn's, and Uranus's outer satellites. Whereas the outer satellites in Jupiter's system clearly break up into two groups (by inclinations and semimajor axes), in Saturn's system of outer satellites, there is a large range of semimajor axes in which both direct and retrograde orbits exist. In contrast, all the outer satellites in Uranus's system discovered to date possess retrograde motions.

In this paper, to analyze the long-period orbital evolution, we disregard the influence of Jupiter's oblateness on the orbital evolution of its new outer satellites and, setting γ = 0, use Hill's double-averaged problem

Table 2. Parameters of the evolving orbits for Jupiter's outer satellites

Satellite	c_1	c_2	$e_{\min}$	$e_{\max}$	$\tilde{i}_{\min}$, deg	$\tilde{i}_{\max}$, deg	$T_{\tilde{\omega}}$, year	$T_{\tilde{\Omega}}$, year
S/1999 J1	0.6393	0.0070	0.133	0.276	143.8	146.3	85	98
S/2000 J1	0.4677	0.0017	0.065	0.479	38.8	46.7	771	540
S/2000 J2	0.8397	0.0359	0.300	0.325	163.8	165.7	45	77
S/2000 J3	0.7124	0.0123	0.175	0.270	149.0	151.2	80	113
S/2000 J4	0.7947	0.0480	0.346	0.381	161.9	164.6	51	84
S/2000 J5	0.7006	0.0063	0.126	0.216	147.5	149.0	90	119
S/2000 J6	0.8519	0.0288	0.268	0.294	163.4	164.9	50	86
S/2000 J7	0.6986	0.0076	0.138	0.234	147.6	149.3	86	115
S/2000 J8	0.5718	0.0724	0.426	0.559	146.7	155.8	48	65
S/2000 J9	0.8733	0.0200	0.223	0.246	163.5	164.6	55	98
S/2000 J10	0.9092	0.0096	0.155	0.169	164.8	165.3	62	114
S/2000 J11	0.7176	0.0185	0.215	0.309	27.0	29.8	154	225

(Lidov 1961, 1963). This problem has already been used to analyze the orbital evolution of Uranus's and Saturn's new satellites (Vashkov'yak 1999, 2001).

The perturbing function of this integrable problem includes only the terms $\sim(a/a')^2$ averaged over the mean anomalies of the satellite and the perturbing body (Sun). In addition, Jupiter's orbital eccentricity e' (the actual value is ~0.05) and orbital inclination to the ecliptic plane i' (the actual value is $\sim 1\overset{\circ}{.}3$) are assumed to be zero.

To check and refine the analytic solution of the averaged problem, we numerically integrate the fuller evolutional system that includes both secular terms $\sim(a/a')^2\sin i'$, $\sim(a/a')^3 e'$ and the time variability of Jupiter's orbital elements, according to the Lagrange–Brower–Wurkom theory.

2.2. Quantitative Evolution Characteristics

The pattern of the evolution of a satellite orbit in Hill's double-averaged problem is determined by numerical values of its first integrals (Lidov 1961):

$$a = c_0, \quad (1-e^2)\cos^2\tilde{i} = c_1,$$
$$e^2(2/5 - \sin^2\tilde{i}\sin^2\tilde{\omega}) = c_2. \qquad (2)$$

In contrast to i and ω, the angular variables $\tilde{i}$ and $\tilde{\omega}$ are related to the orbital plane of a perturbing body whose position relative to the ecliptic is defined by the elements i' and Ω'.

Table 2 gives the constants c_1 and c_2, the ranges of e and $\tilde{i}$, as well as the circulation periods of $\tilde{\omega}$ and $\tilde{\Omega}$. Our calculations show that $c_2 > 0$ for all the above satellites; i.e., the pericenter arguments of their orbits execute circulation motion. The longitudes of the ascending nodes also monotonically change with time. However, whereas $\tilde{\omega}$ monotonically increases for all satellite orbits, $\tilde{\Omega}$ increases only for the satellites of group II with retrograde motions ($\cos\tilde{i} < 0$). For two satellites of group I, the node longitude decreases.

The data in Table 2 indicate that S/2000 J1 differs markedly from the remaining satellites in the parameters of its orbital evolution. First, note that c_1 and c_2 are at a minimum for its orbit, with c_1 being $0.4677 < 0.6$. This determines the existence of two qualitatively different regions ($\tilde{\omega}$, circulation at $c_2 > 0$ and $\tilde{\omega}$ libration at $c_2 < 0$) and their separatrix, which corresponds to $c_2 = 0$ in the $(\tilde{\omega}, e)$ plane. Although this constant is positive, $c_2 = 0.0017 > 0$, it is nearly zero. As a result, the amplitude of the eccentricity oscillations ($e_{\max} - e_{\min} \approx 0.4$) is large, the largest among all the above orbits, and $e_{\max} \approx 0.479$ is close to

$$e_s = \sqrt{1 - \frac{5c_1}{3}} = 0.470,$$

which corresponds to the maximum of e on the separatrix.

Notes: (1) Numerical integration of the fuller averaged system (see the Introduction) shows that, although c_2 is nearly zero, the $\tilde{\omega}$ variation for the S/2000 J1 orbit also remains circulation on a long time scale of 50 000 years (the evolution period of Jupiter's orbital elements).

(2) In general, the possible refinement of the orbital elements for S/2000 J1 in the future can change c_2 only slightly by making it negative. In that case, the $\tilde{\omega}$ variation for this orbit will be libration.

The oscillation amplitude of the orbital inclination for S/2000 J1 is also close to the maximum among all the above orbits, ~8°. However, this particular orbit is distinguished from the remaining orbits by its relatively large circulation periods of $\tilde{\omega}$ and $\tilde{\Omega}$, about 800 years

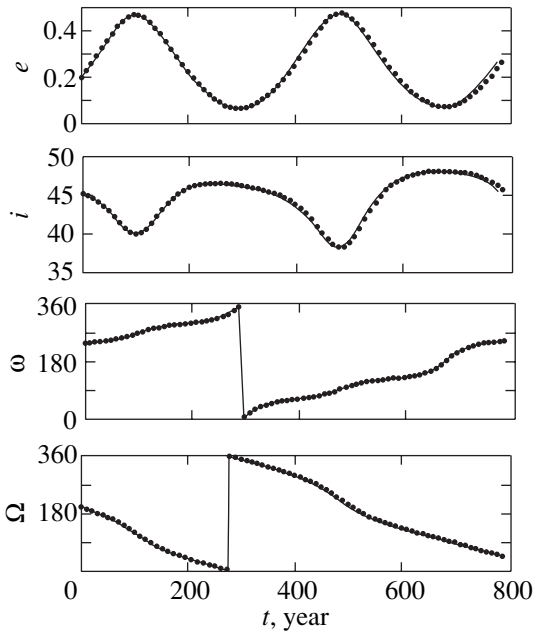

Fig. 2. Orbital evolution of S/2000 J1.

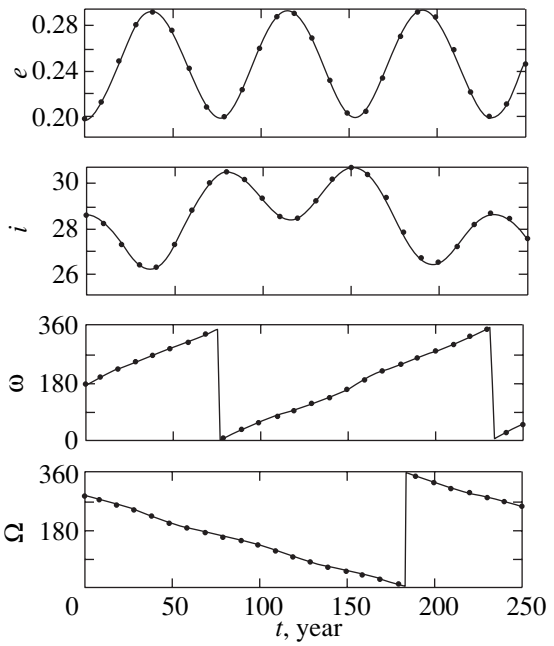

Fig. 3. Orbital evolution of S/2000 J11.

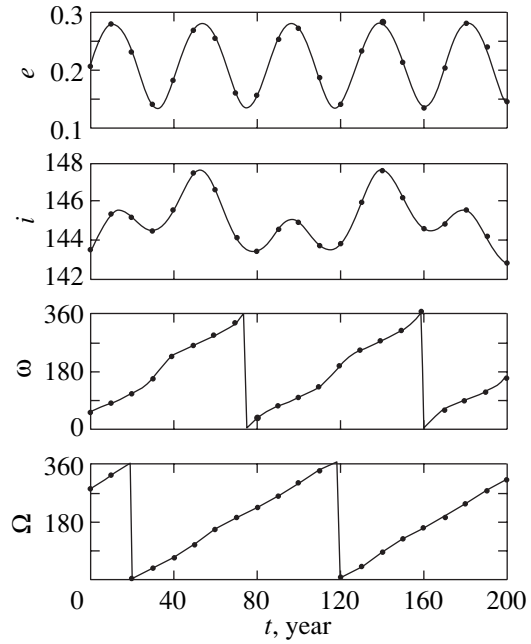

Fig. 4. Orbital evolution of S/1999 J1.

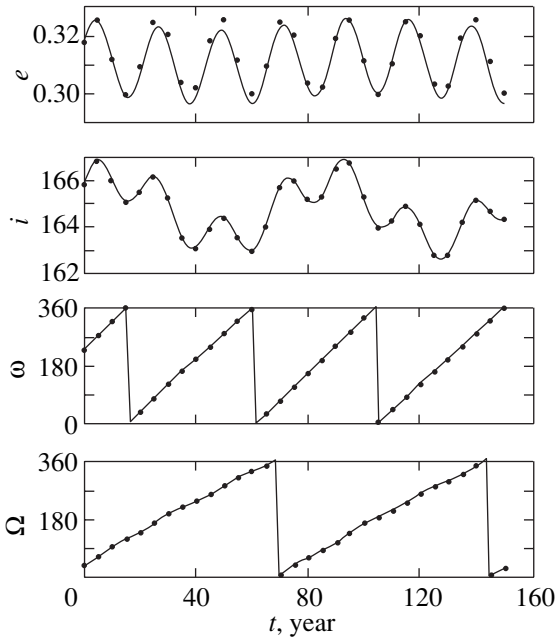

Fig. 5. Orbital evolution of S/2000 J2.

and more than 500 years, respectively. This is because this orbit is closest to Jupiter [its maximum apocenter distance is $Q_{max} = a(1 + e_{max}) \approx 11 \times 10^6$ km] and because the influence of solar attraction is weakest here.

In contrast, Q_{max} for the orbits of S/2000 J2 and S/2000 J8 are about 32 and 36×10^6 km, respectively, and exceed these parameters for the remaining satellites. As a result, the circulation periods of $\tilde{\omega}$ and $\tilde{\Omega}$ are at a minimum, only a few tens of years; i.e., the Sun rapidly "spins" these orbits with periods that are only several times longer than Jupiter's orbital period.

For convenience, plots of the evolving orbital elements for Jupiter's new outer satellites against time are shown in the Appendix (Figs. 2–13).

Figures 2 and 3 show plots of eccentricity e and angular ecliptic elements i, ω, and Ω (in degrees) for the orbits of two satellites from group I. Figures 4–13

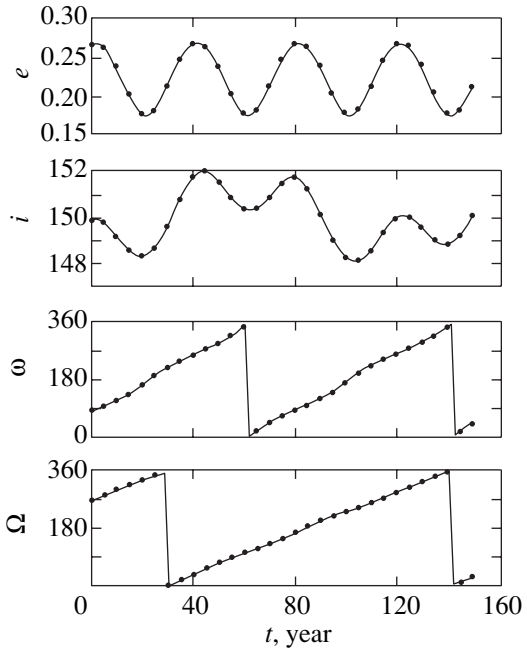

Fig. 6. Orbital evolution of S/2000 J3.

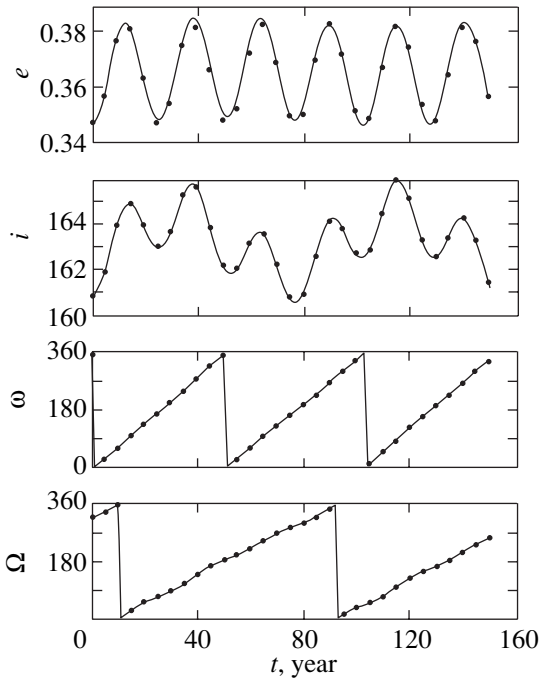

Fig. 7. Orbital evolution of S/2000 J4.

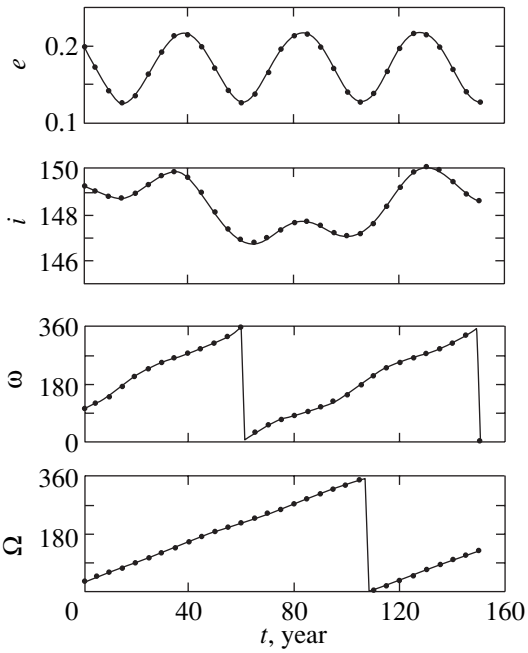

Fig. 8. Orbital evolution of S/2000 J5.

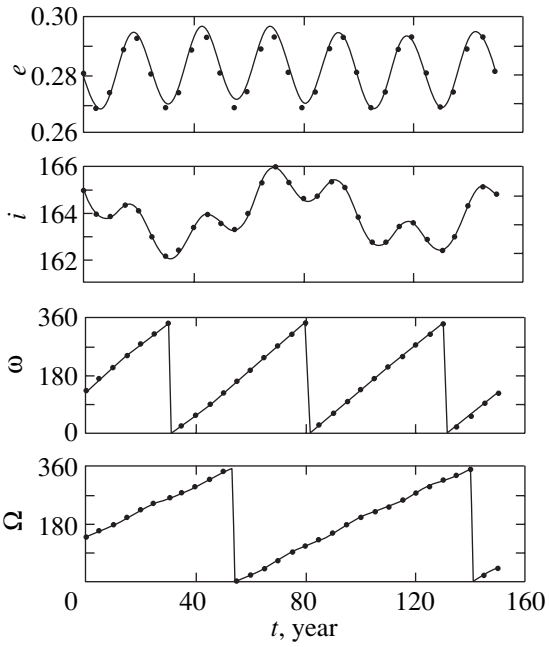

Fig. 9. Orbital evolution of S/2000 J6.

show similar plots for the satellite orbits of group II. In all figures, the dots mark the elements calculated from analytic formulas of the general solution for Hill's double-averaged problem. Since the periods of e, i libration and ω, Ω circulation are much less than 50 000 years, the change from ecliptic angular elements to orbital ones and back, which is required in the solution, was made at constant initial values of i' and Ω'. The solid lines in all figures represent the results of a check numerical integration of the fuller evolutional system. The discrepancies between the analytic and numerical results in the variation of eccentricities seen in Figs. 5, 7, 9, 12, and 13 are relatively small, ~0.002. In the remaining figures, the analytic dependencies $e(t)$ coincide with the numerical ones, to within the graphical accuracy. This is also true for the dependencies $i(t)$,

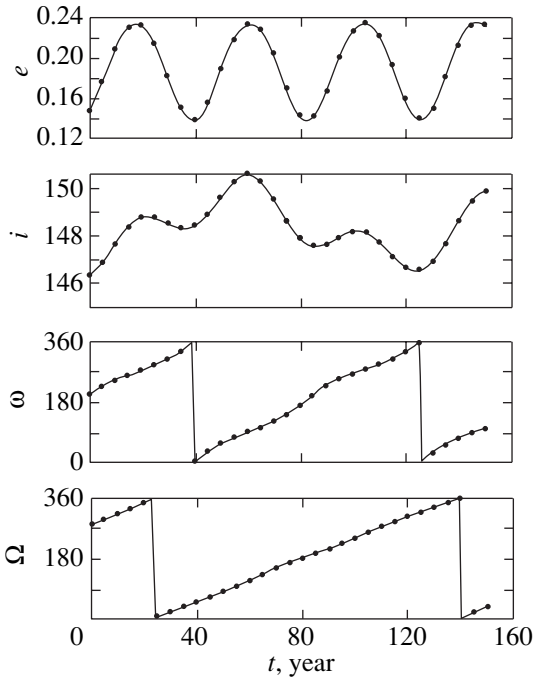

Fig. 10. Orbital evolution of S/2000 J7.

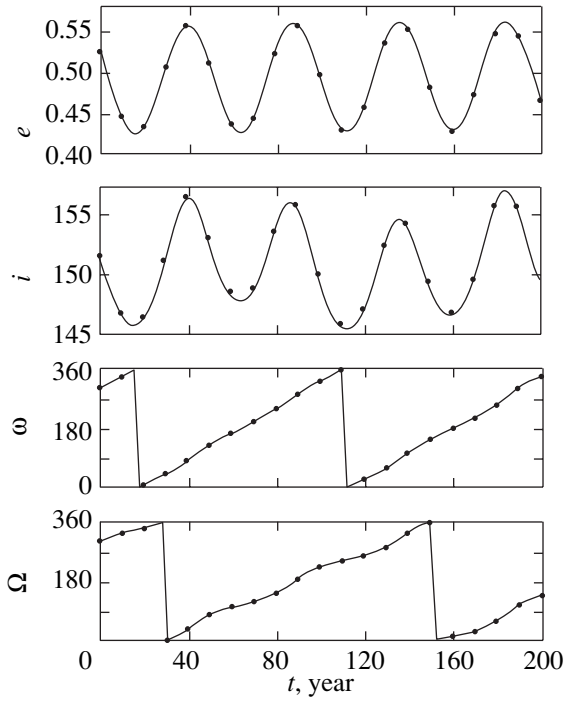

Fig. 11. Orbital evolution of S/2000 J8.

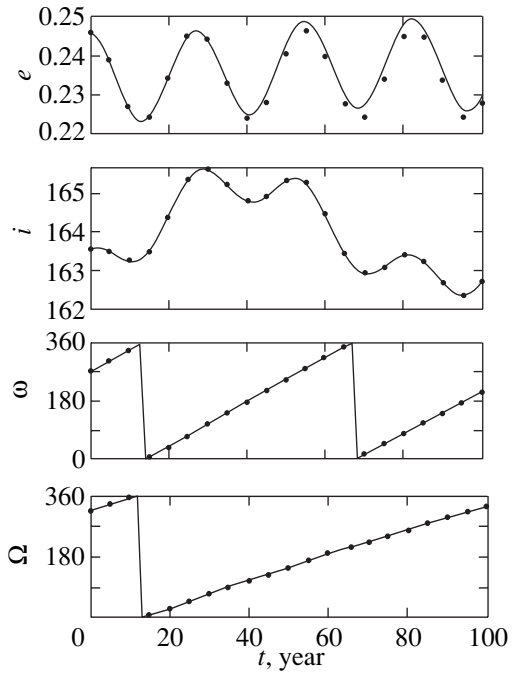

Fig. 12. Orbital evolution of S/2000 J9.

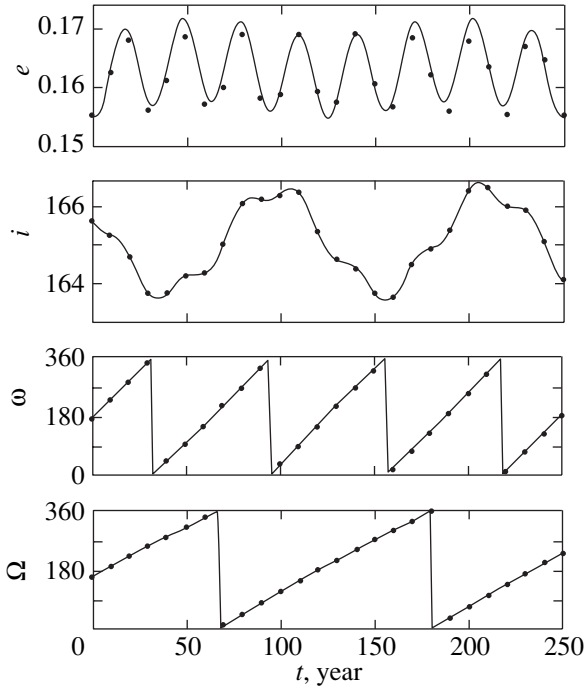

Fig. 13. Orbital evolution of S/2000 J10.

$\omega(t)$, and $\Omega(t)$ for the orbits of all satellites, S/1999 J1 and S/2000 J1–J11.

The orbital eccentricities of all satellites oscillate with twice the frequency of the variations in pericenter arguments. The inclination oscillations also contain a harmonic with the frequency of variations in node longitudes; when $\sin i$ is close enough to zero, this harmonic becomes dominant. This is particularly noticeable for the orbit of S/2000 J10 (Fig. 13), for which $e_{\max} \approx 0.17$ is at a minimum and, consequently, the amplitude of the oscillations with twice the frequency of the variations in $\tilde{\omega}$ is also at a minimum.

3. CONCLUSION

The recently discovered satellites of giant planets will undoubtedly attract the attention of researchers due to their physical properties and orbital dynamics. Having analyzed the orbital evolution of Jupiter's new outer satellites, we revealed its main qualitative features and obtained approximate quantitative characteristics. Our method of analysis allowed us to describe the time variations in satellite orbital elements with longest periods of the order of tens and hundreds of years. Among the perturbations that were not included in our averaged model, the perturbations associated with Jupiter's orbital motion, particularly for the outer satellites of group II, can be appreciable. To construct comprehensive theories for the motion of the new satellites, it is necessary to take into consideration the secular perturbations from Jupiter's oblateness (in particular, for S/2000 J1) and from the attraction by its Galilean satellites and Saturn, as well as the short-period perturbations associated with the satellite orbital motions (with periods no larger than approximately two years).

Qualitatively, it is of interest to explain the different orbital structures of Jupiter's, Saturn's, and Uranus's outer satellites.

ACKNOWLEDGMENTS

This study was supported by the Council of Grants of the President of Russia and the State Support for Leading Scientific Schools (grant. no. 00-15-96036).

REFERENCES

1. S. Ferraz-Mello, *Dynamics of Galilien Satellites* (Univ. de Såo Paulo, Såo Paulo, 1979; Mir, Moscow, 1983).
2. M. L. Lidov, in *Artificial Earth Satellites* (Akad. Nauk SSSR, Moscow, 1961), No. 8, p. 5.
3. M. I. Lidov, in *Problems of the Motion of Artificial Celestial Bodies* (Akad. Nauk SSSR, Moscow, 1963), p. 119.
4. B. G. Marsden, IAU Circ., No. 7460 (2000a).
5. B. G. Marsden, IAU Circ., No. 7469 (2000b).
6. B. G. Marsden, IAU Circ., No. 7525 (2000c).
7. B. G. Marsden, MPE Circ., Y16 (2000d).
8. B. G. Marsden, MPE Circ., A28 (2001a).
9. B. G. Marsden, MPE Circ., A29 (2001b).
10. V. S. Ural'skaya, Itogi Nauki Tekh., Ser. Issled. Kosm. Prostranstva **35**, 26 (1991).
11. M. A. Vashkov'yak, Pis'ma Astron. Zh. **25**, 554 (1999) [Astron. Lett. **25**, 476 (1999)].
12. M. A. Vashkov'yak, Pis'ma Astron. Zh. **27**, 533 (2001) [Astron. Lett. **27**, 455 (2001)].

Astronomy Letters, Vol. 27, No. 10, 2001, pp. 678–682. Translated from Pis'ma v Astronomicheskiĭ Zhurnal, Vol. 27, No. 10, 2001, pp. 795–800.

Triple Approaches in the Plane Isosceles Equal-Mass Three-Body Problem

V. V. Orlov[1]*, A. V. Petrova[1], and A. I. Martynova[2]

[1] *Sobolev Astronomical Institute, St. Petersburg State University, Bibliotechnaya pl. 2, Petrodvorets, 198904 Russia*
[2] *St. Petersburg Academy of Forestry Engineering, Institutskiĭ per. 5, St. Petersburg, 194021 Russia*

Received April 16, 2001

Abstract—We analyze flyby-type triple approaches in the plane isosceles equal-mass three-body problem and in its vicinity. At the initial time, the central body lies on a straight line between the other two bodies. Triple approaches are described by two parameters: virial coefficient k and parameter $\mu = \dot{r}/\sqrt{\dot{r}^2 + \dot{R}^2}$, where $\dot{r}$ is the relative velocity of the extreme bodies and $\dot{R}$ is the velocity of the central body relative to the center of mass of the extreme bodies. The evolution of the triple system is traceable until the first turn or escape of the central body. The ejection length increases with closeness of the triple approach (parameter k). The longest ejections and escapes occur when the extreme bodies move apart with a low velocity at the time of triple approach. We determined the domain of escapes; it corresponds to close triple approaches ($k > 0.8$) and to μ in the range $-0.2 < \mu < 0.7$. For small deviations from the isosceles problem, the evolution does not differ qualitatively from the isosceles case. The domain of escapes decreases with increasing deviations. In general, the ejection length increases for wide approaches and decreases for close approaches. *© 2001 MAIK "Nauka/Interperiodica".*

Key words: *celestial mechanics*

INTRODUCTION

The three-body problem is one of the classical problems in analytical dynamics and celestial mechanics. Considerable progress in understanding the qualitative behavior of the solutions of this problem has been made through numerical experiments. Szebehely (1971) suggested the following classification of the types of motions in the general three-body problem with a negative energy ($E < 0$): (1) simple interaction, (2) ejection with return, (3) escape, (4) stable revolution, (5) Lagrangian equilibrium solutions, and (6) collisions and periodic orbits.

Agekyan and Martynova (1973) supplemented this classification with yet another type: (0) close triple approach. A close triple approach can result in the escape of one of the bodies from the system (see, e.g., Anosova and Zavalov 1981).

Anosova and Zavalov (1981) proposed to divide triple approaches into two types:

(1) *Flybys*, when one of the components passes near the center of inertia of a temporary binary formed by the other two bodies;

(2) *Exchanges*, when this component replaces one of the components of the temporary binary after a series of double approaches.

In triple systems with equal-mass components, escapes more commonly occur after triple approaches of the first type (Anosova and Zavalov 1981).

Agekyan and Anosova (1991) considered flyby-type triple approaches by introducing several approach parameters: closeness, the minimum distance of the passing body from the center of mass of the triple system, and two component velocity ratios. They outlined the domain in the space of these parameters that corresponded to the escape of a passing body after a triple approach. They also formulated the necessary conditions for such an escape: (1) the approach must be sufficiently close (virial coefficient $k \geq 0.86$); (2) at the time of the closest approach of the passing body to the center of mass of the triple system, the other two bodies must recede from each other; and (3) the velocity directions of all bodies must be nearly orthogonal to the straight line that connects the bodies.

The domain of parameters for the triple approaches that result in escapes outlined by Agekyan and Anosova (1991) lies in the vicinity of the isosceles three-body problem. It is therefore of interest to analyze the isosceles case in more detail.

* E-mail address for contacts: vor@astro.spbu.ru

TECHNIQUE

Let us consider the plane isosceles equal-mass three-body problem. Denote the distance between the extreme bodies by r and the distance between the central body and the center of mass of the other two bodies by R. Choose the system of units in such a way that the body masses and the gravitational constant are equal to unity and the total energy of the triple system is $E = -1$. The equations of motion are then

$$\ddot{r} = -\frac{2}{r^2} - \frac{8r}{(r^2 + 4R^2)^{3/2}}, \quad (1)$$

$$\ddot{R} = -\frac{24R}{(r^2 + 4R^2)^{3/2}}. \quad (2)$$

The energy integral for the system is

$$\frac{1}{4}\dot{r}^2 + \frac{1}{3}\dot{R}^2 - \frac{1}{r} - \frac{4}{(r^2 + 4R^2)^{1/2}} = -1. \quad (3)$$

At the initial time, in the state of a triple approach, the central body lies on the straight line that connects the extreme bodies ($R_0 = 0$) and moves along the perpendicular to this straight line upward ($\dot{R}_0 > 0$). The initial conditions can then be specified by using only two parameters. As the first parameter, we take the virial coefficient, the ratio of the kinetic and potential energies of the triple system:

$$k = \left(\frac{\dot{r}_0^2}{4} + \frac{\dot{R}_0^2}{3}\right)\frac{r_0}{5}. \quad (4)$$

As the second parameter, we take the ratio

$$\mu = \frac{\dot{r}_0}{\sqrt{\dot{r}_0^2 + \dot{R}_0^2}}. \quad (5)$$

The virial coefficient $k \in (0,1)$ characterizes the closeness of triple approaches; the approaches become closer with increasing k. The parameter $\mu \in (-1,1)$ characterizes the relation between the body velocities: the extreme bodies approach each other at $\mu < 0$ and move apart at $\mu > 0$. We do not consider the boundary conditions $k = 0$, $k = 1$, and $\mu = \pm 1$, because they result in triple collisions.

The initial coordinates and velocities can be expressed in terms of k and μ as

$$r_0 = 5(1-k), \quad (6)$$

$$R_0 = 0, \quad (7)$$

$$\dot{r}_0 = \mu\sqrt{\frac{12k}{(1-k)(4-\mu^2)}}, \quad (8)$$

$$\dot{R}_0 = \sqrt{\frac{12k(1-\mu^2)}{(1-k)(4-\mu^2)}}. \quad (9)$$

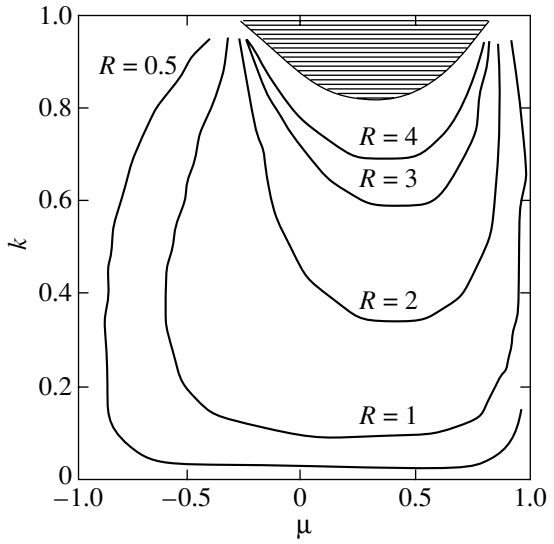

Fig. 1. The domain of (k, μ) parameters corresponding to escapes (hatched region) and R = const isolines on the (k, μ) plane.

Consider the following values of k and μ:

$$k = 0.05(0.05)0.95, \quad (10)$$

$$\mu = -0.95(0.05)0.95. \quad (11)$$

For each set of initial conditions, we traced the evolution of the triple system either until the "turn" of the central body, when $\dot{R}$ changed sign, or until the escape criterion was satisfied (Yoshida 1972; Marchal 1974):

$$R > \frac{1}{2}, \quad \dot{R} > 0, \quad \dot{R}^2 > \frac{96R}{16R^2 - 1}. \quad (12)$$

In this paper, we consider only the effect of a triple approach on the subsequent ejection or escape of the central body. In the case of the turn, we estimate the ejection length R. In the case of breakup, we determine the energy of hyperbolic motion

$$E_{ex} = \frac{1}{3}\dot{R}^2 - \frac{2}{R}. \quad (13)$$

RESULTS

The domain of initial conditions defined by the parameters (k, μ) breaks up into two continuous domains:

(1) the domain of escapes ($E_{ex} > 0$);

(2) the domain of ejections ($E_{ex} < 0$).

The domain of escapes is hatched in Fig. 1. Its boundary is well approximated by a cubic curve:

$$k = 0.29\mu^3 + 0.43\mu^2 - 0.37\mu + 0.88. \quad (14)$$

Note that all escapes result from close triple approaches with $k > 0.82$. Figure 1 also shows R = const

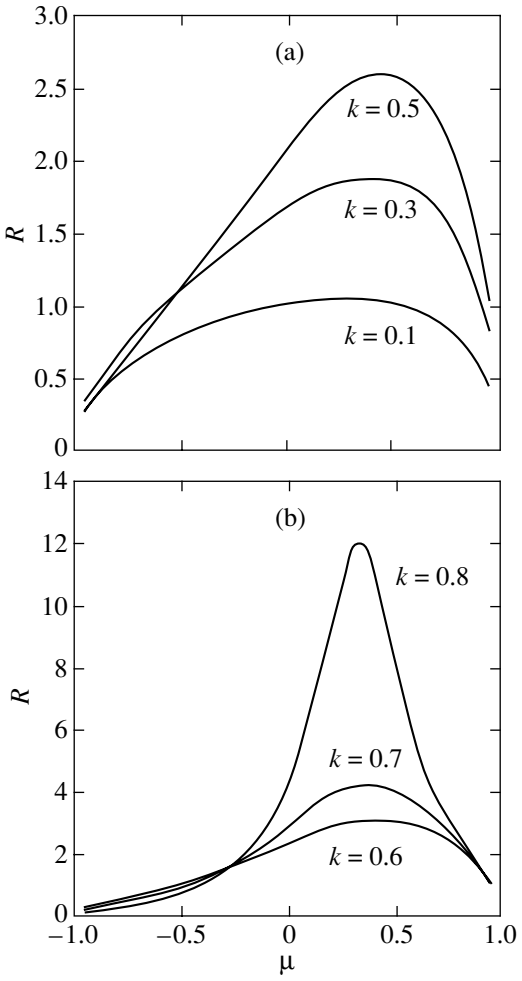

Fig. 2. Ejection length R versus μ for various virial coefficients $k = 0.1$, 0.3, 0.5 (a) and $k = 0.6$, 0.7, and 0.8 (b).

isolines. These isolines enclose the domain of escapes and recede from it as the ejection length decreases.

Consider the dependence of ejection length $R(k, \mu)$ on initial conditions in more detail. Let us fix the virial coefficient k (the closeness of approaches) and vary the velocity ratio μ. Figure 2 shows the dependencies $R(\mu)$ for several k. All these functions are unimodal; they reach a maximum at μ from 0.2 to 0.5 (the extreme bodies slowly recede from each other). The skewness of the functions $R(\mu)$ slightly increases with approach closeness. At $k < 0.5$, the turns are not ejections in the terminology of Agekyan and Martynova (1973) because they do not reach the radius of the ejection sphere:

$$R = \frac{3\sqrt{3}}{2} \approx 2.60. \quad (15)$$

For close triple approaches with $k > 0.5$, the ejection length increases with k for $\mu \in (-0.3, 1)$, whereas for $\mu \in (-1, -0.3)$, the ejection length decreases with increasing approach closeness. Figure 3 shows a general three-

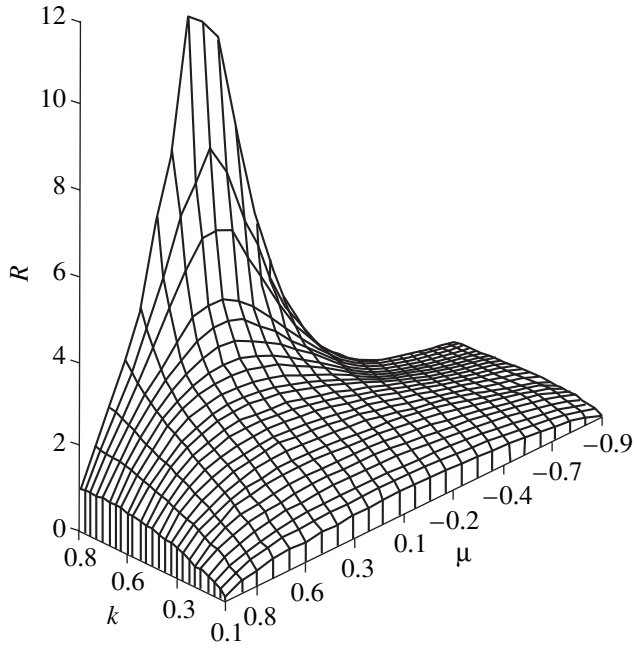

Fig. 3. Function $R(k, \mu)$.

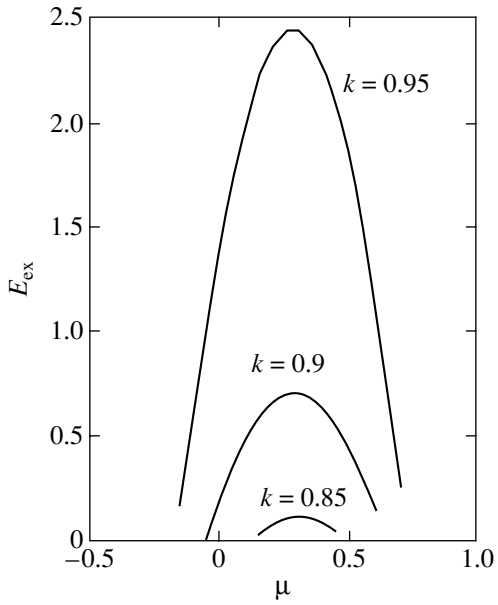

Fig. 4. Dependencies $E_{ex}(\mu)$ for escapes.

dimensional pattern of variations in $R(k, \mu)$ with a distinct sharp rise at $k > 0.5$ and $\mu \in (0, 0.7)$.

Below, we give a physical interpretation of the peculiar features in the behavior of the function $R(k, \mu)$ that we established.

(1) If the extreme bodies recede from each other at the time of a triple approach, then the force exerted by them on the passing body will decrease after the approach and the central body can escape from the tri-

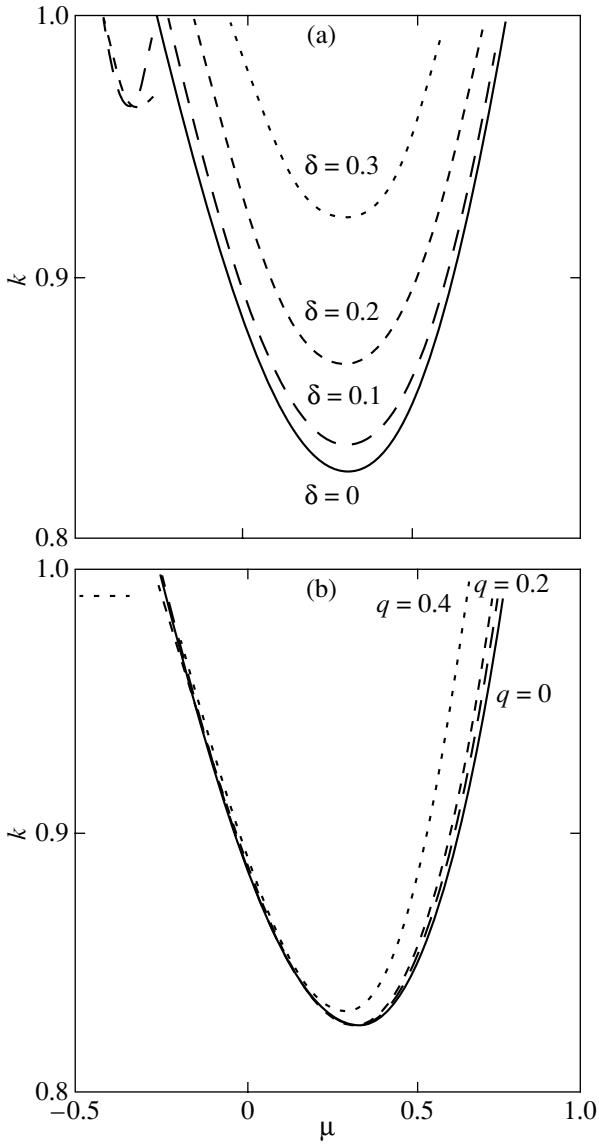

Fig. 5. Deformation of the domain of (k, μ) parameters corresponding to escapes as δ varies for $q = 0$ (a) and q varies for $\delta = 0$ (b).

ple system. If the two extreme bodies approach each other, then the passing body will greatly decelerate after the approach and the store of its kinetic energy may not be enough for the escape; the faster the extreme bodies approach each other, the faster the deceleration force increases and the more efficient is the deceleration process.

(2) At $\mu \approx \pm 1$, the bulk of the kinetic energy of the triple system is contained in the relative motion of the extreme bodies, while the velocity of the central body is very low; consequently, the store of its kinetic energy is negligible and the turn occurs at a very small distance from the center of mass of the triple system.

(3) There is an optimum value of μ (it depends weakly on the closeness of the triple approach) at which

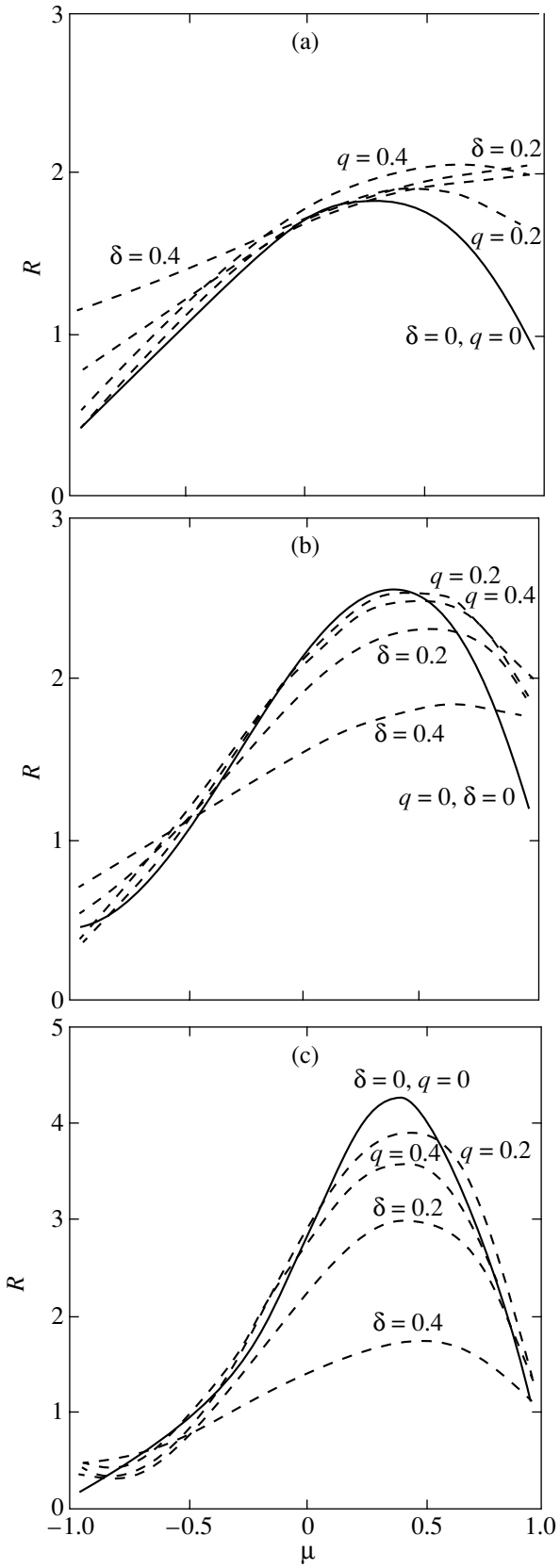

Fig. 6. $R(\mu)$ curves for (a) $k = 0.3$, (b) $k = 0.5$, and (c) $k = 0.7$ and $q = 0$ for various δ, and $R(\mu)$ curves for (a) $k = 0.3$, (b) $k = 0.5$, and (c) $k = 0.7$ and $\delta = 0$ for various q (δ and q are indicated near the curves).

the ejection is longest; this value of μ lies near 1/3. The existence of an optimum range for μ is a natural result of the patterns of behavior noted above, because this range must lie at $\mu > 0$, but not too close to $\mu = 1$.

Consider now the domain of parameters (k, μ) that corresponds to the triple approaches that result in the escape of the central body (the hatched region in Fig. 1). Figure 4 shows the dependencies $E_{ex}(\mu)$ for three fixed values of k. These functions are qualitatively similar in behavior to $R(k, \mu)$ in the vicinity of their maxima (see Fig. 2b). They are almost symmetric with a maximum near $\mu = 1/3$. The $E_{ex}(\mu)$ curves do not intersect: the closer the triple approach is, the higher the corresponding curve lies and the higher is the energy carried away by the escaping body.

DEVIATIONS FROM THE ISOSCELES PROBLEM

Let us now analyze the deviations from the isosceles problem. These deviations can result both from the displacement of the central body along the segment connecting the extreme bodies and from the deviation of the velocity vector of the central body from the perpendicular to this segment.

The following quantity is considered the displacement parameter:

$$\delta = \frac{2\Delta}{r_0}, \tag{16}$$

where Δ is the distance from the central body to the center of mass of the triple system. We use the following quantity as the parameter of deviation of the velocity vector of the central body from the perpendicular:

$$q = \cos\phi, \tag{17}$$

where ϕ is the angle between the velocity vector of the central body and the segment connecting the two extreme bodies. The case $\delta = 0$ and $q = 0$ corresponds to the isosceles problem.

Consider the initial conditions that differ only slightly from the isosceles case:

$$0 < \delta \le 0.4, \quad 0 < q \le 0.4. \tag{18}$$

Figure 5 shows the deformation of the domain of initial conditions that correspond to the escapes of the central body as δ and q vary. The area of this domain slightly decreases with increasing δ and q. Deviations from the isosceles case cause the velocity of the central body to decrease. For significant deviations from the isosceles problem, the domain of escapes breaks up into two parts. No other domains of escapes have been found in the vicinity of the isosceles problem.

Let us consider the effects of deviations from the isosceles case on the ejection length R. The results are shown in Fig. 6. The function $R(\mu)$ becomes flatter with increasing distance δ. Therefore, the larger δ is, the smaller is the increase in maximum R with increasing closeness of the triple approach. The effect of q variation is much weaker than the effect of δ variation. When the direction of motion of the central body deviates from the normal, the behavior of the $R(\mu)$ curves does not change qualitatively. However, there are quantitative discrepancies; in particular, the maximum value of R is slightly smaller at large k. In general, the ejection length increases with increasing deviations from the isosceles problem for wide triple approaches and decreases for close triple approaches.

CONCLUSION

In conclusion, we note a well-defined relation between the parameters of flyby-type triple approaches and the length of the subsequent ejection of the passing body. If the extreme bodies at the approach time move apart or approach each other at a low velocity, then closer approaches result in longer ejections or escapes. If, alternatively, the extreme bodies approach each other or recede from each other at a high velocity, then such approaches end up with short ejections; closer approaches can often result in shorter ejections. Such a behavior is attributable to the interaction between the central body with the binary formed by the extreme bodies before and after the triple approach. If the accelerating force before the approach significantly exceeds the deceleration effect after the approach, then a long ejection or escape takes place. Otherwise, a short ejection with return takes place.

Deviations from the isosceles problem cause the ejection length to increase for wide triple approaches and to decrease for close triple approaches (except the cases where the extreme bodies approach each other or move apart very fast). As the deviations from the isosceles case increase, the domain of initial conditions that correspond to the escapes of the central body is also deformed and reduced.

REFERENCES

1. T. A. Agekyan and Zh. P. Anosova, Astron. Zh. **68**, 1099 (1991) [Sov. Astron. **35**, 551 (1991)].
2. T. A. Agekyan and A. I. Martynova, Vestn. Leningr. Univ., No. 1, 122 (1973).
3. Zh. P. Anosova and N. N. Zavalov, Tr. Astrofiz. Obs. Leningr. Gos. Univ. **36**, 109 (1981).
4. C. Marchal, Celest. Mech. **9**, 381 (1974).
5. V. Szebehely, Celest. Mech. **4**, 116 (1971).
6. J. Yoshida, Publ. Astron. Soc. Jpn. **24**, 391 (1972).

Translated by A. Dambis